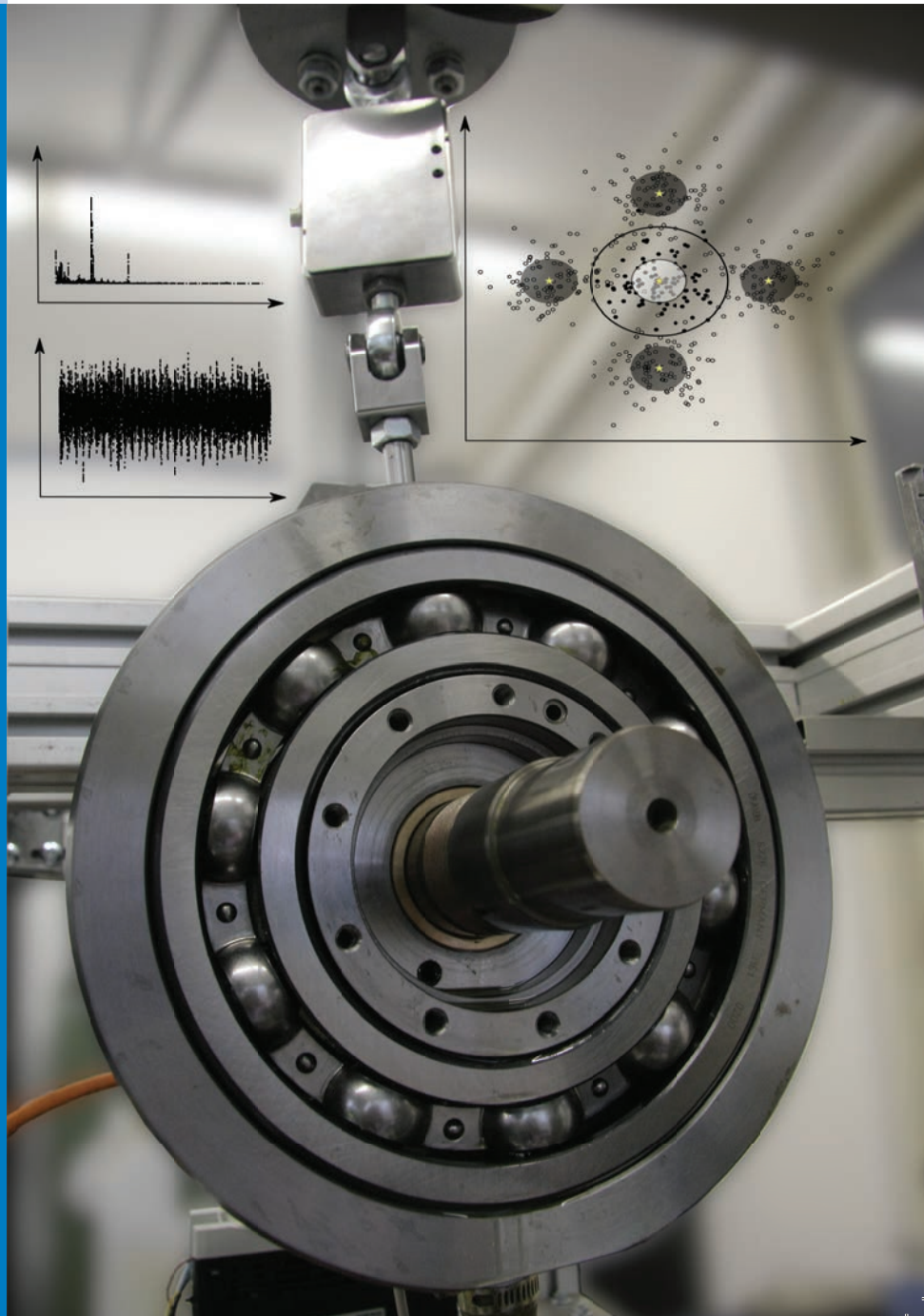




# Strojniški vestnik

# Journal of Mechanical Engineering



no. **4**  
year **2020**  
volume **66**

# Strojniški vestnik – Journal of Mechanical Engineering (SV-JME)

## Aim and Scope

The international journal publishes original and (mini)review articles covering the concepts of materials science, mechanics, kinematics, thermodynamics, energy and environment, mechatronics and robotics, fluid mechanics, tribology, cybernetics, industrial engineering and structural analysis.

The journal follows new trends and progress proven practice in the mechanical engineering and also in the closely related sciences as are electrical, civil and process engineering, medicine, microbiology, ecology, agriculture, transport systems, aviation, and others, thus creating a unique forum for interdisciplinary or multidisciplinary dialogue.

The international conferences selected papers are welcome for publishing as a special issue of SV-JME with invited co-editor(s).

## Editor in Chief

Vincenc Butala

University of Ljubljana, Faculty of Mechanical Engineering, Slovenia

## Technical Editor

Pika Škraba

University of Ljubljana, Faculty of Mechanical Engineering, Slovenia

## Founding Editor

Bojan Kraut

University of Ljubljana, Faculty of Mechanical Engineering, Slovenia

## Editorial Office

University of Ljubljana, Faculty of Mechanical Engineering

SV-JME, Aškerčeva 6, SI-1000 Ljubljana, Slovenia

Phone: 386 (0)1 4771 137

Fax: 386 (0)1 2518 567

info@sv-jme.eu, <http://www.sv-jme.eu>

**Print:** Koštomaj printing office, printed in 275 copies

## Founders and Publishers

University of Ljubljana, Faculty of Mechanical Engineering,  
Slovenia

University of Maribor, Faculty of Mechanical Engineering,  
Slovenia

Association of Mechanical Engineers of Slovenia

Chamber of Commerce and Industry of Slovenia,

Metal Processing Industry Association

## President of Publishing Council

Mitjan Kalin

University of Ljubljana, Faculty of Mechanical Engineering, Slovenia

## Vice-President of Publishing Council

Bojan Dolšak

University of Maribor, Faculty of Mechanical Engineering, Slovenia

## International Editorial Board

Kamil Arslan, Karabuk University, Turkey

Hafiz Muhammad Ali, King Fahd U. of Petroleum & Minerals, Saudi Arabia

Josep M. Bergada, Politechnical University of Catalonia, Spain

Anton Bergant, Litostroj Power, Slovenia

Miha Boltežar, University of Ljubljana, Slovenia

Filippo Cianetti, University of Perugia, Italy

Janez Diaci, University of Ljubljana, Slovenia

Anselmo Eduardo Diniz, State University of Campinas, Brazil

Jožef Duhovnik, University of Ljubljana, Slovenia

Igor Emri, University of Ljubljana, Slovenia

Imre Felde, Obuda University, Faculty of Informatics, Hungary

Janez Grum, University of Ljubljana, Slovenia

Imre Horvath, Delft University of Technology, The Netherlands

Aleš Hribernik, University of Maribor, Slovenia

Soichi Ibaraki, Kyoto University, Department of Micro Eng., Japan

Julius Kaplunov, Brunel University, West London, UK

Iyas Khader, Fraunhofer Institute for Mechanics of Materials, Germany

Jernej Klemenc, University of Ljubljana, Slovenia

Milan Kljajin, J.J. Strossmayer University of Osijek, Croatia

Peter Krajnik, Chalmers University of Technology, Sweden

Janez Kušar, University of Ljubljana, Slovenia

Gorazd Lojen, University of Maribor, Slovenia

Darko Lovrec, University of Maribor, Slovenia

Thomas Lübben, University of Bremen, Germany

Jure Marn, University of Maribor, Slovenia

George K. Nikas, KADMOS Engineering, UK

Tomaž Pepelnjak, University of Ljubljana, Slovenia

Vladimir Popović, University of Belgrade, Serbia

Franci Pušavec, University of Ljubljana, Slovenia

Mohammad Reza Safaei, Florida International University, USA

Marco Sortino, University of Udine, Italy

Branko Vasić, University of Belgrade, Serbia

Arkady Voloshin, Lehigh University, Bethlehem, USA

## General information

Strojniški vestnik – Journal of Mechanical Engineering is published in 11 issues per year (July and August is a double issue).

Institutional prices include print & online access: institutional subscription price and foreign subscription €100,00 (the price of a single issue is €10,00); general public subscription and student subscription €50,00 (the price of a single issue is €5,00). Prices are exclusive of tax. Delivery is included in the price. The recipient is responsible for paying any import duties or taxes. Legal title passes to the customer on dispatch by our distributor. Single issues from current and recent volumes are available at the current single-issue price. To order the journal, please complete the form on our website. For submissions, subscriptions and all other information please visit: <http://www.sv-jme.eu>.

You can advertise on the inner and outer side of the back cover of the journal. The authors of the published papers are invited to send photos or pictures with short explanation for cover content.

We would like to thank the reviewers who have taken part in the peer-review process.

The journal is subsidized by Slovenian Research Agency.

Strojniški vestnik - Journal of Mechanical Engineering is available on <https://www.sv-jme.eu>.



### Cover:

Bearing fault detection and classification is a critical task and often requires high success rates. To meet the requirements of such a demanding task, Gaussian mixture model based classification was applied and tested with different parameter estimation techniques.

### Image courtesy:

University of Ljubljana,  
Faculty of Mechanical Engineering,  
Chair of Machine elements  
and R&D evaluation (CMER&DE),  
Slovenia

ISSN 0039-2480, ISSN 2536-2948 (online)

© 2020 Strojniški vestnik - Journal of Mechanical Engineering. All rights reserved. SV-JME is indexed / abstracted in: SCI-Expanded, Compendex, Inspec, ProQuest-CSA, SCOPUS, TEMA. The list of the remaining bases, in which SV-JME is indexed, is available on the website.

# Contents

**Strojniški vestnik - Journal of Mechanical Engineering**  
**volume 66, (2020), number 4**  
**Ljubljana, April 2020**  
**ISSN 0039-2480**

**Published monthly**

## **Papers**

Branislav Panić, Jernej Klemenc, Marko Nagode: Gaussian Mixture Model Based Classification Revisited: Application to the Bearing Fault Classification	215
VanThien Nguyen, VietHung Nguyen, VanTrinh Pham: Deep Stacked Auto-Encoder Network Based Tool Wear Monitoring in the Face Milling Process	227
Jakub Sikorski, Witold Pawlowski: Internal Friction of Ball Bearings at Very Low Temperatures	235
Sanjay Sundriyal, Vipin, Ravinderjit Singh Walia: Study on the Influence of Metallic Powder in Near-Dry Electric Discharge Machining	243
A.K. Babu, G. Kumaresan, V. Antony Aroul Raj, R. Velraj: Experimental Investigations of Thin-layer Drying of Leaves in a Heat-Pump Assisted Tray-type Batch Drying Chamber	254
Yang Zhang, Duanwei Shi, Tong Xiao, Ji Zhou, Xionghao Cheng: Pitch Stability Analysis for Mechanical-Hydraulic-Structural-Fluid Coupling System of High-Lift Hoist Vertical Shiplift	266



# Gaussian Mixture Model Based Classification Revisited: Application to the Bearing Fault Classification

Branislav Panič\* – Jernej Klemenc – Marko Nagode  
University of Ljubljana, Faculty of Mechanical Engineering, Slovenia

*Condition monitoring and fault detection are nowadays popular topic. Different loads, environments etc. affect the components and systems differently and can induce the fault and faulty behaviour. Most of the approaches for the fault detection rely on the use of the good classification method. Gaussian mixture model based classification are stable and versatile methods which can be applied to a wide range of classification tasks. The main task is the estimation of the parameters in the Gaussian mixture model. Those can be estimated with various techniques. Therefore, the Gaussian mixture model based classification have different variants which can vary in performance. To test the performance of the Gaussian mixture model based classification variants and general usefulness of the Gaussian mixture model based classification for the fault detection, we have opted to use the bearing fault classification problem. Additionally, comparisons with other widely used non-parametric classification methods are made, such as support vector machines and neural networks. The performance of each classification method is evaluated by multiple repeated k-fold cross validation. From the results obtained, Gaussian mixture model based classification methods are shown to be competitive and efficient methods and usable in the field of fault detection and condition monitoring.*

**Keywords:** Gaussian mixture models, classification, bearing fault estimation, parameter estimation, performance of classification methods

## Highlights

- Gaussian-mixture-model-based classification was applied to the bearing-fault classification.
- To discriminate the faulty from non-faulty bearings only simple statistics from vibrational data was used.
- Two different datasets, the Case Western Rice University dataset and Bearing vibration data collected under time-varying rotational speed conditions dataset are used.
- The Gaussian-mixture-model-based classification method showed to be a competitive and efficient method.

## 0 INTRODUCTION

Structural health monitoring, condition monitoring, damage and fault detection are popular topics in engineering [1] and [2]. The early detection of a failure or a fault can be taken as a synonym for the improved maintenance, safety and reliability of a mechanical system or a structure. Constantly evolving fields such as machine learning, data mining and data analysis have greatly facilitated the above-mentioned fields for a great deal of mechanical engineering and engineering generally. Methods from the machine-learning group such as classification methods are widely utilized for different tasks from the diagnostics of aircraft engine blades [3] to the health monitoring of steel plates [4] and the classification of failure modes and the prediction of the shear strength for reinforced concrete beam-column joints [5].

Another great example of the utilization of the classification methods is the bearing-fault classification [6] and [7]. Bearing-fault detection is a very popular problem in mechanical engineering since bearings are one of the most utilized rotational mechanical elements [8] and [9]. This is due to the many phenomena affecting the working conditions

of bearings [10] and [11]. Additionally, bearings are mechanical elements that are easily replaceable, yet the untreated fault of a bearing can cause the failure of other elements in a mechanical system, shafts and other [12]. Failures of other elements can cause a high security risk in some applications or larger economic losses due to longer maintenance times in other applications.

Studies on bearing-fault classification differ in two ways. The first type of studies covers different signal-processing techniques for the classification of bearing faults [7] and [13] or for feature extraction and selection from vibrational data, which are then used to enhance the results of an applied classification method [14]. Other studies mostly utilize the different classification methods to obtain better classification results [6] and [15]. This paper is of the latter type. We have applied four types of classification methods based on the Gaussian mixture model (GMM) to the problem of bearing-fault classification. To compare the performance of the GMM-based classification method, three different non-parametric classification methods are used. All the results are obtained on two real-world datasets, the famous *Case Western*

University dataset [16] and the Variable rotational speed bearing fault dataset [17].

The paper is structured as follows. Section 1 gives the background on GMM-based classification along with a thorough explanation of the different methods and parameter-estimation algorithms. Section 2 gives a brief overview of other non-parametric classification methods. Section 3 tackles the evaluation of the performance of each classification method on the particular dataset. Section 4 describes the datasets and the feature-extraction process. The results and discussion are given in Section 5 and the paper ends with the concluding remarks in Section 6.

## 1 GAUSSIAN-MIXTURE-MODEL-BASED CLASSIFICATION

Data with a known class affiliation, used for determining a classification model, is often perceived as a realization of random variables. This fact is used in the framework of Bayes decision theory [18]. The classification of new observations to one of  $K$  classes is conducted by estimating posterior probabilities  $P(C_i|\mathbf{y})$  for every class and choosing the class  $j$  with the maximum posterior probability Eq. (1).

$$j = \arg \max \left( P(C_i|\mathbf{y}) \right), \quad i = 1, \dots, K. \quad (1)$$

The estimation of posterior probabilities for each class  $P(C_i|\mathbf{y})$  is calculated using the Bayes allocation rule (Eq. 2), which depends on probability density function (PDF)  $P(\mathbf{y}|C_i)$  and the apriori probability of each class  $P(C_i)$ . The estimation of latter becomes the main problem of classification.

$$P(C_i|\mathbf{y}) = \frac{P(C_i)P(\mathbf{y}|C_i)}{\sum_{j=1}^N P(C_j)P(\mathbf{y}|C_j)}. \quad (2)$$

Estimating the class PDF is not a simple task as clear evidence does not exist as to which probability distribution family to use. The choice of probability distribution affects the discriminating functions between classes. For example, in [19], a Gaussian distribution with the same covariance matrices for each class (homoscedacity assumption) is used. This results in linear discriminating functions between classes, illustrated on the first column of plots in Fig. 1, hence the method was named linear discriminant analysis (LDA) [20]. However, if the assumption of homoscedacity is removed (the covariance matrices are different for each class), quadratic discriminating functions are achieved, represented in the second

column of the plots in Fig 1. This is known as quadratic discriminant analysis (QDA) [20].

The discriminating functions between classes can be more complex. The class distribution can be multi modal or skewed. Hence, an extension of classical linear and quadratic discriminant analysis was made in [21]. This extension, mixture discriminant analysis (MDA) utilizes mixture models (MM), precisely Gaussian mixture models (GMM), for the class PDF. Essentially, GMMs are used for cluster analysis and a semi-parametric probability density estimation. It is shown that GMMs can be used to estimate any continuous density with arbitrary accuracy [22] and [23]. They have a lower footprint on memory usage in comparison with non-parametric density estimators (kernel density estimators) as they do not require all the data to be stored once the parameters have been estimated. Additionally, the utilization of GMMs for estimating the class PDFs results in general non-linear discriminating functions between classes (third column on Fig 1).

### 1.2 Estimation of Parameters of Gaussian Mixture Models

A GMM is defined as the sum of  $c$  differently weighted Gaussian probability density functions where the sum of all weights  $w_l$  is equal to 1, Eq. (3), [24]. For example, the GMM used for modeling the class PDF on Fig. 1 contained five components with its mean value given with a yellow star and the covariance matrix represented as a red or blue ellipse.

$$f(\mathbf{y}|\Theta) = \sum_{l=1}^c w_l f(\mathbf{y}|\boldsymbol{\mu}_l, \boldsymbol{\Sigma}_l). \quad (3)$$

The difficulty in estimating the parameters  $\Theta$  of GMMs lies in the estimation of the number of components  $c$ , their weights  $w_l$ , mean vectors  $\boldsymbol{\mu}_l$  and covariance matrices  $\boldsymbol{\Sigma}_l$ .

#### 1.2.1 EM Approach

The most commonly used approach for the estimation of weights of components and component parameters (means and covariance matrices) is via the expectation-maximization (EM) algorithm [25]. The EM algorithm iteratively estimates the parameters of GMMs by maximizing the likelihood function. As the EM algorithm requires the number of components and some initial guess of the component weights and component parameters, an additional procedure is involved. The estimation of the GMM parameters is usually carried out via multiple runs of the EM

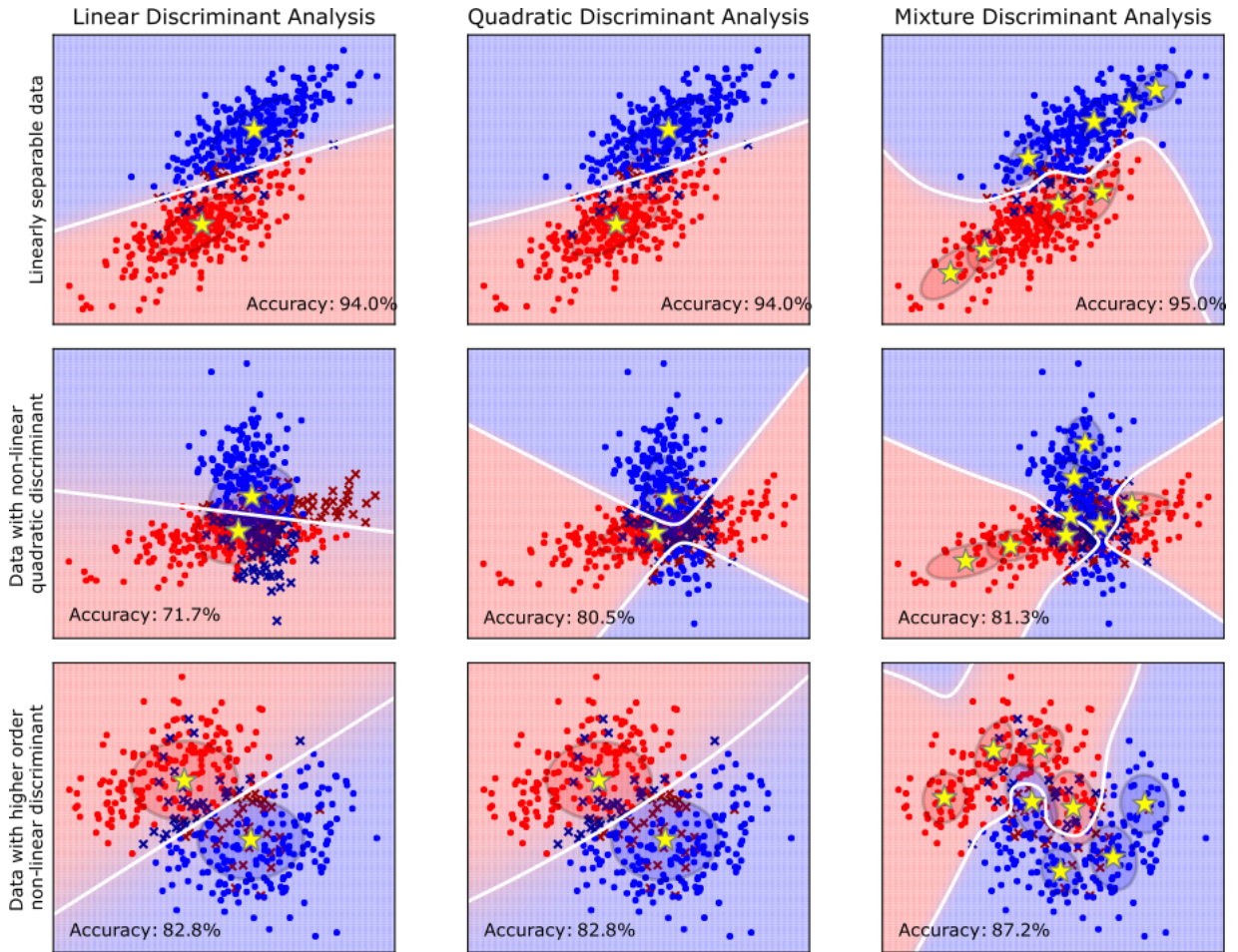


**Fig. 1.** Discriminant functions for LDA, QDA and MDA classification methods for the classification problems with linear discriminant, quadratic discriminant and non-linear discriminant function; first column represent LDA method; second column gives plots of QDA method; third column represents MDA method; first row: the dataset has linear separation between classes; second row: the dataset used has quadratic discriminant; third row: the dataset has non-linear discriminant

algorithm with different numbers of components. The initial guesses of weights of components and component parameters is achieved, for example, either by the random selection of points from the dataset, the  $k$ -means clustering algorithm or hierarchical clustering [26]. Furthermore, the EM algorithm does not guarantee convergence of the likelihood function for each initial guess of parameters, nor does it guarantee convergence to global optima. Therefore, multiple selections of initial guesses of parameters for each number of components is desirable. This makes the procedure of estimating the parameters of GMMs computationally burdening, especially for large datasets and datasets with a large number of dimensions. For a more in-depth explanation and mathematical derivation of the EM algorithm, readers are referred to [18] and [24].

### 1.2.2 REBMIX Approach

The rough-enhanced-Bayes mixture estimation (REBMIX) algorithm [27] and [28] can be used to estimate the parameters of a GMM. The algorithm is a numerical procedure that combines an empirical density estimation, mode-finding, clustering and maximum-likelihood estimation procedures for the estimation of such parameters. Instead of specifying the number of components and the initial guesses of component weights and parameters, the input parameters for the REBMIX algorithm are the smoothing parameters for the empirical density estimation procedures, for example, the number of bins in a histogram density estimation or the number of nearest neighbors for a  $k$ -nearest-neighbors (KNN) density estimation. Another parameter needing to be

specified is the maximum number of components in the GMM. For a given set of input parameters there are multiple estimations of the parameters for a GMM, which differ in terms of the number of components, and the component parameters and weights in the GMM.

### 1.3 Gaussian Mixture Model Selection for the Class Probability Density Function

In general, the results of both the procedures involving the EM algorithm and REBMIX algorithm are multiple parameters of the GMM, which differs in the number of components, the component parameters and weights. The selection of the appropriate parameters and the number of components is based on calculating the information criterion (IC) and selecting those parameters that yield a minimum value for the IC [24]. The IC is used to penalize complex models and hence avoids over-fitting problems. There is a lot of IC presented in the literature, see Chapter 6 of [24]. Out of them mostly used ones are definitely the Akaike information criteria (AIC) and the Bayesian information criterion (BIC). AIC is defined in Eq. (4), where  $M = c - 1 + c \cdot d + c \cdot d(d+1)/2$  is the number of parameters in the  $d$ -dimensional GMM for the number of components  $c$  and  $L$  is the likelihood value.

$$\text{AIC} = -2 \log(L) + 2M. \quad (4)$$

The second one, BIC, is defined in Eq. (5). Although AIC is a good criterion it penalizes less than BIC and for a large amount of data it can result in an over-fitted GMM. That being said, for the purpose of density estimation the BIC is usually best suited [29].

$$\text{BIC} = -2 \log(L) + M \log(L). \quad (5)$$

## 1.4 Software Implementations of GMM-Based Classification

Software implementations of the GMM-based classification procedures are applied using the R programming language [30]. The R programming language is mainly used for statistical computing, machine learning and data mining and therefore provides one of best environments for classification problems. For the software implementations the following convention is used: package names are written in italic font; function names are written in bold font.

### 1.4.1 Mixture Discriminant Analysis

The *mda* package [31] offers GMM-based classification described in [21]. The estimated GMMs for each class PDF have a known number of components in advance. The covariance matrix of each component in the GMM is diagonal and equal for all the components in the estimated GMM. Equal covariance matrices are also kept throughout all the GMMs estimated for different classes of PDF. The estimation of the GMM is achieved using the EM algorithm and  $k$ -means clustering is used for the initialization technique of the EM algorithm. The R package *mda* offers function **mda** for classification purposes. The user-specified input parameters for the **mda** function are the number of components for each class in the classification model. A simple validation procedure was employed for the selection of the number of components in the GMM. Additionally, each class in the classification problem was assumed to have the same number of components in the GMM and the best number of components was selected based on a minimal training error for each dataset. The number of components was selected to range from 1 to 9.

### 1.4.2 Model-Based Classification

Another widely used R package implementation for GMM-based classification is the *mclust* package [32]. Model-based classification improves upon the original *mda* method. The PDF of every class is assumed to follow a parsimonious GMM. Improvements are made in the sense of allowing the GMM to have different covariance structures. These covariance structures are thoroughly described with implementations in [33]. GMMs can have a different number of components for each class. The estimation of the parameters of a GMM is calculated using the EM algorithm coupled with hierarchical clustering initialization (*hclust*) [34]. The appropriate parameters of GMM are selected via the BIC. The R package *mclust* offers function **MclustDA** which is used for GMM-based classification. User-specified input parameters for the **MclustDA** function is the maximum number of components in the GMM. For the maximum number of components, the default value was 9.

### 1.4.3 REBMIX-Based Classification

The *rbmix* R package [35] offers GMM-based classification based on an estimation of the GMM for class PDF with the REBMIX algorithm [27], [36] and

[37]. For the estimation of the empirical probability density, the following procedures are implemented: histogram, kernel density and KNN. Different ICs can be used for the assessment of the number of components, component weights and component parameters [27]. The R package *rebmix* offers the function **REBMIX** for an estimation of the GMM for each class. User input parameters are a type of empirical density estimation and can be chosen from the histogram, kernel density estimation or KNN density estimation. Additionally, the user must supply the number of bins in the histogram and kernel density estimation or the number of nearest neighbors for the KNN density estimation. Additionally, the maximum number of components in the GMM is required. For the empirical density estimation we have used a histogram because it offers the fastest estimation of the GMM; and for the smoothing parameter, the number of bins selected was the default value. Additionally, due to the fact that REBMIX algorithm can be used as a standalone procedure or combined with EM algorithm [37] we have used two variants of this implementation, namely *rebmix* and *rebmix&EM*. The *rebmix&EM* used here corresponds to the Exhaustive REBMIX&EM strategy described in [37]. The maximum number of components was kept the same as for the *mda* and *mclust* case, which was 9.

**Table 1.** Properties of different GMM based classification methods

	<i>mda</i>	<i>mclust</i>	<i>rebmix</i>	<i>rebmix&amp;EM</i>
Uses EM?	yes	yes	no	yes
EM-init*	<i>k</i> -means	hclust	/	<i>rebmix</i>
Shrink**?	yes	yes	no	no
pros	mild***	diverse	rapid	mild***
cons	limiting	slow	faulty	over-fitting

\* How is the initialization of EM algorithm performed?

\*\* Does the method shrink the number of parameters in GMM?

\*\*\* Mild refers to the computational intensity of both methods.

The main differences and the advantages and disadvantages of each GMM-based classification method are listed in Table 1. The choice of algorithm for the estimation of GMM parameters may affect classification performance. Three methods use EM algorithm for estimation and only *rebmix* does not. Since the *rebmix* is merely an heuristic, the final estimated parameters of GMM can be degenerated, which is the main disadvantage. On the other hand, it provides rapid estimation compared to the EM algorithm [28]. Additionally, the EM algorithm used for the other three methods may be trapped in a local optima and requires careful initialization [37]. The choice of initial parameters directly affects the

final estimated GMM parameters, so we assume that different initialization can have advantages for the classification results. Finally, the GMM has a lot of parameters that need to be estimated. Most parameters belong to the covariance matrices of the different GMM components. Therefore, the general GMM with an unrestricted covariance matrix can produce over-fitting, and this is the main disadvantage of *rebmix&em* method. On the other hand, the *mda* method assumes a hard parsimony, which can probably be limiting. The *mclust* method offers 14 different types of covariance structures [32], which can be fruitful for classification problems. However, since this is very computationally intensive, this method can be quite slow.

## 2 NON-PARAMETRIC CLASSIFICATION METHODS

Non-parametric methods are also very useful tools for classification purposes. We have selected methods which are, in our opinion, most commonly used for engineering purposes [6] and [15]. In the following paragraphs brief explanations of different classification methods are given.

### 2.1 Support vector machines

Support vector machines (SVM) create a separating hyperplane between classes in  $N$ -dimensional space [38]. The optimal separating hyperplane is determined via a maximal margin between a small amount of selected observations, referred to as support vectors. Estimation of the SVM based classification was carried out using the *e1071* R package [39] which is an interface to the LIBSVM C++ library [40]. The function used for SVM based classification was **svm** with all parameters kept to a default value for both simplicity and a reduction in computational time.

### 2.2 Artificial Neural Networks

An artificial neural network (ANN) is a classification method which mimics brain structure and information processing in the brain [18]. The structure of a neural network is represented as layers of connected neurons. The structure can be divided into three layers, input layer, hidden layer and output layer. Hidden layer can additionally have more sub layers for more complex information processing, commonly referred to as deep networks. Used R package in this study is *nnet* package [41] and [42], which offers modeling of single hidden layer neural networks. Used function in the *nnet* package was **nnet** with all parameters kept to default value.

### 2.3 *k*-nearest neighbor

KNN method uses votes of nearest observations with a known class affiliation to decide the class membership of a new observation with an unknown class affiliation [43]. The class with the most votes amongst the *k*-nearest observations is chosen as the class membership of new observations. For the KNN classification method the R package used is *FNN* [44]. The function used in the *fnn* package was **fnn**. The user specified input parameter needed for this classification was the number of nearest neighbors used in the voting stage. The number of nearest neighbors was selected based on the minimal training error. The number of considered nearest neighbors was 2, 5, 10, 15, and 20.

Table 2 summarizes the main advantages and disadvantages of selected non-parametric classification methods.

**Table 2.** Properties of different non-parametric classification methods

Method	Properties	
svm	pros	less parameters, less memory intensive, intuitive, rapid
	cons	black-box method, less flexible
nnet	pros	more flexible, can have multiple hidden layers (deep neural networks)
	cons	black-box method, more parameters, can produce overfit, generally slower, more memory intensive
knn	pros	simple, intuitive
	cons	least flexible, most memory intensive (dataset needs to be stored), can be time consuming

## 3 PERFORMANCE EVALUATION AND FEATURE EXTRACTION

### 3.1 Performance Evaluation of Classification Method

For a reliable estimation of the performance measures for a classification method on a single dataset, multiple repetitions of the classification with different perturbations of the dataset are needed. One of the techniques mentioned earlier which can be used for this purpose is *k*-fold cross validation [45]. The dataset is split into *k* equally sized subsets (as opposed to random splitting where the data may, for example, be split 70 % and 30 %). All *k* subsets are then used for testing and training purposes. If the dataset is additionally randomly perturbed, different subsets can be obtained and we can perform multiple *k*-fold cross validations.

Most of the measures of fit used in evaluating the performance of classification with a particular method can be found in [46] and [47]. Different measures of fit certainly reveal different aspects of the performance of classification methods. Furthermore, by obtaining multiple values through multiple repeated *k*-fold cross validation of that measure of fit, some useful statistic such as the mean or median can be extracted and used for comparison, as can be seen in Meyers comparison of support vector machines [48].

For the evaluation of performance in a single turn of cross validation, two measures are used. The first is a classification error. The classification error is widely accepted and commonly used measure of fit that is appropriate as a general purpose measure of fit for classification tasks. It is defined as the percentage of wrongly classified observations from a certain dataset in the classification problem. A smaller classification error generally yields a better performance. The other performance measure used here was the computation time of the training and testing phases.

Multiple repeated *k*-fold cross validation yields multiple values of the classification errors and computation times. From the results of multiple repeated *k*-fold cross validation useful statistics can be derived such as, mean or standard deviation (std) of classification errors or computational times. This statistics can give more appropriate representation of the performance versus the single value which is usually obtained with random split of the dataset into train/test datasets.

### 3.2 Feature Extraction and Construction of Classification Datasets

For this study two different datasets for the bearing-fault classification were used. The first dataset is the widely used and known *Case Western Reserve University* (CWRU) dataset [16]. The second one is the bearing-vibration data under the time-varying rotational speed (VRSB) dataset [17]. All the datasets represent time-series vibration data collected from normal healthy bearings and a faulty bearing with different fault conditions, such as inner/outer race defects or ball defects. The CWRU dataset contains vibrational data for normal/healthy bearings along with vibrational data for bearings with an inner race, outer race and ball defects. The testing is made on 6205-2RS JEM SKF, deep groove ball bearing and 6203-2RS JEM SKF, deep groove ball bearing. Testing load ranged from 0 Nm to 2205 Nm and the testing speed ranged from 1730 r/min to 1797 r/min. Fault sizes were following: 0.1778 mm, 0.3556 mm,

**Table 3.** Used statistics for the feature extraction process

Statistic	Equation	Statistic	Equation	Statistic	Equation
Root mean square	$RMS = \sqrt{\frac{1}{N} \sum_{i=1}^N x_i^2}$	Crest factor	$CF = \frac{\max(x_i)}{RMS}$	Kurtosis factor	$KF = \frac{KV}{RMS^4}$
Square root of the amplitude	$SRA = \left(\frac{1}{N} \sum_{i=1}^N \sqrt{ x_i }\right)^2$	Impulse factor	$IF = \frac{N \max(x_i)}{\sum_{i=1}^N  x_i }$	Frequency center	$FC = \frac{1}{N} \sum_{i=1}^N f_i$
Kurtosis value	$KV = \frac{1}{N} \sum_{i=1}^N \left(\frac{x_i - \mu_x}{\sigma_x}\right)^4$	Margin factor	$MF = \frac{\max(x_i)}{SRA}$	Root-mean-square frequency	$RMSF = \sqrt{\frac{1}{N} \sum_{i=1}^N f_i^2}$
Skewness value	$SV = \frac{1}{N} \sum_{i=1}^N \left(\frac{x_i - \mu_x}{\sigma_x}\right)^3$	Shape factor	$SF = \frac{\max(x_i)}{SV}$	Root variance frequency	$RVF = \sqrt{\frac{1}{N} \sum_{i=1}^N (f_i - FC)^2}$
Peak-to-peak value	$PPV = \max(x_i) - \min(x_i)$				

0.5334 mm and 0.7112 mm. The other dataset contains only vibrational data for normal/healthy bearings and vibrational data of bearings with with inner-race and outer-race defects. The bearing used for testing was ER16K ball bearing. In previous studies [6], [15] and [49] a plethora of features that could be extracted

from the vibrational data were studied, specifically from the time domain, frequency domain or the time-frequency domain using various signal-processing tools such as the Fourier transform, Hilbert transform, Wavelet transform, etc. The feature-extraction part can greatly enhance the results of the classification

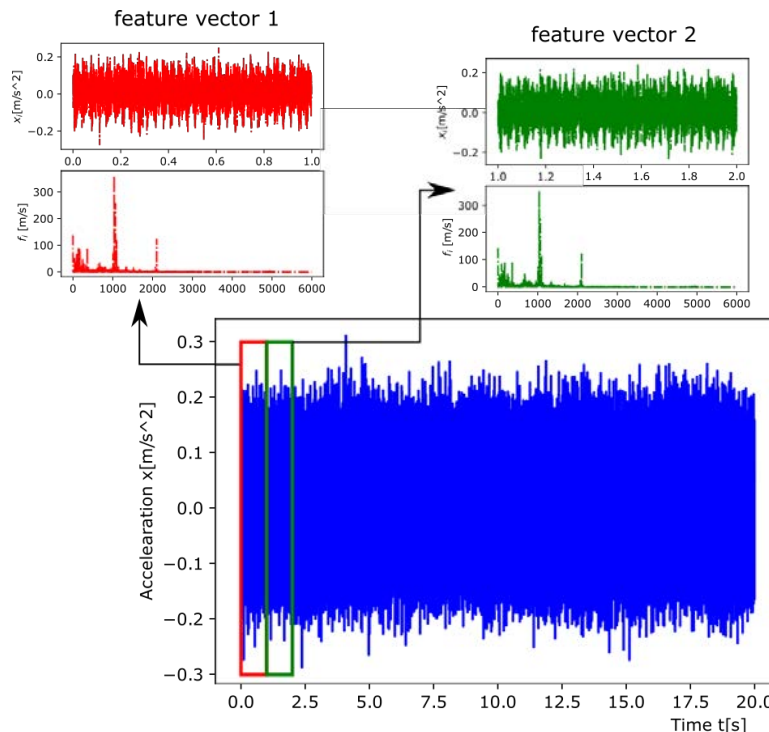


**Fig. 2.** Feature-extraction process from the vibrational data of a healthy bearing of the Case Western Reserve University dataset

and there is a lot of studies emerging on this topic [50]. However, since this paper represents the application of a classification method and its variants to one of the most dominant problems in the field of bearing and rotating-machinery fault detection we will simplify the feature-extraction process to only the statistical features of the vibrational signals in the time and frequency domains.

This resulted in thirteen different most popular statistical features, judging by the literature [6], [15] and [49]. Features are given in Table 3, where  $x_i$  is the  $i^{\text{th}}$  amplitude of the acceleration signal,  $N$  is the number of samples in the signal,  $\mu_x$  is the mean value of the signal,  $\sigma_x$  is the standard deviation of the signal,  $f_i$  is the corresponding  $i^{\text{th}}$  frequency amplitude.

To construct the classification datasets with the presented statistical features an interval of 1s is used, Fig. 2. For example, the CWRU dataset contains signals with a length of 20 s sampled at 12,000 samples per second (sps) or sampled at 48,000 sps. Those signals resulted in 20 instances for the CWRU classification dataset. Table 4 summarizes the characteristics of the constructed classification datasets.

**Table 4.** Used data sets

	Number of instances	Number of features	Number of classes
CWRU	1906	14	4
VSBD	360	14	3

Fig. 3 gives the pseudo code of the algorithm flow for the evaluation of classification methods.

Input: vibrational data, classification method,  
 number of folds  $k$ , number of repeats  $r$ ;  
 Output: classification errors  $E$  and evaluations times  $T$ ;  
 1: Extract the features from vibrational data;  
 2: do:  
 3: set random partitioning scheme  $i$ ;  
 4: split the input dataset into  $k$  subsets;  
 5: do:  
 6: merge  $(k - 1)$  subsets so that  $j$  subset is left out;  
 7: estimation time  $t_i$  = estimate classification model;  
 8: evaluation time  $t_e$ , classification error  $e$  =  
 evaluate model on  $j$  subset;  
 9: total time  $t = t_i + t_e$ ;  
 10: merge solution  $e$  and  $t$  into result arrays  $E$  and  $T$ ;  
 11: while  $j < k$ ;  
 12: while  $i < r$ ;

**Fig. 3.** Evaluation of classification method using the multiple repeated  $k$ -fold cross validation

## 4 RESULTS AND DISCUSSION

First, let us address the parameters used for the multiple repeated  $k$ -fold cross validation. The number  $k$  of folds was set to 5. The number of random perturbations of the datasets was set to 10, meaning that for each dataset the methods were applied 50 times and 50 different values of the classification errors and computational times were acquired. Those results were illustrated using box-plots. A box-plot represents the distribution of the data, where the boundaries of the box represent the 25 % and 75 %. The line inside the box represents the median value of that distribution. Additionally, for each dataset and classification method the mean value and standard deviation are given in tables.

### 4.1 CWRU Classification Dataset

The results are given in Fig. 4 and Table 5. The results of the classification errors (Fig. 4a plot) yielded three clusters of performers. Standalone *rbmix* gave the worst performance with respect to the accuracy of the classification. The best performers were the methods *nnet* and *rbmix&em*. The methods *mda*, *mclust*, *svm* and *nnet* were the average performers. On other hand, judging by the computational times (Fig. 4b) the *rbmix* method was the fastest method, performing 2 to 10 times faster than other methods. The *nnet* and *svm* methods yielded equal performance with respect to the computational time and were the second-fastest performing methods. A comparison of only the GMM-based classification methods on the CWRU dataset yielded *rbmix&em* as the best-performing method. This method yielded the smallest values of the classification error, while preserving the shortest computational times, judging by the mean values and standard deviations in Table 5.

**Table 5.** Mean and standard deviation of the results on the CWRU dataset

Method	Error [%] mean (std)	Time [s] mean (std)
<i>mda</i>	23.22 (2.67)	0.42 (0.41)
<i>mclust</i>	24.34 (2.80)	0.48 (0.45)
<i>rbmix</i>	34.85 (2.78)	0.05 (0.05)
<i>rbmix&amp;em</i>	9.89 (3.15)	0.27 (0.35)
<i>knn</i>	23.97 (1.88)	0.36 (0.33)
<i>svm</i>	21.77 (2.19)	0.09 (0.08)
<i>nnet</i>	10.32 (2.61)	0.10 (0.10)

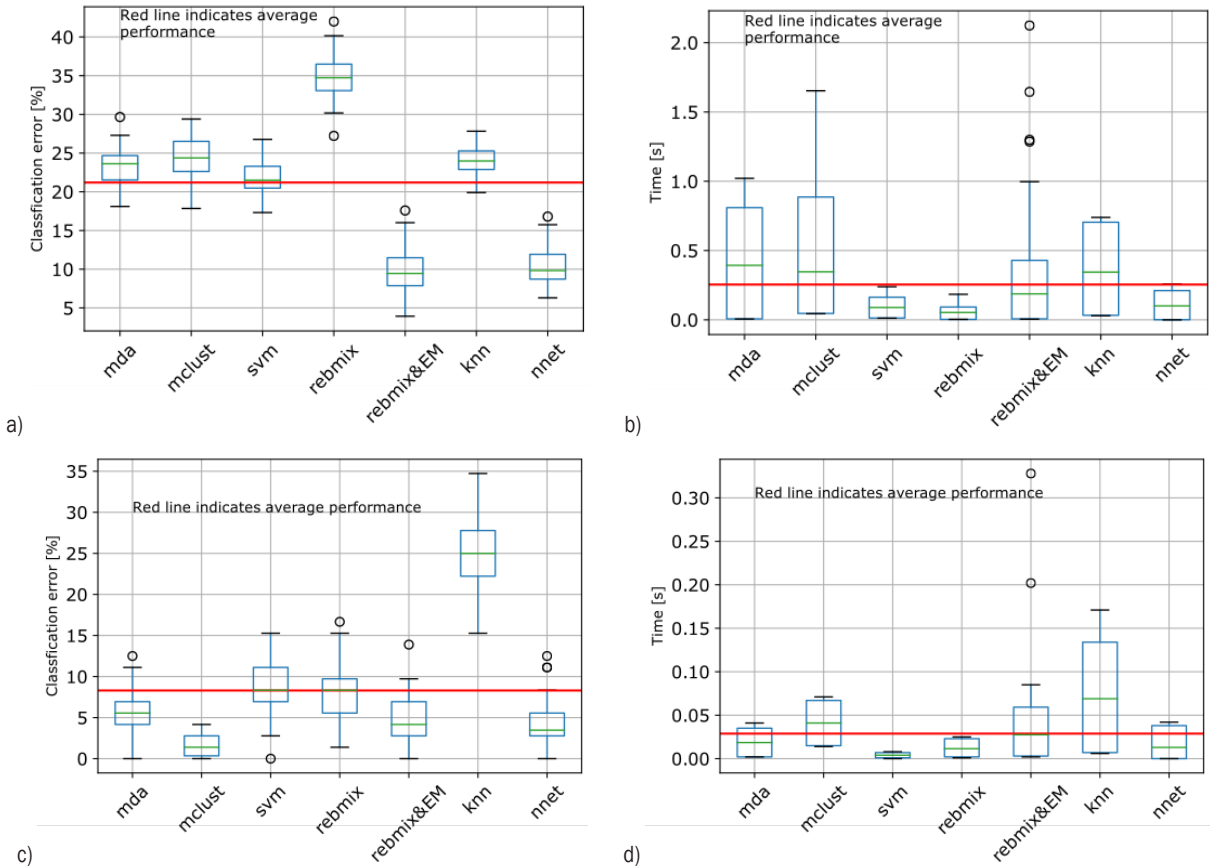


**Fig. 4.** Box-plots of a) classification errors, and b) computational times on CWRU dataset, c) classification errors, and d) computational times on VSBD dataset

Although, the standalone *rebmix* method had convincingly the shortest computational time, the results of the classification error were much larger than the other GMM classification methods, which deteriorates the overall performance of the *rebmix* method. The *nnet* method gave the best overall performance on the CWRU dataset. The method gave fast results while preserving almost the smallest classification error.

**4.2 VSBD Classification Dataset**

The results for the VSBD dataset are given in Fig. 4 and Table 6. Judging by the box-plots of the classification errors (Fig. 4c) the best performer was the *mclust* method. The worst performer was the *knn* method.

Additionally, the average performers can be placed into two clusters: the first one consisting of the methods *svm* and *rebmix*, which gave a slightly worse performance, and the methods *mda*, *nnet* and *rebmix&em*, which gave a slightly better performance.

Judging by the box-plots of the computational times (Fig. 4d), the method *svm* had the best performance, while *knn* had the worst performance. The methods *rebmix* and *nnet* had equal performance, which was a little better than the average performance and the methods *mda*, *mclust* and *rebmix&em* gave an average performance.

**Table 6.** Mean and standard deviation of results on VSBD dataset

Method	Error [%] mean (std)	Time [s] mean (std)
mda	5.72 (2.67)	0.02 (0.02)
mclust	1.58 (1.21)	0.04 (0.03)
rebmix	7.83 (3.47)	0.01 (0.01)
rebmix&em	4.69 (2.79)	0.04 (0.04)
knn	25.25 (4.67)	0.07 (0.06)
svm	8.94 (3.45)	0.003 (0.003)
nnet	4.11 (2.74)	0.01 (0.01)

On the VSBD dataset all the methods were extremely fast. This can be linked to the small number

of instances in the VSBD dataset. Therefore, the computation time has a far smaller impact than in the case of the CWRU dataset. The best-performing method of the GMM classification methods was the *mclust* method, although the *mda* and *rbmix* methods had smaller values of the mean and the standard deviation of the computation time (see Table 6). In the overall comparison, the *nnet* method had a slight deterioration in performance with respect to the classification errors, while it preserved the above-average value of the computational time.

## 5 CONCLUSIONS

In this work we have investigated the performance of different GMM-based classification methods on the problem of the bearing-fault classification. The performance was evaluated on two publicly available datasets with bearing-vibrational data. To construct the classification datasets out of which the bearing faults can be classified, we used just simple processing techniques and only statistical features from the data are estimated. We opted out of using more complicated signal-processing techniques, for example, the wavelet transform, because of the pure simplicity. If the classification method can perform well on extracted simple statistics, it will perform even better on more sophisticated ones. Therefore, the general applicability is evaluated.

From the results obtained on both datasets one of the GMM-based classification method variants had the best results: on the CWRU dataset the *rbmix&EM* method and on the VSBD the *mclust* method. Although the variants of the GMM based classification did not yield the most satisfying results for the computational time, this was mostly caused by the slow convergence of the EM algorithm. Since there is a lot of effort in the research for speeding up the convergence of the EM algorithm [24], this can be utilized to improve the computational dependency of the GMM-based classification methods. On other hand, standalone *rbmix* proved to be fast variant, although the other results were unsatisfying. As expected, the *nnet* method gave a good trade off between accuracy and computational time on both used datasets, which ultimately positioned it as a serious rival to GMM based methods.

We will end this article by providing some insights into our future work. Different speeding-up techniques of the EM algorithm along with different pre-processing techniques for the REBMIX algorithm will be tested. Finally, more datasets for the engineering-based classification tasks will be tested.

## 6 ACKNOWLEDGEMENTS

The authors acknowledge the financial support from the Slovenian Research Agency (research core funding No. 1000-18-0510).

## 7 REFERENCES

- [1] Salehi, H., Burgueño, R. (2018). Emerging artificial intelligence methods in structural engineering. *Engineering Structures*, vol. 171, p. 170-189, DOI:10.1016/j.engstruct.2018.05.084.
- [2] Nasiri, S., Khosravani, M.R., Weinberg, K., (2017). Fracture mechanics and mechanical fault detection by artificial intelligence methods: A review. *Engineering Failure Analysis*, vol. 81, p. 270-293, DOI:10.1016/j.engfailanal.2017.07.011.
- [3] Rabcan, J., Levashenko, V., Zaitseva, E. Kvassay, M., Subbotin, S. (2019). Non-destructive diagnostic of aircraft engine blades by fuzzy decision tree. *Engineering Structures*, vol. 197, p. 109396, DOI:10.1016/j.engstruct.2019.109396.
- [4] Hasni, H., Alavi, A.H., Lajnef, N., Abdelbarr, M. Masri, S.F., Chakrabarty, S. (2017). Self-powered piezo-floating-gate sensors for health monitoring of steel plates. *Engineering Structures*, vol. 148, p. 584-601, DOI:10.1016/j.engstruct.2017.06.063.
- [5] Mangalathu, S., Jeon, J.-S. (2018). Classification of failure mode and prediction of shear strength for reinforced concrete beam-column joints using machine learning techniques. *Engineering Structures*, vol. 160, p. 85-94, DOI:10.1016/j.engstruct.2018.01.008.
- [6] Pan, H., He, X., Tang, S., Meng, F. (2018). An improved bearing fault diagnosis method using one-dimensional CNN and LSTM. *Strojniški vestnik - Journal of Mechanical Engineering*, vol. 64, no. 7-8, p. 443-452, DOI:10.5545/sv-jme.2018.5249.
- [7] Do, V.T., Nguyen, L.C. (2016). Adaptive empirical mode decomposition for bearing fault detection. *Strojniški vestnik - Journal of Mechanical Engineering*, vol. 62, no. 5, p. 281-290, DOI:10.5545/sv-jme.2015.3079.
- [8] Nejad, A.R., Odgaard, P.F., Gao, Z., Moan, T. (2014). A prognostic method for fault detection in wind turbine drivetrains. *Engineering Failure Analysis*, vol. 42, p. 324-336, DOI:10.1016/j.engfailanal.2014.04.031.
- [9] Liu, W.Y. (2013). The vibration analysis of wind turbine blade-cabin-tower coupling system. *Engineering Structures*, vol. 56, p. 954-957, DOI:10.1016/j.engstruct.2013.06.008.
- [10] Cheng, L.Z., Liu, D.K., Wang, Y., Chen, A.Q. (2019). Load distribution and contact of axle box bearings in electric multiple units. *International Journal of Simulation Modelling*, vol. 18, no. 2, p. 290-301, DOI:10.2507/IJSIMM18(2)475.
- [11] Edler, J., Tic, V., Lovrec, D. (2019). 1-D simulation model of a progressive flow controller for hydrostatic bearings. *International Journal of Simulation Modelling*, vol. 18, no. 2, p. 267-278, DOI:10.2507/IJSIMM18(2)472.
- [12] Liu, J. (2020). A dynamic modelling method of a rotor-roller bearing-housing system with a localized fault including the additional excitation zone. *Journal of Sound and Vibration*, vol. 469 p. 115144, DOI:10.1016/j.jsv.2019.115144.
- [13] Lu, S., Zheng, P., Liu, Y., Cao, Z., Yang, H., Wang, Q. (2019). Sound-aided vibration weak signal enhancement for bearing

- fault detection by using adaptive stochastic resonance. *Journal of Sound and Vibration*, vol. 449, p. 18-29, DOI:10.1016/j.jsv.2019.02.028.
- [14] Li, Y., Yang, Y., Wang, X., Liu, B., Liang, X. (2018). Early fault diagnosis of rolling bearings based on hierarchical symbol dynamic entropy and binary tree support vector machine. *Journal of Sound and Vibration*, vol. 428, p. 72-86, DOI:10.1016/j.jsv.2018.04.036.
- [15] Sobie, C., Freitas, C., Nicolai, M. (2018). Simulation-driven machine learning: Bearing fault classification. *Mechanical Systems and Signal Processing*, vol. 99, p. 403-419, DOI:10.1016/j.ymssp.2017.06.025.
- [16] Loparo, K. (1998). Bearings vibration data set, Cast Western Reverse University, from: <https://cseggroups.case.edu/bearingdatacenter/home>, accessed on 2019-12-12.
- [17] Huang, H., Baddour, N., (2018). Bearing vibration data collected under time-varying rotational speed conditions. *Data in Brief*, vol. 21, p. 1745-1749, DOI:10.1016/j.dib.2018.11.019.
- [18] Bishop, C. (2006). *Pattern Recognition and Machine Learning*, Springer-Verlag, Berlin, Heidelberg.
- [19] Fisher, R.A. (1936). The use of multiple measurements in taxonomic problems. *Annual Eugenics*, vol. 7, no. 2, p. 179-188, DOI:10.1111/j.1469-1809.1936.tb02137.x.
- [20] Rao, C.R. (1948). The utilization of multiple measurements in problems of biological classification. *Journal of the Royal Statistical Society. Series B (Methodological)*, vol. 10, no. 2, p. 159-203, DOI:10.1111/j.2517-6161.1948.tb00008.x.
- [21] Hastie, T., Tibshirani, R. (1996). Discriminant analysis by gaussian mixtures. *Journal of the Royal Statistical Society. Series B (Methodological)*, vol. 58, no. 1, p. 155-176, DOI:10.1111/j.2517-6161.1996.tb02073.x.
- [22] Escobar, M.D., West, M. (1995). Bayesian density estimation and inference using mixtures. *Journal of the American Statistical Association*, vol. 90, no. 430, p. 577-588, DOI:10.1080/01621459.1995.10476550.
- [23] Roeder, K., Wasserman, L. (1997). Practical Bayesian density estimation using mixtures of normals. *Journal of the American Statistical Association*, vol. 92, no. 439, p. 894-902, DOI:10.1080/01621459.1997.10474044.
- [24] McLachlan, G., Peel, D. (2000). *Finite Mixture Models*, John Wiley and Sons, New York, DOI:10.1002/0471721182.
- [25] Dempster, A.P., Laird, N.M., Rubin, D.B., (1977). Maximum likelihood from incomplete data via the EM algorithm. *Journal of the royal statistical society, Series B (Methodological)*, vol. 39, no. 1, p. 1-38, DOI:10.1111/j.2517-6161.1977.tb01600.x.
- [26] Melnykov, V., Melnykov, I. (2012). Initializing the EM algorithm in gaussian mixture models with an unknown number of components. *Computational Statistics and Data Analysis*, vol. 56, no. 6, p. 1381-1395, DOI:10.1016/j.csda.2011.11.002.
- [27] Nagode, M. (2015). Finite mixture modeling via REBMIX. *Journal of Algorithms and Optimization*, vol. 3, no. 2, p. 14-28, DOI:10.5963/JA0030200.
- [28] Ye, X.W., Xi, P.S., Nagode, M. (2019). Extension of REBMIX algorithm to von Mises parametric family for modeling joint distribution of wind speed and direction. *Engineering Structures*, vol. 183, p. 1134-1145, DOI:10.1016/j.engstruct.2018.08.035.
- [29] Biernacki, C., Celeux, G., Govaert, G. (2000). Assessing a mixture model for clustering with the integrated completed likelihood. *IEEE Transactions on Pattern Analysis and Machine Intelligence*, vol. 22, no. 7, p. 719-725, DOI:10.1109/34.865189.
- [30] R Core Team, 2014, R: A Language and Environment for Statistical Computing, R Foundation for Statistical Computing, Vienna, Austria, from: <http://www.R-project.org/>, accessed on 2019-12-12.
- [31] Hastie, T., Tibshirani, R., Leisch, F., Hornik, K., Ripley, B.D. (2017). mda: Mixture and Flexible Discriminant Analysis, from: <https://CRAN.R-project.org/package=mda>, accessed on 2019-12-12.
- [32] Scrucca, L., Fop, M., Murphy, T.B., Raftery, A.E. (2016). mclust 5: Clustering, classification and density estimation using Gaussian finite mixture models. *The R Journal*, vol. 8, no. 1, p. 205-233, DOI:10.32614/RJ-2016-021.
- [33] Celeux, G., Govaert, G. (1995). Gaussian parsimonious clustering models. *Pattern Recognition*, vol. 28, no. 5, p. 781-793, DOI:10.1016/0031-3203(94)00125-6.
- [34] Scrucca, L., Raftery, A.E. (2015). Improved initialisation of model-based clustering using Gaussian hierarchical partitions. *Advances in Data Analysis and Classification*, vol. 9, no. 4, p. 447-460, DOI:10.1007/s11634-015-0220-z.
- [35] Nagode, M., Panić B. (2019). Finite Mixture Modeling, Clustering & Classification, from: <https://cran.r-project.org/web/packages/rebmix>, accessed on 2019-12-12.
- [36] Nagode, M., (2018), Multivariate normal mixture modeling, clustering and classification with the rebmix package. *ArXiv e-prints*, arXiv:1801.08788.
- [37] Panić, B., Klemenc, J., Nagode, M. (2020). Improved initialization of the EM algorithm for mixture model parameter estimation. *Mathematics*, vol. 8, no. 3, p. 373, DOI:10.3390/math8030373.
- [38] Cortes, C., Vapnik, V. (1995). Support-vector networks. *Machine Learning*, vol. 20, no. 3, p. 273-297, DOI:10.1023/A:1022627411411.
- [39] Meyer, D., Dimitriadou, E., Hornik, K., Weingessel, A., Leisch, F. (2018). e1071: Misc Functions of the Department of Statistics, Probability Theory Group, from: <https://cran.r-project.org/web/packages/e1071>, accessed on 2019-12-12.
- [40] Chang, C., Lin, C. (2011). LIBSVM: A library for support vector machines. *ACM Transactions on Intelligent Systems and Technology*, vol. 2, no. 3, p. 27:1-27:27, DOI:10.1145/1961189.1961199.
- [41] Ripley, B. (2017). Feed-Forward Neural Networks and Multinomial Log-Linear Models, from: <https://cran.r-project.org/web/packages/nnet>, accessed on: 2019-12-12.
- [42] Venables, W.N., Ripley, B.D. (2002). *Modern Applied Statistics with S*, Springer, New York.
- [43] Altman, N.S. (1992). An introduction to Kernel and nearest-neighbor nonparametric regression. *The American Statistician*, vol. 46, no. 3, p. 175-185, DOI:10.1080/00031305.1992.10475879.
- [44] Beygelzimer, A., Kakadet, S., Langford, J., Arya, S., Mount, D, Li, S. (2018). fnn: Fast nearest neighbor search algorithms and applications, from: <https://cran.r-project.org/web/packages/FNN/>, accessed on: 2019-12-12.

- [45] Hastie, T., Tibshirani, R., Friedman, J. (2009). *The Elements of Statistical Learning*, Springer New York, DOI:10.1007/978-0-387-84858-7.
- [46] Sokolova, M., Lapalme, G. (2009). A systematic analysis of performance measures for classification tasks. *Information Processing & Management*, vol. 45, no. 4, p. 427-437, DOI:10.1016/j.ipm.2009.03.002.
- [47] Ferri, C., Hernández-Orallo, J., Modroiu, R. (2009). An experimental comparison of performance measures for classification. *Pattern Recognition Letters*, vol. 30, no. 1, p. 27-38, DOI:10.1016/j.patrec.2008.08.010.
- [48] Meyer, D., Leisch, F., Hornik, K. (2003). *Benchmarking Support Vector Machines*, Report Series, Vienna.
- [49] Li, H., Liu, T., Wu, X., Chen, Q. (2019). Research on bearing fault feature extraction based on singular value decomposition and optimized frequency band entropy. *Mechanical Systems and Signal Processing*, vol. 118, p. 477-502, DOI:10.1016/j.ymssp.2018.08.056.
- [50] Liu, J., Xu, Z., Zhou, L., Yu, W., Shao, Y. (2019). A statistical feature investigation of the spalling propagation assessment for a ball bearing. *Mechanism and Machine Theory*, vol. 131, p. 336-350, DOI:10.1016/j.mechmachtheory.2018.10.007.

# Deep Stacked Auto-Encoder Network Based Tool Wear Monitoring in the Face Milling Process

VanThien Nguyen – VietHung Nguyen\* – VanTrinh Pham  
Hanoi University of Industry, VietNam

*Tool wear identification plays an important role in improving product quality and productivity in the manufacturing industry. The actual tool wear status with input cutting parameters may cause different levels of spindle vibration during the machining process. This research proposes an architecture comprising a deep learning network (DLN) to identify the actual wear state of machining tool. Firstly, data on spindle vibration signals are obtained from an acceleration sensor. The data are then pre-processed using the fast Fourier transform (FFT) method to reveal the relevant outstanding features in the frequency domain. Finally, the DLN is constructed based on stacked auto-encoders (SAE) and softmax, which is trained with the input data on the vibration features of the respective tool wear state. This DLN architecture is then used to identify the actual wear statuses of machining tool. The experimental results from the collected data show that the proposed DLN architecture is capable of identifying actual tool wear with high accuracy.*

**Keywords:** Face milling; Tool wear; Stacked auto-encoder (SAE); Deep learning network (DLN); Cast iron

## Highlights

- An expert technique for tool wear monitoring based on an experimental dataset is explored.
- The feature values with respect to the wear status of cutting tools are extracted and analyzed.
- The effects of a proposed deep learning network architecture for identifying the different tool wear statuses are considered.
- A patterns prediction method is compared and developed.

## 0 INTRODUCTION

In the machining process, cutting tool play an important role and can affect the stability of machine components and systems. Cutting tool status is closely related to the vibration, cutting heat and cutting force of a machining system, which normally includes the machine tool, cutting tool, workpiece, and clamping device. The working status of a cutting tool significantly influences machining efficiency and thus the accuracy of a product [1] to [3]. Therefore, monitoring cutting tool status is important. Normally, tool wear can cause major failure of the cutting tool, which may result in wastage of a product, slow operation, and a lack of productivity. Identifying the wear status of cutting tool is especially important in evaluating product accuracy [4] and [5].

The features of the original vibration signal can provide useful information for assessing the wear condition of cutting tool and can be extracted by principal component analysis (PCA) [6] and linear discriminate analysis (LDA) [7] and [6]. Dimensional feature data, in particular, can cause a computational burden, affect the efficiency of the classification phase as it is time-consuming, and reduce the diagnosis accuracy. These methods are effective with linear data but cannot be effectively applied for complex nonlinear and nonstationary vibration data.

Machine learning techniques have been researched and applied in many fields of science and technology, such as computer vision, automatic diagnostics systems and pattern recognition. These techniques are often based on artificial intelligence methods such as k- nearest neighbour (K-NN) [8], support vector machines (SVM) [9] and [10], and the artificial neural network (ANN) [11] to [13]. These methods have been effectively applied to identify tool wear status. However, they have some weaknesses, including ineffective feature extraction. In particular, the objectivity of unsupervised feature learning has been ignored, and automation is not employed in these methods [14] and [15]. Therefore, using these techniques to identify tool wear in the machining process has been unsatisfactory.

Recently, deep learning network (DLN) architecture has been widely used in research [16] and some engineering science applications such as medical informatics [17], pattern recognition [18] and [19], and time-series prediction [20] to [22]. DLNs are hierarchically constructed with many hidden layers with the aim of effectiveness in the output layer [23]. In this study, the authors propose a DLN architecture based on the SAE and softmax classifier, which are closely stacked together to implement tool wear diagnosis in the end-milling process. In this architecture, each auto-encoder (AE) implements vibration data reconstruction to generate higher-

level features with an unsupervised algorithm that is optimized to minimize errors between the input and output data. The relevant vibration features are precisely extracted at the hidden layer of the last AE, which can significantly improve the learning effect of the classification phase. In addition, softmax is derived from the multinomial logistic model, which is based on the supervised learning algorithm and is suitable for multiclass classification [24]. Finally, the parameters of the proposed DLN will be fine-tuned with the supervised condition in its complete architecture, with the goal of effectiveness of the classification accuracy result.

The rest of the paper is structured as follows: Section 1 presents the materials. Section 2 proposes a DLN architecture, which is then used to identify tool wear status of the end-milling process. Section 3 presents experimental results and discusses the diagnosis results, which are analyzed and compared. Section 4 is the conclusion. Acknowledgments and a list of references then follow.

## 1 MATERIALS

This section expresses the single AE architecture and softmax classifier model that are the basis for constructing the DLN for the diagnosis technique. The AE is used to exploit the features of the original vibration signal related to tool wear status. These features are then used to train softmax classifier and construct the proposed DLN.

### 1.1 Auto-Encoder Network Architecture

In [23], AE is a special type of neural network architecture that acts as an unsupervised algorithm. The AE architecture consists of three layers instead of the input layer, the hidden layer and the output layer, which are organized into two phases -encoding and decoding- as shown in Fig. 1. The input layer  $x = \{x_1, x_2, \dots, x_n\}$ , hidden layer  $f = \{f_1, f_2, \dots, f_m\}$ ,  $m \ll n$ , and output layer  $\tilde{x} = \{\tilde{x}_1, \tilde{x}_2, \dots, \tilde{x}_n\}$  are seamlessly connected. This AE is implemented to reconstruct data of the input layer.

The encoder phase has encoded the characteristics of the high-dimensional input data  $x$  into the low-dimensional  $f$  data in the hidden layer. The input and hidden layers are connected by the activation function,  $f = Sigmoid(W^{(1)} \cdot x + b^{(1)})$ , in the mapping process, where  $W^{(1)}$  is the weight matrix and  $b^{(1)}$  is the bias vector. More specifically, each input vector  $x_i$  is mapped onto the hidden layer with the expression of significant, reduced features. In contrast, the decoder phase reconstructs the input layer  $x$ . Input data  $f$  is mapped back onto the output layer of  $\tilde{x}$  with high-dimensional reconstructed data. The activation function  $\tilde{x} = Sigmoid(W^{(2)} \cdot f + b^{(2)})$  is used to connect the hidden layer to output layer, where the weight matrix  $W^{(2)} = (W^{(1)})^T$  is interpreted as tied weights and  $b^{(2)}$  is the bias vector of the decoder phase. The AE is optimized architecture with parameter sets  $(W^{(1)}, W^{(2)}, b^{(1)}, b^{(2)})$  to minimize error of restructuring in the output layer. The following cost function is used:

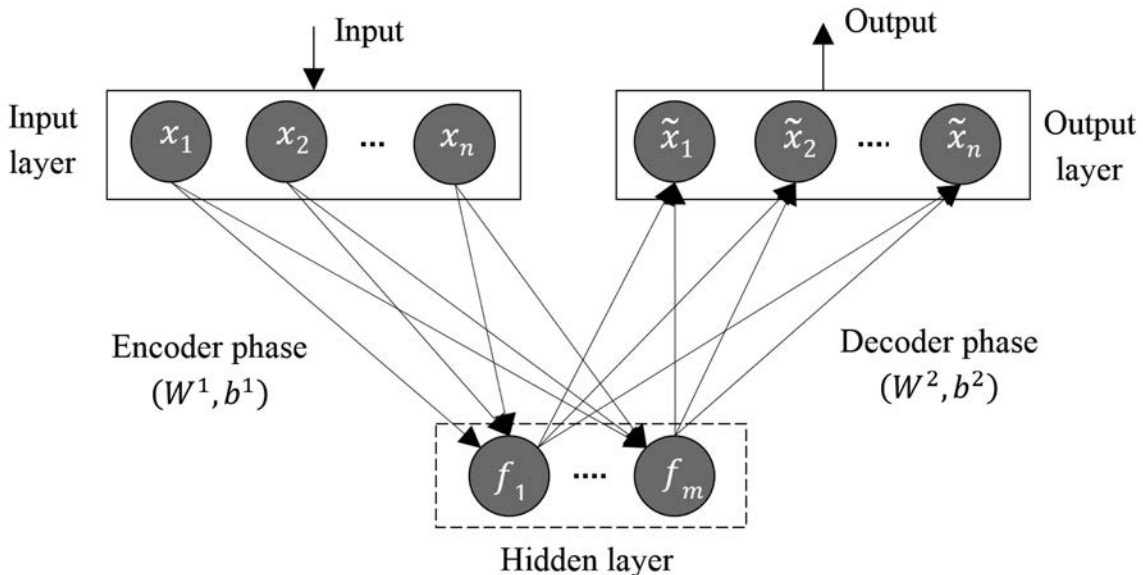


Fig. 1. Architecture of single AE network

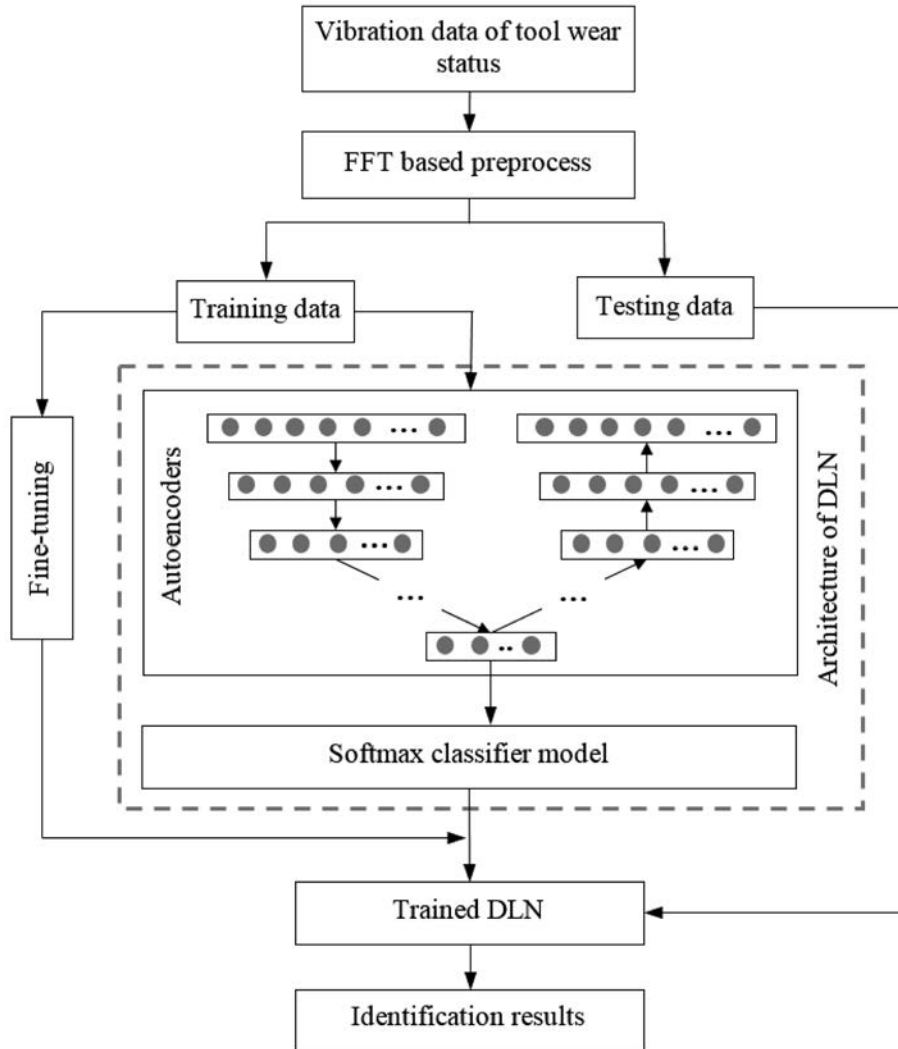


Fig. 2. Diagnosis technique based on DLN architecture

$$C = \frac{1}{N} \sum_n \sum_i \left( f_i^{(n)} - \tilde{f}_i^{(n)} \right)^2 + \lambda \cdot \Omega_w + \beta \cdot \Omega_s, \quad (1)$$

where  $i$  is the number of variables in input data;  $N$  is the number of samples;  $\lambda$  is the coefficient for the  $\Omega_w$ ;  $\beta$  is the coefficient for the  $\Omega_s$ ;  $\Omega_w$  is an  $L_2$  regularization term defined by Eq. (2); and  $\Omega_s$  is a sparsity regularization term defined by Eq. (3).

$$\Omega_w = \sum_l \sum_i \sum_j \left( W_{ij}^l \right)^2, \quad (2)$$

$$\Omega_s = \sum_l \sum_j KL(\rho \parallel p_j^k). \quad (3)$$

where  $p_j^k$  is the mean activation for unit  $j$  in layer  $k$ ;  $\rho$  is the desired mean activation; and  $KL$  is the Kullback-Leibler divergence, which is defined by Eq. (4).

$$KL(\rho \parallel p_j^k) = \rho \log \frac{\rho}{p_j^k} + (1 - \rho) \log \frac{1 - \rho}{1 - p_j^k}. \quad (4)$$

It can be seen that each AE is independently trained to represent the features. The features are extracted from hidden layer nodes that contain the most important information of the input layer. The extracted features can be input data for the next AE to produce higher-level features.

### 1.2 Softmax Classifier Model

As a follow-up, training the softmax classifier model to identify patterns is a necessary step for the whole model of the diagnosis technique. The model uses the encoded feature data in the hidden layer of the

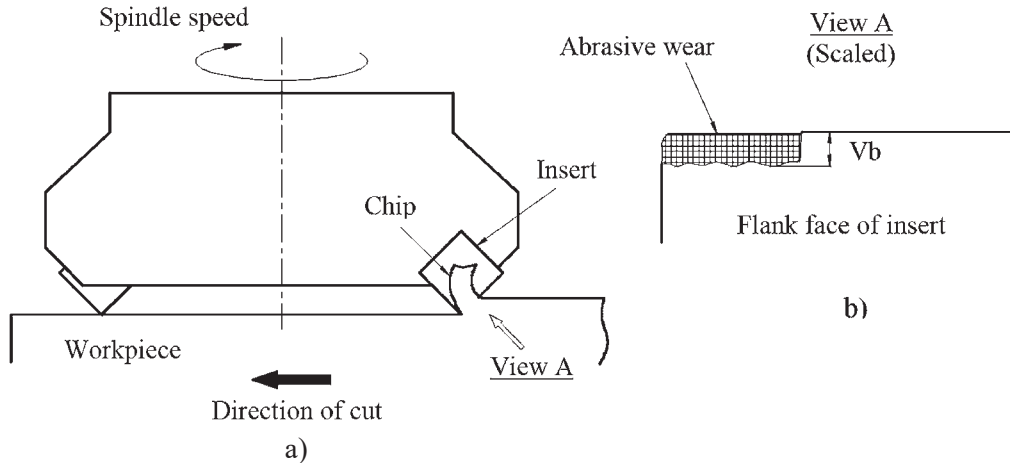


**Fig. 3.** Schematic drawing of face milling process; a) cutting zone at tool/workpiece interface, and b) observing of  $V_b$  tool wear on the insert

last AE. Softmax uses loss function based on cross entropy [16] and [23].

Softmax based on the supervised learning algorithm requires input samples  $x = \{x^{(1)}, x^{(2)}, \dots, x^{(n)}\}$  and class labels  $t = \{t^{(1)}, t^{(2)}, \dots, t^{(k)}\}$  for the classifier model. The training process for an input sample evaluates the probability:  $probability(t = j/x)$  for each value of  $j = 1, 2, \dots, k$ . This means that the probability of the class label is estimated by each of the  $k$  different possible values. Therefore, hypothesis function  $\mathcal{H}_\theta(x^{(i)})$  is constituted as follows:

$$\mathcal{H}_\theta(x^{(i)}) = \begin{bmatrix} probability(t^{(i)} = 1|x^{(i)}; \theta) \\ probability(t^{(i)} = 2|x^{(i)}; \theta) \\ \vdots \\ probability(t^{(i)} = k|x^{(i)}; \theta) \end{bmatrix} = \frac{1}{\sum_{j=1}^k \exp(\theta_j^T x^{(i)})} \begin{bmatrix} \exp(\theta_1^T x^{(i)}) \\ \exp(\theta_2^T x^{(i)}) \\ \vdots \\ \exp(\theta_k^T x^{(i)}) \end{bmatrix}, \quad (5)$$

where  $\theta_1, \theta_2, \dots, \theta_k \in R^{n+1}$  are the parameters of the softmax classifier, and the  $\frac{1}{\sum_{j=1}^k \exp(\theta_j^T x^{(i)})}$  term represents the normalization of the distribution.

AEs and softmax classifier are hierarchically stacked together to construct the diagnosis technique. This technique is then fine-tuned with all the parameters to optimize the whole model, which will be evaluated using a test dataset.

## 2 PROPOSED DIAGNOSIS TECHNIQUE

This section describes the DLN in the proposed diagnosis technique. The significant feature data is extracted from vibration data related to tool wear status by unsupervised algorithm-based AEs, which provides the softmax classifier with inputs. The combination of AEs with softmax in the proposed DLN architecture achieves the impressive diagnosis results. Vibration data in the frequency domain corresponding to tool wear status are inputs to the DLN. Fig. 2 shows diagnosis implementation, which comprises the following seven steps:

- Step 1:* Acquire vibration data based on cutting tool status.
- Step 2:* Pre-process the collected data by FFT in time domain to express data clearly in the frequency domain.
- Step 3:* Divide the training data-testing ratio for the diagnostic phase. The training data are then used to train the model. The testing data are used to evaluate the trained model.
- Step 4:* Exploit the important features in the hidden layer AE, which is based on an unsupervised algorithm.
- Step 5:* Train the softmax classifier model using the extracted features of the last AE. Arrange the AEs and softmax classifier in the DLN architecture.
- Step 6:* Train the gained DLN by fine-tuning all the parameters using the class label.
- Step 7:* Identify the actual status of tool wear by the trained DLN.

### 3 EXPERIMENTAL RESULTS

This section presents the experimental results, demonstrating the quality of the proposed method. The wear status of face milling tool is identified in the face milling process. Vibration data on the state of the tool is collected, and pre-processed before serving as input to the proposed method.

#### 3.1 Spindle Vibration Based Tool Wear Data Acquisition

The experimental dataset of BEST Lab at UC Berkeley is used to identify tool wear status [25]. The authors used a Matsuura machining center model MC-510V with a 70 mm face mill mounted with six inserts of the KC710 (Kennametal) type and a cast-iron milling workpiece is. The face milling operations dataset was experimented on different conditions, and the flank wear  $Vb$  values are verifiability measured, respectively. Fig. 3 is a schematic drawing of the face milling process. Vibration data was monitored by an accelerometer with a maximum sampling rate of 100 kHz. Table 1 shows a dataset of 40 samples. Samples were collected on machine spindle vibration corresponding to four tool wear states:  $Vb_0=0$  mm,  $Vb_1=0.11$  mm,  $Vb_2=0.29$  mm, and  $Vb_3=0.50$  mm,

which correspond to no tool wear, slightly worn tool, half worn tool, and severely worn tool, respectively. The acquired vibration data was recorded at the end of 2<sup>nd</sup>, 7<sup>th</sup>, 29<sup>th</sup>, and 44<sup>th</sup> minutes. Tool status was tested with the same cutting parameters at a spindle speed of 826 rpm, feed of 0.5 mm, and cutting depth of 1.5 mm. Fig. 4 shows these vibration signals in the time domain with four examples of corresponding wear statuses. The figure may imply that the vibration intensity that corresponds with cutting tool status is unclear and that the tool wear status cannot be determined even though the cutting parameter is unchanged.

**Table 1.** Tool wear statuses based vibration data

Cutting tool status	Training samples	Testing samples	Flank wear bandwidth [mm]	Class
Not worn $Vb_0$	$(x_1-x_5)$	$(x_6-x_{10})$	-	1
First worn $Vb_1$	$(x_{11}-x_{15})$	$(x_{16}-x_{20})$	0.11	2
Second worn $Vb_2$	$(x_{21}-x_{25})$	$(x_{26}-x_{30})$	0.29	3
Third worn $Vb_3$	$(x_{31}-x_{35})$	$(x_{36}-x_{40})$	0.50	4

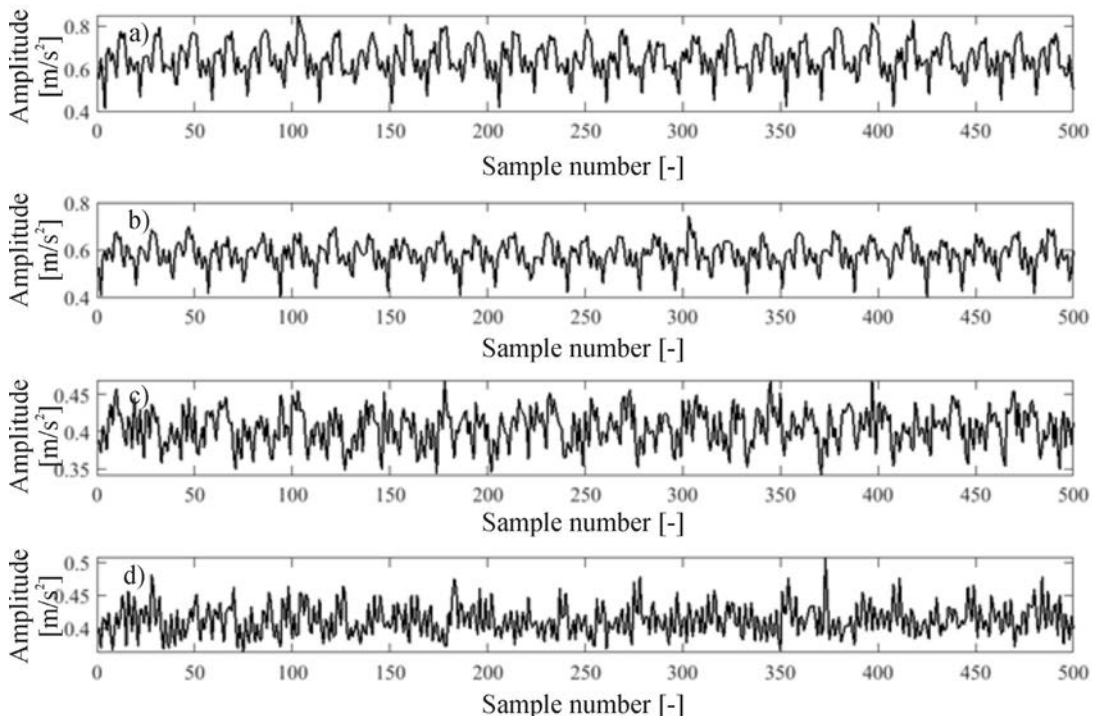


**Fig. 4.** Example of vibration signals use for cutting tool status determination; a) normal state; b) first-worn status; c) second-worn status, and d) third-worn status

### 3.2 Results and Discussion

To highlight the specific vibration frequencies of tool wear statuses, original time-domain vibration data was pre-processed and transformed into the frequency domain using the FFT method. These data were then used to extract the features of cutting tool status. The feature dataset of the vibration signal was extracted from two AEs, whose parameters are shown in Table 2.

**Table 2.** Parameter of AEs

	AE structure	$\lambda$	$\beta$
AE 1	512-20-512	0.05	6
AE 2	20-3-20	0.05	4

Table 3 shows the experimental results for identifying tool status. The results indicate each state of the cutting tool. The original vibration data were accurately identified by the class to which they belong. The diagnostic result for each tool wear status is 100 % accurate, which means that the expression of the unsupervised features of the original vibration signal exploited their efficient and important features. In this case, the combination of the optimized AE is related to Eq. (1) for the reconstruction of data with the softmax classifier model, which, according to the probability of Eq. (5) is very effective. Fig. 5 shows the confusion matrix for the four wear statuses of cutting tool (i.e.,  $Vb_0$ ,  $Vb_1$ ,  $Vb_2$ , and  $Vb_3$ ), which are the same class as determined by the model trained by previous training data.

**Table 3.** Results of tool wear identification based on our proposed method

Tool wear status	Testing data	Features			Results
1	$(x_6-x_{10})$	0.559913	0.010705266	0.007923	5(1)
2	$(x_{16}-x_{20})$	0.055347	0.336805625	0.012599	5(2)
3	$(x_{26}-x_{30})$	0.000139	0.000127181	0.000102	5(3)
4	$(x_{36}-x_{40})$	0.000108	9.24E-05	8.32E-05	5(4)
Training time [s]					0.3072
Accuracy [%]					100

To compare the identification results with the other classifiers, the authors constructed the shallow classifiers as the feed-forward neural network (FNN) classifier and a k-nearest neighbour (k-NN) classifier to identify tool wear status. The extracted three-dimensional feature data of the last AE was used to train and test the classifiers. An FNN classifier with

10 hidden layer, four output layer, and training error goal of 0.01 and a k-NN classifier with four nearest neighbours are formed to conduct the identification procedure. Table 4 shows the evaluation result of the FNN classifier and the k-NN classifier. The evaluation showed that the identification accuracy of both these classifiers was lower than the identification accuracy of the proposed DLN. It is known that the tool wear diagnosis technique, based on the proposed DLN, effects high-level feature representation in deep learning to gain high classification accuracy. Nevertheless, the perfect classification accuracy results for the proposed DLN come at a high price in terms of time compared to the only k-NN architecture, as the results in Table 3 and 4 show. This causes each phase of DLN construction to be optimized. Finally, the DLN based our proposed diagnosis technique is confirmed as efficient for feature representation and classification, which is illustrated in Fig. 6.

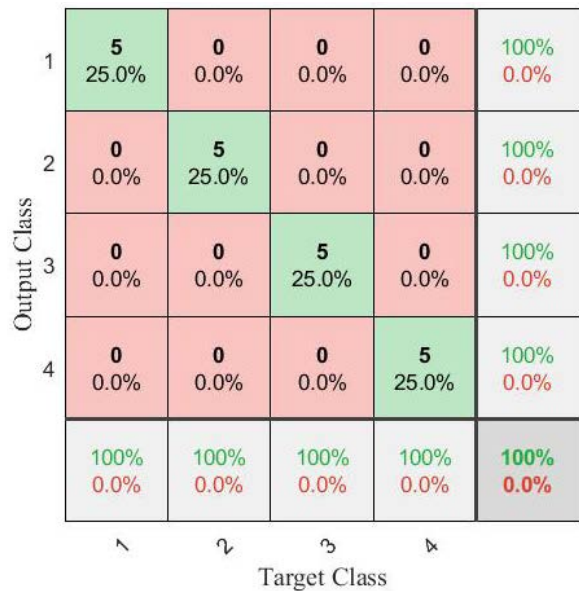


**Fig. 5.** Identification result confusion matrix

**Table 4.** Results of tool wear identification based on FNN and k-NN classifiers

Class	Testing data	FNN	k-NN
1	$(x_6-x_{10})$	5(1)	3(1)2(3)
2	$(x_{16}-x_{20})$	5(2)	5(2)
3	$(x_{26}-x_{30})$	0(3)5(4)	5(3)
4	$(x_{36}-x_{40})$	5(3)	0(4)5(3)
Time [s]		0.3462	0.1098
Accuracy [%]		75	65

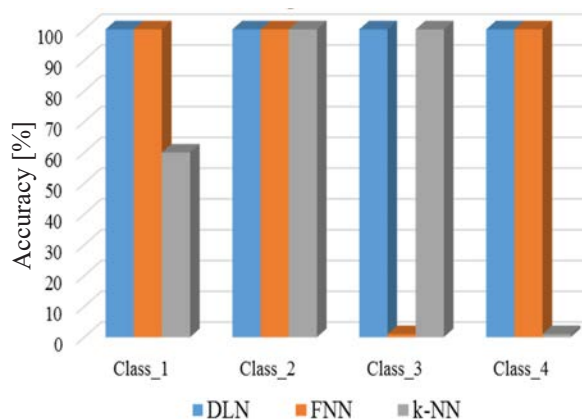


Fig. 6. Comparisons of identification accuracy results

#### 4 CONCLUSIONS

This research, based on a theoretical framework and experiment, proposes a diagnostic method for determining the wear states of cutting tools used for face milling. The experimental data are the spindle vibration signals of the milling machine in relation to wear state of cutting tools. The proposed diagnosis technique is structured based on the SAE in feature representation, a softmax classifier model, and experimental data. In particular, the vibration data related the tool wear state are used by AEs to create compact low-dimensional data that expresses the most important features of the actual tool states. Softmax is then combined to train the model to recognize tool states. The experimental results demonstrate that this proposed technique is highly effective in accurately identifying patterns of tool wear states in the face milling process. Based on data of time series, the authors believe that this proposed technique can be used to diagnose other conditions of the cutting tool such as tool breakage or tool life and can be applied to other diagnostic fields such as the bearing fault or gear fault.

#### 5 ACKNOWLEDGEMENT

The authors would like to express our gratitude to Faculty of Mechanical Engineering, Hanoi University of Industry.

#### 6 CONFLICTS OF INTEREST

The authors declare that they have no conflict of interest.

#### 7 REFERENCES

- [1] Lauro, C.H., Brandão, L.C., Baldo, D., Reis, R., Davim, J.P. (2014), Monitoring and processing signal applied in machining processes—A review. *Measurement*, vol. 58, p. 73-86, DOI:10.1016/j.measurement.2014.08.035.
- [2] Cui, Y., Fussell, B.K., Jerard, R.B., Esterling, D. (2009). Tool wear monitoring for milling by tracking cutting force model coefficients. *Transactions of the North American Manufacturing Research Institution of SME*, vol. 37, p. 613-620.
- [3] Hoang, D.T., Nguyen, N.-T., Tran, Q.D., Nguyen, T.V. (2019). Cutting forces and surface roughness in face-milling of SKD61 hard steel. *Strojniški vestnik - Journal of Mechanical Engineering*, vol. 65, no. 6, p. 375-385, DOI:10.5545/sv-jme.2019.6057.
- [4] Chi, Y., Dai, W., Lu, Z., Wang, M., Zhao, Y. (2018), Real-time estimation for cutting tool wear based on modal analysis of monitored signals. *Applied Sciences*, vol. 8, no. 5, art ID. 708, DOI:10.3390/app8050708.
- [5] Čerče, L., Pušavec, F., Kopač, J. (2015) A new approach to spatial tool wear analysis and monitoring. *Strojniški vestnik - Journal of Mechanical Engineering*, vol. 61, no. 9, p. 489-497, DOI:10.5545/sv-jme.2015.2512.
- [6] Lu, H., Chang, C., Hwang, N., Chung, C. (2009), Grey relational analysis coupled with principal component analysis for optimization design of the cutting parameters in high-speed end milling. *Journal of Materials Processing Technology*, vol. 209, no. 8, p. 3808-3817, DOI:10.1016/j.jmatprotec.2008.08.030.
- [7] Dimla, E.D. Snr. (2000) Sensor signals for tool-wear monitoring in metal cutting operations—a review of methods. *International Journal of Machine Tools and Manufacture*, vol. 40, no. 8, p. 1073-1098, DOI:10.1016/S0890-6955(99)00122-4.
- [8] Penedo, F., Haber, R.E., Gajate, A., Toro, R.M. (2012), Hybrid incremental modeling based on least squares and fuzzy K-NN for monitoring tool wear in turning processes. *IEEE Transactions on Industrial Informatics*, vol. 8, no. 4, p. 811-818, DOI:10.1109/TII.2012.2205699.
- [9] Brezak, D., Majetic, D., Udiljak, T., & Kasac, J. (2012) Tool wear estimation using an analytic fuzzy classifier and support vector machines. *Journal of Intelligent Manufacturing*, vol. 23, no. 3, p. 797-809, DOI:10.1007/s10845-010-0436-x.
- [10] Nguyen, V.H., Cheng, J.S., Thai, V.T. (2017). An integrated generalized discriminant analysis method and chemical reaction support vector machine model (GDA-CRSVM) for bearing fault diagnosis. *Advances in Production Engineering & Management*, vol. 12, no. 4, p. 321-336, DOI:10.14743/apem2017.4.261.
- [11] Palanisamy, P., Rajendran, I., Shanmugasundaram, S. (2008). Prediction of tool wear using regression and ANN models in end-milling operation. *The International Journal of Advanced Manufacturing Technology*, vol. 37, p. 29-41, DOI:10.1007/s00170-007-0948-5.
- [12] Li, X., Lim, B., Zhou, J., Huang, S., Phua, S., Shaw, K., Er. M.J. (2009). Fuzzy neural network modelling for tool wear estimation in dry milling operation. *Annual Conference of the Prognostics and Health Management Society*, p. 1-11.

- [13] Bajić, D., Celent, L., Jozić, S. (2012). Modeling of the influence of cutting parameters on the surface roughness, tool wear and the cutting force in face milling in off-line process control. *Strojniški vestnik - Journal of Mechanical Engineering*, vol. 58, no. 11, p. 673-682, DOI:10.5545/sv-jme.2012.456.
- [14] Zimroz, R., Bartelmus, W., Barszcz, T., Urbanek, J. (2014). Diagnostics of bearings in presence of strong operating conditions non-stationarity—A procedure of load-dependent features processing with application to wind turbine bearings. *Mechanical systems and signal processing*, vol. 46, no. 1, p. 16-27, DOI:10.1016/j.ymssp.2013.09.010.
- [15] Jia, F., Lei, Y., Lin, J., Zhou, X., Lu, N. (2016). Deep neural networks: A promising tool for fault characteristic mining and intelligent diagnosis of rotating machinery with massive data. *Mechanical Systems and Signal Processing*, vol. 72-73, p. 303-315, DOI:10.1016/j.ymssp.2015.10.025.
- [16] Bishop, C.M. (2006). *Pattern Recognition and Machine Learning*. Springer, Cambridge.
- [17] Fritscher, K., Raudaschl, P., Zaffino, P., Spadea, M.F., Sharp, G.C., Schubert, R. (2016). Deep neural networks for fast segmentation of 3D medical images. *Medical Image Computing and Computer-Assisted Intervention; 19th International Conference*, p. 158-165, DOI:10.1007/978-3-319-46723-8\_19.
- [18] Gao, S., Zhang, Y., Jia, K., Lu, J., Zhang, Y. (2015). Single sample face recognition via learning deep supervised autoencoders. *IEEE Transactions on Information Forensics and Security*, vol. 10, no. 10, p. 2108-2118, DOI:10.1109/TIFS.2015.2446438.
- [19] Nguyen, V.H., Cheng, J.S., Yu, Y., Thai, V.T. (2019). An architecture of deep learning network based on ensemble empirical mode decomposition in precise identification of bearing vibration signal. *Journal of Mechanical Science and Technology*, vol. 33, no. 1, p. 41-50, DOI:10.1007/s12206-018-1205-6.
- [20] Chong, E., Han, C., Park, F.C. (2017). Deep learning networks for stock market analysis and prediction: Methodology, data representations, and case studies. *Expert Systems with Applications*, vol. 83, p. 187-205, DOI:10.1016/j.eswa.2017.04.030.
- [21] Lu, C., Wang, Z., Zhou, B. (2017). Intelligent fault diagnosis of rolling bearing using hierarchical convolutional network based health state classification. *Advanced Engineering Informatics*, vol. 32, p. 139-151, DOI:10.1016/j.aei.2017.02.005.
- [22] Långkvist, M., Karlsson, L., Loutfi, A. (2014). A review of unsupervised feature learning and deep learning for time-series modeling. *Pattern Recognition Letters*, vol. 42, p. 11-24, DOI:10.1016/j.patrec.2014.01.008.
- [23] Bengio, Y. (2009). Learning deep architectures for AI. *Foundations and Trends® in Machine Learning*, vol. 2, no. 1, p. 1-127, DOI:10.1561/2200000006.
- [24] Shi, C., Panoutsos, G., Luo, B., Liu, H., Li, B., Lin, X. (2019). Using multiple-feature-spaces-based deep learning for tool condition monitoring in ultraprecision manufacturing. *IEEE Transactions on Industrial Electronics*, vol. 66, no. 5, p. 3794-3803, DOI:10.1109/TIE.2018.2856193.
- [25] Agogino, A., Goebel, K. (2007). Milling data set. NASA Ames Prognostics Data Repository, NASA Ames, Moffett Field, <http://ti.arc.nasa.gov/project/prognostic-data-repository>.

# Internal Friction of Ball Bearings at Very Low Temperatures

Jakub Sikorski – Witold Pawlowski\*

Lodz University of Technology, Institute of Machine Tools and Production Engineering, Poland

*Results of the study on the internal friction of steel ball bearings made of X65Cr14 alloy and ceramic bearings made of zirconium oxide operating at temperatures lowered by liquid nitrogen down to  $-195\text{ }^{\circ}\text{C}$  are presented in this paper. Standard grease added by the manufacturer, while graphite and molybdenum disulphide powder were used for lubrication of the bearings during the measurements. Tests were also carried out to examine the performance of the bearings operating without lubrication. The power of bearing internal friction versus temperature was measured. The lowest bearing internal friction was observed for molybdenum disulphide, whose effective lubricating performance was verified for both types of ball bearings. Graphite powder was almost equally effective with the advantage of being suitable for use in machines that come into contact with food.*

**Keywords:** rolling bearings, rolling resistance, lubrication, low temperatures

## Highlights

- At very low temperatures ( $-195\text{ }^{\circ}\text{C}$ ) the type of lubrication used in the bearing is of much greater importance than the material of which the bearing is made.
- Steel bearings can be used in machines operating at very low temperatures provided that viscous lubricants are replaced with dry lubricants.
- The lowest bearing internal friction was observed for molybdenum disulphide, whose effective lubricating performance was verified for both steel and ceramic types of ball bearings.
- The performance of the bearings at low temperatures was supported by measuring the power of the internal friction as well as with the microscopic analyses of the surface structures of cooperating elements of the bearings.

## 0 INTRODUCTION

One of the most common assemblies in any machine is the bearing. It is also one of the most important ones as the failure-free operation of any equipment depends on its faultless functioning. The more complex the machine is, the more bearings it requires, which is why ensuring optimal operating conditions for each bearing in the machine is paramount. Several key factors affect the service life of the bearing. The most important one is the maintenance of proper lubrication.

Many studies on lubrication and lowering the coefficient of friction between cooperating machine parts have indicated lubricants expected to ensure reliable performance of bearings over a wide range of temperatures. Naturally, the first lubricants to be analysed were those added by the manufacturer. However, these substances fail to retain their properties within a broad spectrum of temperatures, especially when operating at low and very low temperatures. The increasing viscosity of the grease and subsequent formation of paraffinic microcrystals leads to a complete solidification of the lubricant and entrapment of the remaining liquid fraction in the crystal lattice of paraffin and wax [1] and [2]. The thin layer of lubricant in bearings undergoes elastohydrodynamic lubrication (EHL) for which the roughness of cooperation

bearing surfaces is a significant factor [3]. The surface roughness, temperature, and lubrication methods as well as clearance size are also mutually dependent factors regarding friction and wear in composite plain bearings [4].

Solids exhibit greater stability over a wide temperature range. For this reason, the following study concentrated on the lubricating capacity of such substances, which reduce the coefficient of friction that are based on pure powder free of liquid fractions. Graphite and molybdenum disulphide are most frequently used for this purpose, while tungsten sulphide, graphite fluoride, tetrafluoroethylene, and certain polymers are resorted to less often [5] and [6].

The use of carbon in the form of graphite powder to lubricate cooperating machine parts has long been known and has been discussed extensively in the literature. However, the analyses of the behaviour of graphite as a lubricant were focused on high operating temperatures, with temperatures as high as  $120\text{ }^{\circ}\text{C}$  considered in some of the studies as low. Thermal conditions reported in the previous studies have ranged from ambient temperatures up to  $550\text{ }^{\circ}\text{C}$  [1], [5], [7] and [8].

Molybdenum disulphide is another well-known lubricant. Again, investigations of its lubricating performance when applied as a powder or a surface

coating of cooperating parts have been carried out at temperatures varying from 20 °C to 800 °C [9] to [13].

The behaviour of molybdenum disulphide and molybdenum disulphide and graphite composites bonded with polymer resins is also described. The effectiveness of these lubricating composites was tested to a temperature close to -200 °C [14].

This article reports the analysis of the performance of steel and ceramic bearings operating under very low temperature conditions. The tests were carried out on ball bearings at temperatures lowered with liquid nitrogen to -195 °C. Bearings lubricated with standard lubricant added by the manufacturer, graphite powder, and molybdenum disulphide powder were investigated. Attempts were also made to test the steel and ceramic bearings operating with no lubrication.

Depending on the manufacturer, operation limit temperatures in the range of -30 °C to -80 °C are recommended for commercially available rolling bearings and lubricants [15]. The following study is to enhance the current understanding of how bearings and lubricants behave at very low temperatures, which could be useful in the design of new generation robots for exploration of space and nearby planets in the solar system.

## 1 DESCRIPTION OF THE EXPERIMENT SETUP

The most important element of the test bench shown in Fig. 1 is a low-temperature chamber, inside which the ball bearing (1) is mounted on the aluminium frame (2) with an aluminium clamping ring (3) fastened to the frame with two bolts (4). Furthermore, a copper tube is included in the frame (5), inside of which a

resistance detector of temperature (6) has been placed. The purpose of the tube is to improve heat transfer to the detector glued inside one of the tube pieces with silver-based thermal paste.

The drive system of the bearing is comprised of a high-speed DC motor (7), a clutch (8) which transmits torque to the drive shaft (9) at the end of which the bearing is installed. The point of using a DC motor was to significantly simplify the procedure for measuring the power of the bearing internal friction. Two neodymium magnets (10) are embedded in the shaft openings, cooperating with a Hall effect sensor (11) used for precise measurement of the rotational speed of the bearing. The entire mechanical system is encased in a two-piece thermal cover (12) made of extruded polystyrene foam and fitted with a sight glass (13) at its front to enable observation of the bearing during the test. A hole at the top of the cover allows liquid nitrogen to be supplied to cool the bearing.

The measurement setup illustrated in Fig. 2 consists of a low-temperature chamber (1) into which liquid nitrogen from a dewar (2) is supplied through a PTFE tube capable of withstanding low temperatures. The electric motor is powered with a laboratory power supply (3), and its rotational speed is measured by a frequency meter (4) receiving impulses from the Hall effect detector. Other elements include universal meters to measure the temperature detector resistance (5) and to control voltage drops across the power cords (6). The last device connected to the laboratory power supply is an oscilloscope (7) that additionally monitors potential voltage surges on the electric motor. The data from the power supply, frequency meter, and resistance meter are recorded on a laptop computer (8).

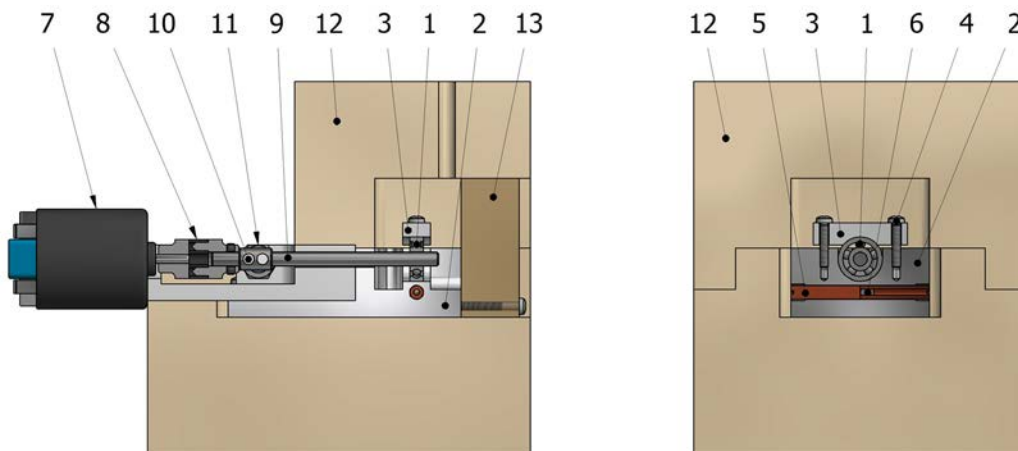


Fig. 1. Front and side section view of the low-temperature chamber

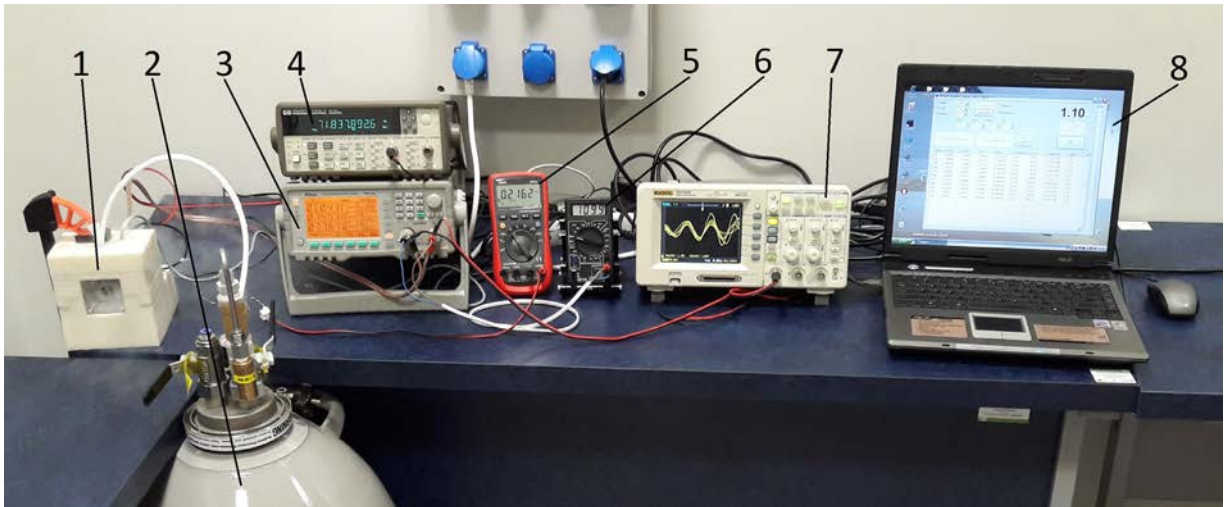


Fig. 2. Low-temperature chamber with measuring equipment

## 2 RESEARCH METHODOLOGY

Friction is a prevalent physical phenomenon. It occurs whenever an object is in motion and strives to counteract it. In machines, two main types of friction can be identified: kinetic or sliding friction in bearings and sliding joints, and rolling friction in all types of rolling bearings. In the case of rolling objects, surface deformation is always observed; therefore, the harder the material of which the bearing is made, the smaller the contact surface of the bearing elements, which may consequently result in less friction.

Friction between the balls of the bearing and its inner and outer races generates friction torque that counteracts the rotation of the bearing. The torque, combined with information on the rotational speed of the shaft on which the bearing is mounted, enables calculating the power required to drive the rotating bearing. Based on the above information, it was concluded that the electric power supplied to the electric motor that puts the bearing into rotational motion reflects the bearing internal friction.

The first step in getting ready for determining the bearing internal friction was to determine the power of resistance to movement of the drive system itself. For this purpose, the power consumption of the drive motor and power supply cords was analysed. The laboratory power supply used in the study allows the user to control the voltage and current supplied to the motor with a computer, which renders the procedure of supplying power to the motor entirely reproducible. The laboratory power supply also allows the user to monitor voltage drops on the power cords with a

second pair of cords. A schematic diagram in Fig. 3 shows the correct connection of the entire system. OFC 4N oxygen-free copper cables with a cross-section area of 4 mm<sup>2</sup> were used to further limit influence of resistance from the power cords. The objective was to minimize cable heat-up during operation and maintain consistent resistance during subsequent measurements. The values of the power of the electric motor and cords thus obtained were subtracted from the total power of the entire setup (with bearing) to determine the power lost during the operation of the bearing.

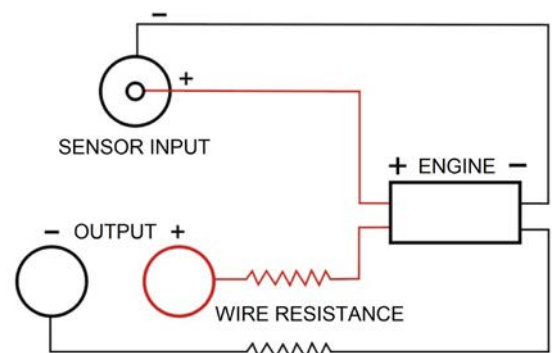
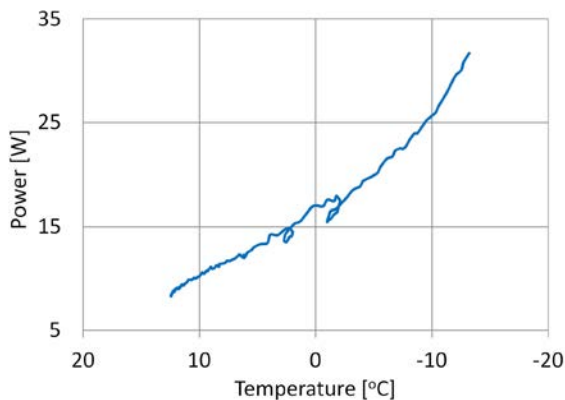


Fig. 3. Schematic diagram of the laboratory power supply connection

Before the measurements, each bearing was submitted to the following procedure to normalize the testing parameters. For all the measurements, 5 mm × 16 mm × 5 mm type 625 ball bearings without seals were used. After being installed on the drive shaft, the

bearing was placed in the frame and secured with the clamping ring bolts tightened in the same reproducible manner for each test.

Next, the drive system of the bearing was run for about an hour so that, at a speed of about 30,000 rpm, the bearing would complete 2,000,000 revolutions, which was recorded by a frequency meter. The purpose was to remove excess lubricant from the bearing and to obtain consistent and reproducible measurement results. The preliminary 2,000,000 revolutions proved to be particularly meaningful for bearings lubricated with viscous grease, as is evident in the graph below (Fig. 4) illustrating the attempt to run measurements on a newly installed bearing. Apparently, an excess of the lubricant caused the bearing to seize up at a temperature of  $-14^{\circ}\text{C}$  due to the lubricant thickening. The lubricant increasing its viscosity also results in the increase of the power required to drive the bearing with higher movement resistance which in turn causes temporary warming of the bearing.



**Fig. 4.** Power of the steel bearing internal friction immediately upon mounting

All experiments (40 per each bearing type) were performed according to the following procedure:

- running the bearing at ambient temperature for 10 min (60,000 rotations or 130,000 rotations respectively) in order to stabilize the initial conditions of the measurement,
- closing the low-temperature chamber and the moisture removal by the nitrogen insufflation,
- the measurement procedure of gradual cooling the bearing to  $-195^{\circ}\text{C}$  lasting 8 min to 22 min,
- opening the chamber and gradual warming the still rotating bearing (60 min).

During each cycle of measurements of the bearing internal friction, the following data were collected: the values of voltage, electric current, and power supplied to the motor recorded by the laboratory power

supply, the drive shaft rotational speed by the Hall effect sensor connected to the frequency meter, and the resistance of the temperature sensor read by the universal meter. All the above measuring instruments were connected to the computer in which, with the aid of proprietary software, the data was logged at a speed of about 80 rows per minute and, in the case of temperature, converted from electrical resistance.

Based on the results of the preliminary measurements, it was concluded that to ensure the most consistent results, the bearings should be cooled down at the slowest rate possible. For this reason, the results of measurement cycles of less than 8 minutes were disregarded. In the next section, examples of charts that provide information about the power of the analysed steel and ceramic bearings' internal friction are presented. The charts were produced based on data sets with 600 to 1,700 measurement data rows.

### 3 ANALYSIS OF THE RESULTS

The experiments comprised 80 measurement cycles performed for two types of bearings. Based on the analysis of the test results, the maximum dispersion of the measurement values for each bearing type was determined to be max. 7 %. The graphs below present the most representative measurements of the power of bearing internal friction versus temperature. The first chart (Fig. 5) illustrates the results of measurements of the power of the internal friction of a steel bearing made of X65Cr14 alloy mounted on a drive shaft rotating at a speed of 6,000 rpm. The choice of stainless steel bearings (X65Cr14) was caused by the resistance to possible corrosion. That corrosion could be initiated by moisture condensing during the heating phase of the test rig when the low-temperature chamber is open. The effect of the corrosion could have introduced additional errors during the power measurements. During the preliminary tests, the bearing operated with the lubricant added by the manufacturer. The grease was then removed, and attempts were made to test the performance of the bearing completely clean of lubrication. Unfortunately, the steel bearings run without any lubricant would fail after only a few hours of testing. The last one to be tested was a bearing in which the standard grease was replaced with molybdenum disulphide powder.

With standard grease, a gradual increase in the power of the bearing internal friction is clearly evident until the thickening lubricant was almost completely removed from the race where the bearing balls rolled. For lubricant-free and molybdenum disulphide measurements, the graphs show almost linear trends

over the entire temperature range. This is explained by the powder lubricant being non-sensitive to the decrease in temperature, whereas a slight increase in the power consumed by the bearing can most probably be attributed to the shrinkage of the aluminium housing, which led to additional clamping of the outer bearing race.

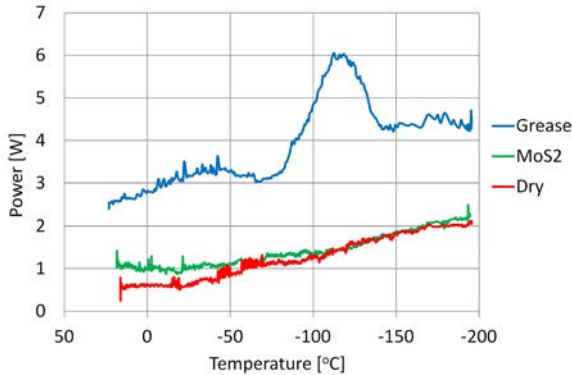


Fig. 5. Power of the steel bearing internal friction, 6,000 rpm

The graph (Fig. 6) shows the internal friction of a steel bearing mounted on a drive shaft rotating at a speed of 13,000 rpm. The same lubrication parameters as for the speed of 6,000 rpm were used for the measurements. The higher rotational speed further exposed inadequate properties of the viscous grease and confirmed the low internal friction values produced by the bearing lubricated with molybdenum disulphide. Furthermore, it has been successfully demonstrated that for both rotational speeds the steel bearing is capable of performing its function even at  $-195\text{ }^{\circ}\text{C}$ , although the issue of selecting the most appropriate lubricant remains of utmost importance.

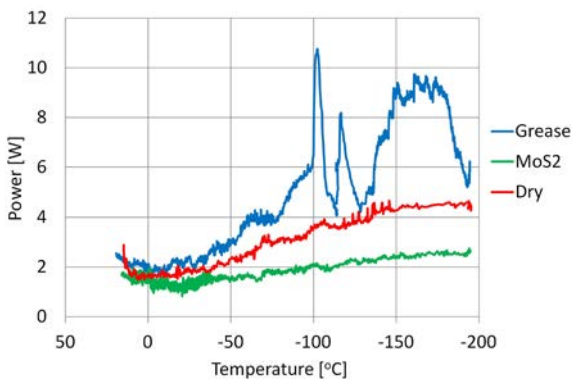


Fig. 6. Power of the steel bearing internal friction, 13,000 rpm

The graph in Fig. 7 presents the internal friction of a zirconium oxide bearing mounted on a shaft rotating at a speed of 6,000 rpm. The full ceramic

bearing (both races and balls) is commercially supplied with no lubricant added and has been designed to operate as such. The subsequent tests were carried out with graphite and molybdenum disulphide powder lubrication. As the chart clearly shows for all the variants, the bearing internal friction was low and increased linearly starting at  $-50\text{ }^{\circ}\text{C}$  as the temperature recorded inside the low-temperature chamber was decreasing. Again, the increase in the power consumed by the bearing was probably caused by the shrinkage of the aluminium housing, which resulted in additional clamping of the outer race of the bearing. Slightly higher values of the power of internal friction observed for the ceramic bearing could have been caused by a smaller predetermined internal clearance than for the steel bearing.

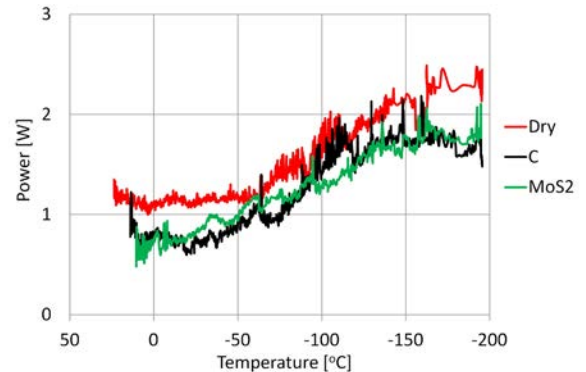
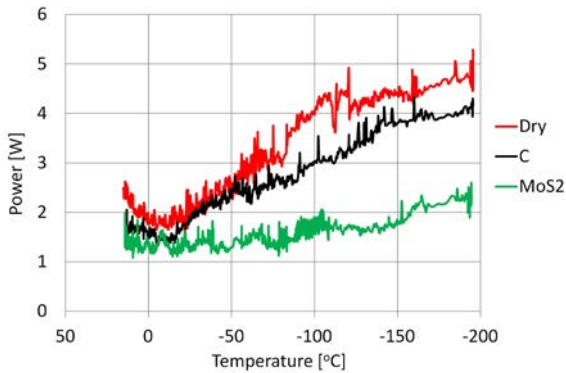


Fig. 7. Power of the ceramic bearing internal friction, 6,000 rpm

The graph (Fig. 8) shows the internal friction of a ceramic bearing mounted on a shaft rotating at a speed of 13,000 rpm. As is evident, power trends for the non-lubricated and graphite powder lubricated bearings are similar to those observed for 6,000 rpm. The values of the power of the bearing internal friction are only proportionately higher relative to the higher rotational speed of the drive shaft. When lubricated with molybdenum disulphide powder, the bearing resistance remained at virtually the same level as in the previous chart. This further corroborates the claim that the increase in internal friction was caused only by the change in the bearing dimensions resulting from a temperature decrease to  $-195\text{ }^{\circ}\text{C}$ . As in the previous charts, also here, for all the cases, the bearing internal friction increased linearly with decreasing temperature, starting at about  $-20\text{ }^{\circ}\text{C}$ .



**Fig. 8.** Power of the ceramic bearing internal friction, 13,000 rpm

#### 4 ANALYSIS OF THE CONDITION OF THE BEARINGS

Having completed the measurements, an attempt was made to inspect the mechanical condition of the bearings that had been tested at the bench. For this purpose, microscope images of new bearing balls and balls of the bearings used in the tests at the test bench were captured.

Fig. 9 shows an image of a ball of a new steel bearing. The visible irregularities are due to the machining of the ball by the bearing manufacturer. A large number of surface scratches and pits are evident. For this reason, a lubricant is required for proper operation of steel bearings to facilitate interaction between the ball and the bearing races. The dark spots in the image are a residue of the grease added by the manufacturer.

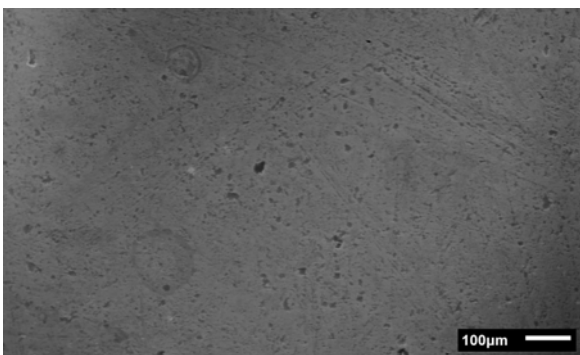


**Fig. 9.** Surface of the ball of a new steel bearing

The image (Fig. 10) is a photograph of a ball of a steel bearing run in the most difficult conditions, i.e., with no lubrication. Areas are visible where the material has been torn off the surface of the ball due to friction between the bearing assembly parts, significantly impairing the smoothness of the interacting surfaces. A high rate of growth in the

number of such defects results in a global increase in the bearing internal friction and thus in elevated temperatures of the rolling parts, which further accelerates the process of the bearing degradation. This is why it is so crucial that lubricant is used in steel bearings as it reduces friction and improves heat dissipation from the areas of the bearing under the greatest loads. Only a few hours of operation resulted in the bearing failure due to deterioration of the ball and race surfaces.

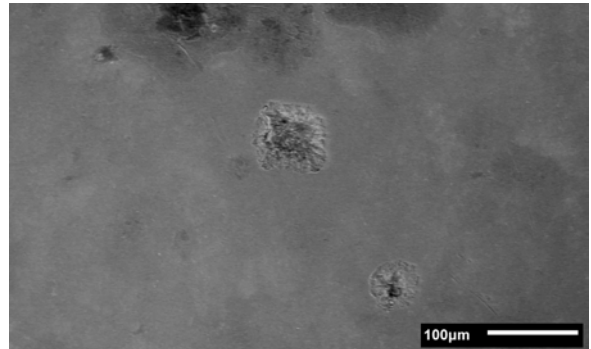


**Fig. 10.** Surface of the ball of a steel bearing after the tests

In Fig. 11, an image of a ball of a new ceramic bearing is shown. Clearly, the surface is much smoother than in the case of the steel bearing. The only few irregularities noticeable come from the machining of the ball by the bearing manufacturer. To reveal any further surface irregularities, it was necessary to take a photograph with the magnification 20 times higher than required for the steel bearing. The high degree of smoothness and the high level of the material hardness render ceramic bearings capable of operating without additional lubrication.

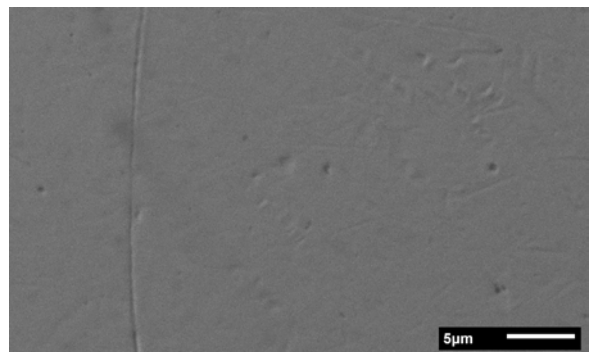


**Fig. 11.** Surface of the ball of a new ceramic bearing

The image (Fig. 12) shows a ceramic bearing ball after the measurements of the bearing internal friction. During all cycles of measurement, the ceramic bearing completed 7,000,000 revolutions at the bench,

operating with lubrication by molybdenum disulphide powder without grease. The surface of the ball shows minor signs of wear, but it is essential to remember that the size of the scratches and damaged areas is minute. Molybdenum disulphide is also visible in the photograph, filling all minor damage areas and improving the overall smoothness of the ball surface. The molybdenum disulphide powder may have been removed from larger scratches during the ball cleaning process prior to microscopic imaging.

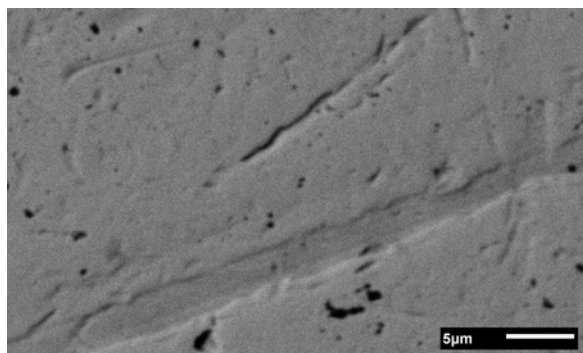


Fig. 12. Surface of the ball of a ceramic bearing after the test

During all performed tests, constantly growing power consumption of the bearing due to its wear was not observed. Both measurements of the power of bearing initial friction as well as microscopic images of the bearing balls subjected to the examinations indicate that the accelerated structural wear of tested bearing elements at low temperatures does not occur significantly.

## 5 CONCLUSIONS

Based on the performed measurements, it has been found that the type of lubrication used in the bearing is of much greater importance than the material of which the bearing is made. Contrary to the general opinion, steel bearings can be used in machines operating at very low temperatures provided that viscous lubricants are replaced with dry lubricants. The virtually linear graphs indicate that operation of steel and ceramic bearings should be possible and reliable even at temperatures lower than  $-195\text{ }^{\circ}\text{C}$ .

The lowest bearing internal friction was observed for molybdenum disulphide, whose effective lubricating performance was verified for both types of ball bearings. Furthermore, its properties remained unaffected throughout all the measurement cycles performed on bearings lubricated in this manner. Graphite powder was almost equally effective with the

added advantage of being suitable for use in machines that come into contact with food.

Due to the design of the test bench, the thermal expansion of individual materials in contact with the studied bearings was taken into account in the tests. The increase in power with decreasing temperature is certainly due to the shrinkage of the aluminium frame; however, the increase in power due to the shrinkage of the bearing itself cannot be ruled out on that stage of research. These issues, as well as the interaction of the bearings with materials such as aluminium and titanium alloys used as a construction material for shafts and hub assemblies, will be the focus of future research.

## 6 REFERENCES

- [1] Mortier, R.M., Orszulik, S.T. (eds.) (1992). *Chemistry and Technology of Lubricants*. Springer Science + Business Media, New York.
- [2] Wie, B. (2015). Recent advances on mitigating wax problem using polymeric wax crystal modifier. *Journal of Petroleum Exploration and Production Technology*, vol. 5, p. 391-401, DOI:10.1007/s13202-014-0146-6.
- [3] Yang, X., Li, Y., Liu, G., Wang, J. (2019). Effect of surface roughness on elastohydrodynamic lubrication performance of cylindrical roller bearing. *Technical Gazette - Tehnički vjesnik*, vol. 26, no. 3, p. 710-721, DOI:10.17559/TV-20190104091451.
- [4] Miler, D., Škec, S., Katana, B., Žeželj, D. (2019). An experimental study of composite plain bearings: The influence of clearance on friction coefficient and temperature. *Strojniški vestnik - Journal of Mechanical Engineering*, vol. 65, no. 10, p. 547-556, DOI:10.5545/sv-jme.2019.6108.
- [5] Sliney, H.E. (1991). *Solid Lubricants*. NASA Technical Memorandum, NASA, Cleveland.
- [6] Miyoshi, K. (1999). Considerations in vacuum tribology (adhesion, friction, wear, and solid lubrication in vacuum). *Tribology International*, vol. 32, no. 11, p. 605-616, DOI:10.1016/S0301-679X(99)00093-6.
- [7] Peterson, M.B., Johnson, R.L. (1956). Friction studies of graphite and mixtures of graphite with several metallic oxides and salts at temperatures to  $1000\text{ }^{\circ}\text{F}$ . *NASA Technical Notes*, NASA, Cleveland.
- [8] Savage, R.H. (1948). Graphite Lubrication. *Journal of Applied Physics*, vol. 19, no. 1, DOI:10.1063/1.1697867.
- [9] Johnson, V.R., Vaughn, G.W. (1956). Investigation of the mechanism of  $\text{MoS}_2$  lubrication in vacuum. *Journal of Applied Physics*, vol. 27, no. 10, p. 1173-1179, DOI:10.1063/1.1722224.
- [10] Khare, H.S., Burris, D.L. (2013). The effects of environmental water and oxygen on the temperature-dependent friction of sputtered molybdenum disulfide. *Tribology Letters*, vol. 52, p. 485-493, DOI:10.1007/s11249-013-0233-8.
- [11] Kubart, T., Polcar, T., Kopecký, L., Novák, R., Nováková, D. (2005). Temperature dependence of tribological properties of  $\text{MoS}_2$  and  $\text{MoSe}_2$  coatings. *Surface and Coatings*

- Technology*, vol. 193, no. 1-3, p. 230-233, **DOI:10.1016/j.surfcoat.2004.08.146**.
- [12] Muratore, C., Voevodin, A.A. (2006). Molybdenum disulfide as a lubricant and catalyst in adaptive nanocomposite coatings. *Surface and Coatings Technology*, vol. 201, no. 7, p. 4125-4130, **DOI:10.1016/j.surfcoat.2006.08.014**.
- [13] Khare, H.S., Burris, D.L. (2014). Surface and subsurface contributions of oxidation and moisture to room temperature friction of molybdenum disulfide. *Tribology Letters*, vol. 53, p. 329-336, **DOI:10.1007/s11249-013-0273-0**.
- [14] Yuhno, T.P., Vvedensky, Y.V., Sentyurikhina, L.N. (2001). Low temperature investigations on frictional behavior and wear resistance of solid lubricant coatings. *Tribology International*, vol. 34, no. 4, p. 293-298, **DOI:10.1016/S0301-679X(01)00013-5**.
- [15] Diemand, D. (1990). Lubricants at low temperatures. *Cold Regions Technical Digest*, no. 90, USA Cold Regions Research and Engineering Laboratory, Hanover.

# Study on the Influence of Metallic Powder in Near-Dry Electric Discharge Machining

Sanjay Sundriyal<sup>1</sup> – Vipin<sup>1</sup> – Ravinderjit Singh Walia<sup>2,\*</sup>

<sup>1</sup>Delhi Technological University, India

<sup>2</sup>Punjab Engineering College, India

*Near-dry electrical discharge machining (ND-EDM) is an eco-friendly process. In this study, an approach has been made to make the machining process more efficient than ND-EDM with the addition of metallic powder with the dielectric medium to machine EN-31 die steel. Powder-mixed near-dry EDM (PMND-EDM) has several advantages over the ND-EDM or conventional electrical discharge machining (EDM) process, such as a higher material removal rate (MRR), fine surface finish (Ra), sharp cutting edge, lesser recast layer, and lower deposition of debris. The output response variables are MRR, Ra, residual stress (RS) and micro-hardness (MH) of the machined surfaces. Further study of the workpiece was performed, and a comparative study was conducted between ND-EDM and PMND-EDM. In this proposed method of machining, the MRR, Ra, and MH increased by 17.85 %, 16.36 %, and 62.69 % while RS was reduced by 56.09 %.*

**Keywords:** material removal rate; near-dry EDM; powder mixed near-dry EDM; residual stress; surface roughness

## Highlights

- Experimental investigations have been conducted in the PMND-EDM process. The metallic powder (zinc) as an additive along with the mist of a dielectric medium was used for performance enhancements.
- In PMND-EDM, the MRR was influenced by powder concentration. The MRR increases with the increase in metallic powder concentration, and the maximum increase in MRR was 17.85 %, as compared to ND-EDM.
- The surface finish was improved by 16.36 % in PMND-EDM as the sparking is uniformly distributed among the powder particles, which gives even and uniform machined surfaces.
- There was a decrease in residual stress by 56.09 % over the machined surfaces in PMND-EDM as compared to ND-EDM process.
- The maximum increase in MH was 62.69 % over the machined surface in PMND-EDM as compared to ND-EDM.

## 0 INTRODUCTION

The necessity of machines using the least harmful cutting fluids has prompted many researchers to investigate the use of minimum quantity lubrication (MQL) in near-dry machining (NDM). In NDM, machining is done with the supply of minute quantities of lubricant or mist at the work surface. It was developed as an alternative technique to supply the internal high-pressure coolant, reducing the use of metal-working fluids (MWFs), which eventually also led to a reduction in the cost of MWFs. In NDM, the cooling medium is a combination of air and oil in the form of an aerosol, or minute droplets of mist. Mist is the gaseous suspension of solid into air (or liquid) particles. The process feasibility of near-dry electrical discharge machining (EDM) was explored in 1981, and further investigations were performed on dielectric mixtures of mist with gases such as argon and nitrogen [1]. In powder-mixed EDM (PM-EDM), the effect on the breakdown voltage of kerosene by the addition of graphite powder was studied [2]. It has been noted that some powders, such as graphite and silicon when mixed with dielectric, the distribution of spark at the discharge gap led to the creation of

very fine glossy surfaces [3]. The MRR increases and tool wear rate (TWR) decreases with the proper addition of metallic powders to the dielectric fluid. An approach was made to achieve optimal process parameters setting in PM-EDM, and the study revealed that process parameters at optimum levels in PM-EDM gave higher MRR and surface finish [4]. The effect of different powder concentration of graphite powder on responses such as Ra, TWR and MRR on H-11 die steel was studied, revealing that the addition of graphite powder at a concentration of 6 g/l enhances the MRR and surface finish while tool wear rate is decreased [5]. Research was conducted with different dielectrics on environmental and hazard and operability (HAZOP) analysis in PM-EDM, concluding that HAZOP analysis successfully reduced the wastage of dielectric, and minimized the machining cost and environmental hazards as compared to traditional EDM machining methods [6]. The thermal phenomenon in powder-mixed near-dry electrical discharge machining (PMND-EDM) was explained, and the tendency of variation in MRR was analysed by varying each process parameter [7] to [9]. The plasma channel characteristics in PM-EDM were analysed [10]. It was proved that the plasma channel

\*Corr. Author's Address: Punjab Engineering College, Vidya Path, Chandigarh, India, waliaravinder@yahoo.com

was much more stable in PM-EDM than the plasma formed in pure kerosene oil because the plasma generated in PM-EDM was compressed by the electric bridge of conductive powder particles in EDM oil. The machinability of titanium alloy (Ti-6Al-4V) was examined during EDM. The performance was assessed in terms of MRR, as was the rate of tool wear. The surface integrity of the machined specimen is evaluated in the purview of surface morphology and topographical features [11]. The impact of SiC powder concentration on surface topography, particle deposition, and subsurface structures in the PM-EDM of Ti-6Al-4V-ELI work material was studied, and it was observed that a high suspended particle concentration in dielectric liquid enhance the material transfer mechanism in a particulate form [12]. Flushing mode plays an important role in any EDM operation. An incorrect flushing can result in erratic cutting and poor machining conditions [13]. Significant work has also been done in the field of residual stress generated over a machined surfaced by EDM, and an attempt has been made to model these stresses so that these residual stresses are minimized [14]. It was revealed that the value of residual stresses at the sub-surface of the workpiece machined by EDM was more than the top surface due to high surface roughness over the top surface. A parametric study for residual stresses was performed in wire EDM, utilizing the Taguchi method of optimization to minimize the residual stresses in aluminium workpieces [15]. A nano-indentation technique and Raman spectroscopy were adopted to measure the residual stress in AISI H13 tool steel machined by EDM process [16]. The optimization of the residual stress was done using an X-ray  $\cos \alpha$  method in a vibration-assisted hybrid EDM process, analysing the residual stress generated over a high-carbon high-chromium D2 tool steel workpiece [17]. Several studies have been done regarding enhancing the micro-hardness (MH) value and surface roughness of the machined components by powder-additive EDM methodology. Efforts have been made to identify favourable conditions to enhance the surface MH of EN-31 tool steel using Cu-W tool manufactured by powder metallurgy in the electrical discharge alloying (EDA) process. The Taguchi method was followed to obtain a combination of process variables for achieving the best MH. The presence of hard tungsten carbide ( $W_2C$ ) and cementite ( $Fe_3C$ ) on the machined surface was related to the observed substantial increase in MH (approx. 150 %) [18]. An experimental work was carried out for the surface modification of Ti6Al4V alloy using TiC/Cu powder metallurgy electrode. Taguchi's  $L_{18}$

mixed orthogonal array and analysis of variance were performed to evaluate the influence of parameters on surface roughness and MH. The carbides generated on the machined surface, increased the hardness as high as 912 HV without much sacrifice of the roughness of the machined surface [19]. The surfaces of the die steel materials were modified by the addition of tungsten powder in a dielectric medium in EDM process [20]. This addition caused the deposition of carbon in the plasma, which improved the surface morphology and increased MH by more than 100 %. The MH of cryogenically treated aluminium alloy was improved by 94.85 % in PM-EDM [21]. A Taguchi  $L_9$  orthogonal array was utilized to increase the MH of the workpiece in PMND-EDM and resulted in an increase of MH upto 506.63 HV [22].

The use of minimum quantity lubrication system plays an important role regarding the accuracy obtained in machined products and also prevents environmental pollution and hazard to the workers. The use of optimum metal-working fluids leads to economic benefits and environmentally friendly machining methods. Although research related to PMND-EDM has been done previously, it was limited to the study of the MH of the machined component. This study aims to further investigate PMND-EDM in a detailed manner. After an extensive literature review, an attempt has been made to study PMND-EDM related to MRR, Ra, residual stress (RS) and MH. In this research, a new setup was developed to study the role of three-phase dielectric with different electrode dimensions, metallic powder concentration, and flow rate. His experimental setup was developed to investigate the effects of metallic powder concentration, various electrodes, and dielectric flow rate on the machining performance on the above-mentioned factors. Finally, the comparisons on machining performances were made between ND-EDM and PMND-EDM based on the results obtained by experiments.

## 1 METHODS

### 1.1 Indigenous Developed Setup for Powder Mixed Near-Dry EDM

In modern manufacturing techniques, researchers are always developing highly productive machining methods. In comparison to conventional EDM, a recent trend in technology and innovation has brought in hybrid EDM, such as dry EDM, near-dry EDM and PMND-EDM. PMND-EDM machining gives a minimum heat-affected zone and a very low

recast layer in the machined products. As discussed, PMND-EDM has several advantages over traditional EDM process; therefore, there is a need to develop a more efficient hybrid setup for PMND-EDM (Fig. 1). It has a minimal input of resources, is relatively environmentally friendly and also gives the desired results. In this study, an indigenous setup for PMND-EDM was developed that uses metallic powder mixed with kerosene oil (LL-221) under high air pressure as a dielectric medium. This machining process has advantages in terms of MRR, surface finish, and other surface characteristics in comparison to near-dry EDM, dry EDM, and other conventional EDM methods. The dielectric in this indigenous setup is a heterogeneous mixture of three phases (solid + liquid + gas). A mixing chamber was designed and manufactured in which oil along with metallic powder and glycerol are mixed in right proportion with compressed air supplied from the compressor at a high pressure, ranging from 0.4 MPa to 0.8 MPa. The setup was designed and developed in the Precision Manufacturing Laboratory (Delhi Technological University (DTU), Delhi). The designed chamber has a separate inlet for dielectric medium and, in case the pressure inside the chamber goes beyond operational limits, a safety valve mounted on top to release the pressure of compressed air has been provided. A flow meter was integrated with the setup, which can vary the flow rate of dielectric mist within range of 1ml/min to 20 ml/min. As the flow meter is a transparent body, the flow rate of mist can be easily read from the calibration scale mounted on the flow meter. To avoid metallic powder particle settling, glycerol is added in the tank along with dielectric fluid from the inlet of the tank. The setup also includes manually operated regulators mounted on the control panel for regulating air and oil pressure (0 MPa to 0.8 MPa). The setup

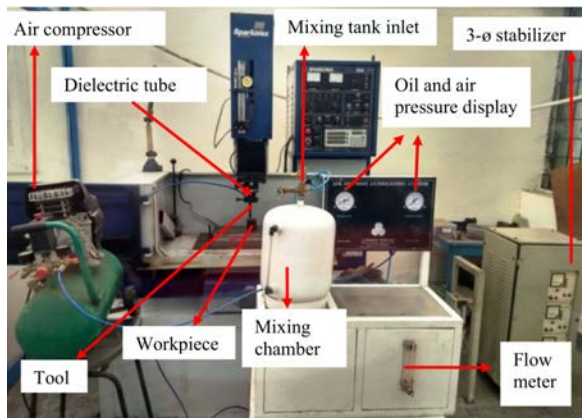


Fig. 1. Developed experimental setup for PMND-EDM

comprises a display unit for oil and air pressure, which is analogous in nature. The control panel of the EDM machine (Sparkonix Limited, Pune), consists of electrical and non-electrical parameters, such as pulse on, pulse off, gap voltage, gap current, lift, sensitivity, feed and speed. Experimental conditions for machining and is shown in Table 1.

Table 1. Experimental condition for machining

Parameters	Classification
Workpiece	EN-31 (35 mm × 15 mm × 15 mm)
Tool electrode	COPPER
Dielectric	Air + oil (LL-221) + metallic powder
Discharge current	12 A
Gap voltage	25 V
Pulse on / off	500 μs/ 75 μs
Polarity	+ve
Powder concentration	0 g/l, 2 g/l, 4 g/l
Flow meter of dielectric	0 ml/min to 20 ml/min
Air and oil pressure	0.6 MPa
Powder material	Zinc (22 μm)
Stabilizing agent	Glycerol (5 %)

Fig. 2 shows the internal design of the tool. Different dimensions of the sparking end of the tools and properties of the workpiece are given in Tables 2 and 3, respectively. Hollow tubular copper electrodes, shown in Fig. 3, were developed in the precision manufacturing lab., DTU, Delhi.

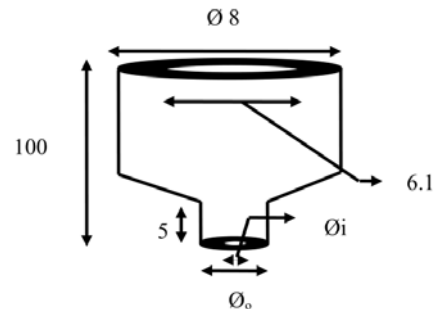


Fig. 2. Design of tool developed for PMND-EDM; all dimensions in mm

Table 2. Diameter of various tools developed for present study (sparking end)

Tool type	Inner diameter [mm]	Outer diameter [mm]
Tool 1	1	2
Tool 2	2	3
Tool 3	3	4
Tool 4	4	5

The other ends of the tools are constant in dimension with 6.1 mm inner diameter and 8 mm outer diameter. The tool setup was developed for PMND-EDM, which has a flexible tube of 6 mm outer diameter inserted at the top end of the tool.

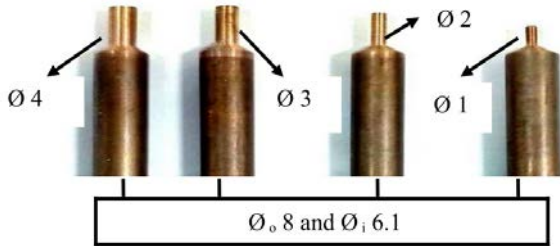


Fig. 3. Hollow copper electrode of different dimensions; all dimensions in mm

Table 3. Properties of workpiece (EN-31)

Thermal conductivity [W/(m K)]	44.5
Hardness [HRC]	63
Yield stress [MPa]	450
Tensile strength [MPa]	750
Density [kg/m <sup>3</sup> ]	7850
Melting point [°C]	1540

## 2 EXPERIMENTAL

### 2.1 Working Principle of PMND-EDM

The dielectric medium, which is a mixture of oil, metallic powder, comes out from the outlet of the mixing chamber in the form of mist accompanied by pressurized air, which was passed by the compressor into the mixing chamber. This mist was supplied to the electrode tool through a flexible tube, which eventually passes through the hollow passage of the copper tool, as shown in Fig. 4. The mist flow rate was controlled manually by the regulator provided at the control panel of the setup. As the desired experimentation condition was achieved, straight polarity power was supplied to the tool set up and the workpiece. The material removal rate is based on the heat erosion principle. The moment sparking is generated at the inter-electrode gap (IEG); gasification and fusion take place at the machining gap due to which the plasma channel is formed between the tool and the workpiece, providing a heat source to the surface of the workpiece [1]. The enormous amount of heat developed at the machining gap or spark gap melts the surface of workpiece and creates numerous craters, due to which erosion starts at the surface.

The eroded material or debris was flushed out by the high-pressurize mist. Due to the presence of metallic powder (additive), it was observed that a phenomenon of a chain like formation of powder particles, also known as the bridging effect which occurs at the machining gap [4].

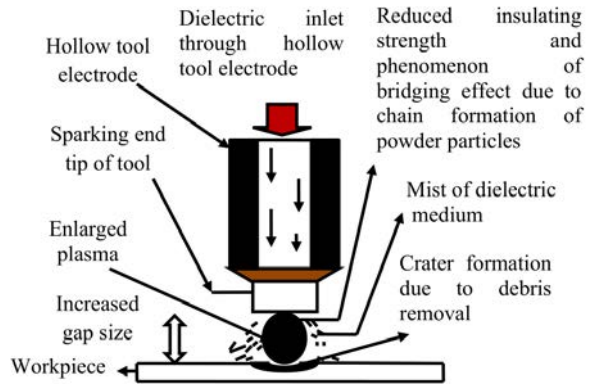


Fig. 4. Schematic diagram of electrode, plasma and workpiece interaction with each other

The chain-like formation of powder particles was due to the interlocking of grains when they come close together due to which the discharge gap between the tool and workpiece increases, energizing the spark plasma and leading to enlarged widened plasma channels with reduced electrical density. This bridging effect of grains decreases the dielectric insulating strength and gap voltage at the IEG. These favourable conditions show an increase of discharging frequency, further resulting in faster sparking at the workpiece surface due to which the material removal rate increases with improved surface quality.

## 3 EXPERIMENTAL METHOD

### 3.1 Experimental Process Parameters

The process parameters can be divided into different categories, i.e., electrical parameters, non-electrical parameters (other parameters), electrode parameters (tool), workpiece parameters and metallic powder parameters. The output response parameters include PMND-EDM process performance, such as MRR, Ra, RS and MH. The powder (zinc) used was metallic along with a stabilizing agent (glycerol) so that the powder uniformly mixes with the dielectric medium. The electrical parameters include current, pulse time, voltage, gap voltage, sensitivity, lift, feed and speed. Other parameters include mist pressure, flow rate,

etc.; the remaining factors include the type of tool electrode and workpiece.

Electrical parameters:

- *Peak current*: This is the most important electrical parameter, which determines the spark energy.
- *Discharge voltage*: This is also known as gap voltage, which is responsible for the spark gap.
- *Sensitivity*: This regulator is used to control the movement of the tool.
- *Speed*: These control the speed of z-axis lead screw or the tool.

Non-electrical parameters:

- *Oil and air pressure*: These are regulated constantly to achieve a perfect phase of both in mist.
- *Dielectric flushing pressure*: This is the pressure of the mist coming out from the dielectric tank.
- *Mist flow rate controller*: This device controls the flow rate of dielectric mist, measured in ml/min.
- *Workpiece and electrode tool*: The workpiece selected for the study is EN-31, which has good physical and chemical properties, while the electrode tool selected was copper, due to good thermal conductivity and high boiling point.
- *Dielectric oil*: Kerosene based oil (LL-221) was chosen as it has good cooling and flushing ability.
- *Metallic powder*: Different metallic powders serve as additives in the dielectric medium such as copper, zinc, silicon, graphite, aluminium powder, etc.

### 3.2 Experimental Procedure

Series of experiments were conducted in this developed hybrid setup, and responses, such as MRR, Ra, RS, and MH, were studied. The dielectric mixture was prepared by adding kerosene oil, zinc powder and glycerol. Once the mixture is filled in the dielectric tank, the pressure of mist was set at a value of 0.6 MPa by the regulator at the control panel of the hybrid setup. The flowmeter for the mist was set up at 6 ml/min. The machining time of 10 minutes was set for all the experiments. The first set of experiments was performed with mist only (i.e., without any metallic powder); the second set of experiments was performed with 2 % (2 g/l) powder concentration; the third set of experiments was done with 4 % (4 g/l) powder concentration with four different tools as given in Table 4.

A total of 36 experiments (repeatability with three times for each experiment) were conducted under experimental settings (Table 5) for obtaining the average values for output responses. The experiments

were conducted with positive polarity to obtain better results.

**Table 4.** Set for experiments

Exp. no.	Powder concentration [%]	Total experiments	Tool type
1	0	4	1, 2, 3, 4
2	2	4	1, 2, 3, 4
3	4	4	1, 2, 3, 4

Pressure 0.6 MPa; time 10 min;  $T_{on}$  500  $\mu$ s;  $T_{off}$  75  $\mu$ s; discharge current 12 A; gap voltage 25 V; tool electrode (copper); workpiece EN-31; mist flow rate 6 ml/min

**Table 5.** Dielectric medium proportion for different set of experiments

Exp. no.	Medium
1	Compressed Air + kerosene oil
2	Compressed Air + 2 gram zinc powder + kerosene oil + 5 % glycerol
3	Compressed Air + 4 gram zinc powder + kerosene oil + 5 % glycerol

The response was measured using the relations given below:

$$MRR = (W_i - W_f) / T_m,$$

where  $W_i$  is the initial weight of the workpiece before machining,  $W_f$  the final weight of the workpiece after machining,  $T_m$  the time taken for machining, and  $MRR$  in mg/min.

*Surface finish*: Ra was checked by using a benchtop ZeGage optical profilometer (model TM3000).

*Residual stress*: RS was calculated by using a Pulsetech  $\mu$ X-360 residual stress analyser.

*Micro-hardness*: MH was measured by using a Fischerscope instrument (HM2000S model, USA)

*Weight of the specimen* was measured using an electronic balance of least count 0.001gram (Asia Techno weigh India).

*Scanning electron microscope*: A Hitachi Scanning electron microscope for the study of surface morphology of machines surface.

## 4 RESULTS AND DISCUSSION

### 4.1 Influence of Machining Process on MRR

In PMND-EDM, with the addition of liquid and conductive metallic powder to compressed air, there was a reduction of the dielectric medium insulating strength between a tool and workpiece electrodes. This resulted in improved de-ionization effect and

discharging conditions. All these factors improve discharge frequency and MRR is thus increased. A solid and liquid mixture, such as mist assisted with metallic powder, changes the electric field strength of the dielectric medium and thus facilitates the discharge initiation [7]. Enlarged discharge gap results in sufficient heat dissipation, due to which more molten materials were ejected by the explosive force by the gasification of solid and liquid phases. This phenomena also restrains the excessive expansion of the discharge channel in its radius. Higher MRR was observed in metallic PMND-EDM, because IEG increases due to the cluster formation of metallic powder, which increases plasma intensity and results in more erosion. The samples of the workpiece machined by PMND-EDM are shown in Fig. 5. It was experimentally proved that the maximum percentage increase in MRR of PMND-EDM was 17.85 % as compared to near- dry EDM, as shown in Fig. 6.

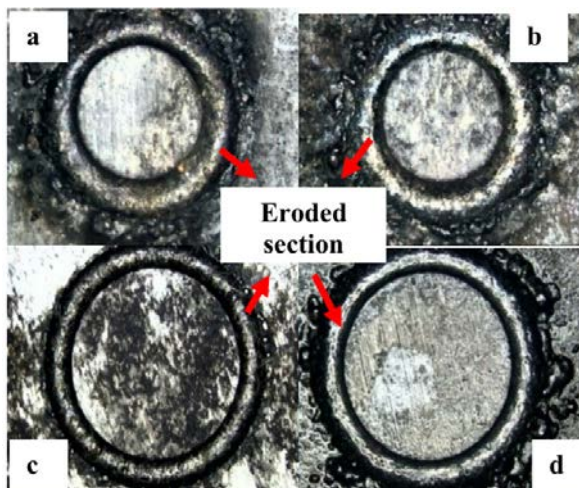


Fig. 5. EN -31 Sample machined by PMND-EDM; a) machined sample by tool 1, b) machined sample by tool 2, c) machined sample by tool 3, d) machined sample by tool 4

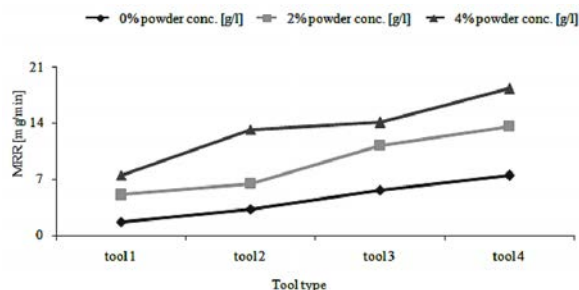


Fig. 6. Graph of MRR vs. tool type at different powder concentration

The plasma channel was small with a 2 % concentration of powder due to which fewer craters

can be seen after machining of the workpiece, as shown in Fig. 7. Intensive craters over the machined surface were observed in Fig. 8, which signifies that a higher erosion rate was achieved as the concentration of metallic powder was increased. A high energy enlarged plasma channel due to increased metallic powder concentration was the main reason for higher erosion. The electrical resistivity decreases, and the working gap expands due to the presence of metallic powder in EDM oil [3]. This phenomenon stabilizes the arc through better flushing and servo-hunting.

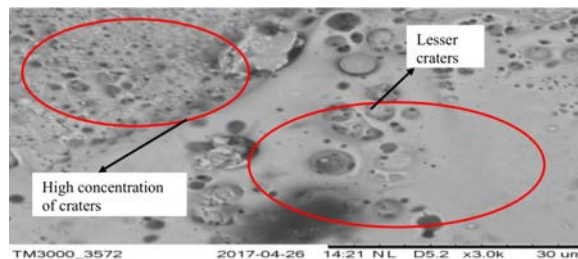


Fig. 7. SEM image of a machined surface with 2 g/l powder concentration (image width: 68.8 μm, accelerating voltage 15.0 kV)

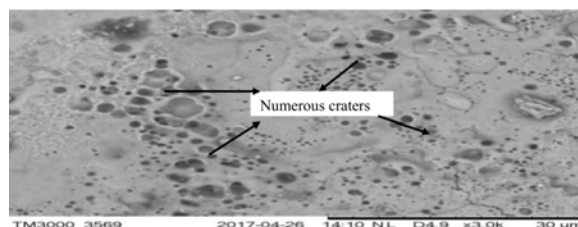


Fig. 8. SEM image of a machined surface with 4 g/l powder concentration (image width: 68.8 μm, accelerating voltage 15.0 kV)

#### 4.2 Influence of Machining Process on Surface Finish (Ra)

Metallic powder additives along with dielectric oil reduce the electric density and increase the spark gap, due to which the sparking over the machined surface is uniformly distributed [23]. It was observed that higher surface finish was achieved in machined products because the increased spark gap helped in effective debris removal from the machining area [2]. Powder concentration and the type of metallic powder were important factors in influencing the spark gap. The maximum percentage increase in surface finish was 16.36 % in PMND-EDM as compared to near-dry EDM as shown in Fig. 9. With a further increase of metallic powder concentration (4 %), the plasma channel becomes more uniformly energized and distributed. which gives better surface finish than that of the 2 % powder concentration.

Fig. 10 shows a machined surface with reduced cracks by PMND-EDM, which was also the reason to achieve better surface quality characteristics. Fig. 11 shows the surface of the workpiece machined at 4 % powder concentration. The peaks signify the height of the surface irregularities at different parts over the machined area. The variation of surface roughness in the images was signified by the pattern of yellow colour. The dark yellow colour of the image shows the area of lesser irregularities while bright yellow colour signifies the area of high irregularities over the machined surface. Similar analysis was performed for other machined products with 2 % powder concentration as well as in near-dry condition

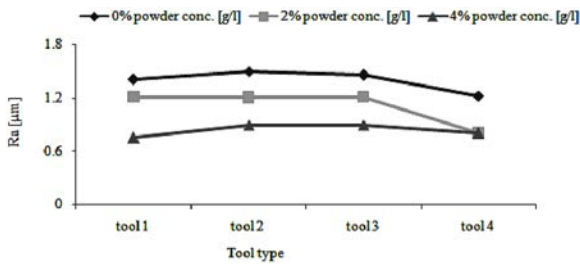


Fig. 9. Graph of surface roughness value vs. tool type at different powder concentration

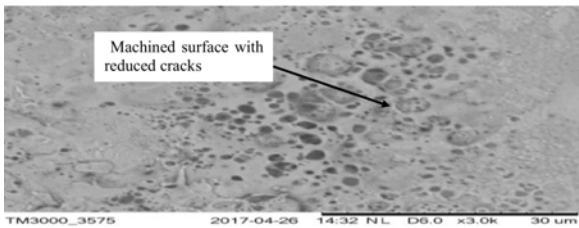


Fig. 10. SEM image of the machined area by PMND-EDM (Image width: 68.8 μm, accelerating voltage 15.0 kV)

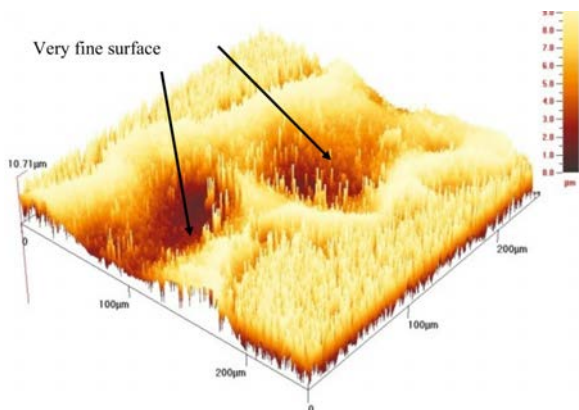


Fig. 11. 3-D image of surface roughness profile of the machined surface with 4 g/l powder in PMND-EDM

as shown in Figs. 12 and 13, respectively. At 2 % metallic powder concentration, the plasma is partially energized, which gives considerably better surface quality with lesser irregularities as shown in Fig. 12. Surface roughness decreases by adding zinc powder in the dielectric fluid, as added powder enlarges and widens the discharge gap between the electrodes. This results in the easy removal of debris, which leads to the improvement in surface quality. The powder particles distribute the spark energy uniformly, which results in shallow craters on the workpiece surface. It was revealed that by the addition of metallic powder, the discharging energy dispersion improves because insulating strength of the dielectric fluid reduces with the addition of metallic powder. These favourable conditions give a refined machined surface with a high surface finish. This proves that a significant role was played by the metallic powder to modify the channel

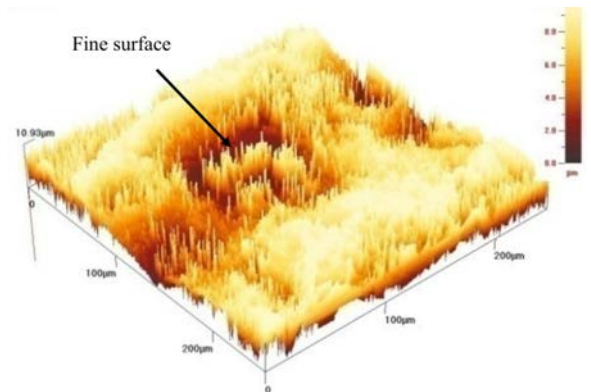


Fig. 12. 3-D image of surface roughness profile of the machined surface with 2 g/l powder in PMND-EDM

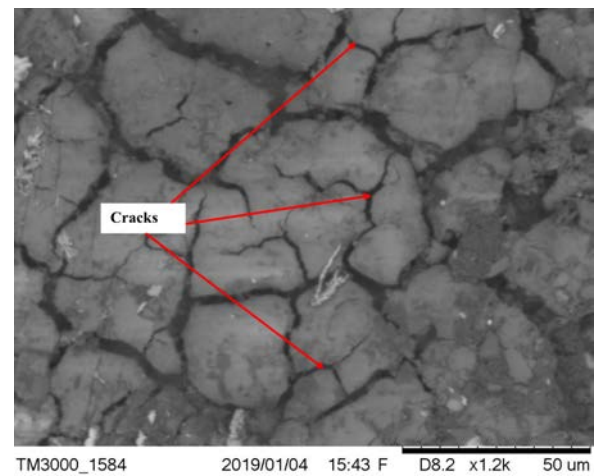


Fig. 13. SEM image of the machined area in near-dry EDM (image width: 68.8 μm, accelerating voltage 15.0 kV)

of the plasma, which gives even and uniform surfaces. While in near-dry EDM, an improper plasma channel was observed due to the absence of metallic powder. This leads to the formation of a large machined area with an uneven surface with cracks, as shown in Figs. 13 and 14. The cross-sectional area was analysed for a

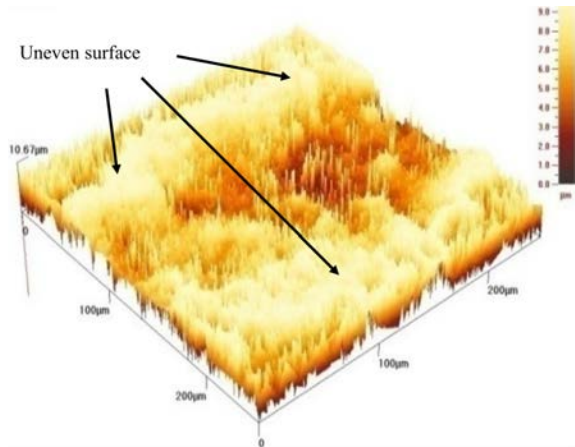


Fig. 14. 3-D image of surface roughness profile of machined surface with near-dry EDM

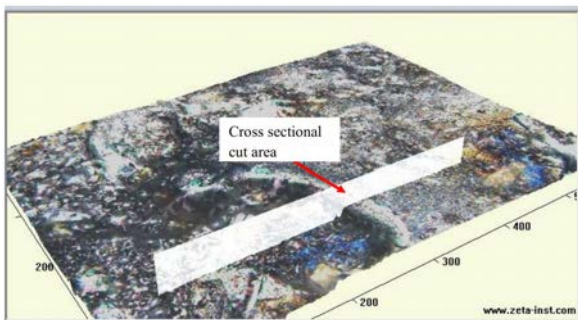


Fig. 15. 3-D image of the area for cross sectional study

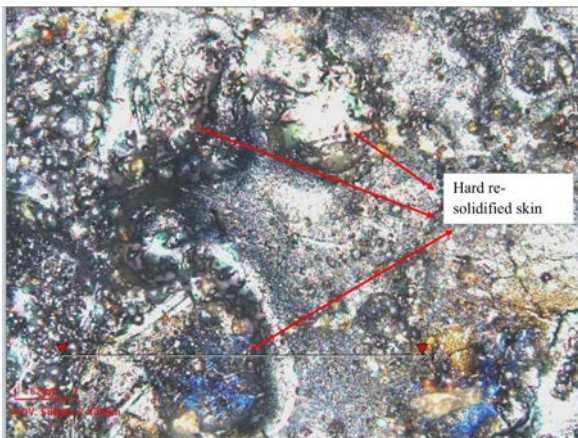


Fig. 16. Hard re-solidified melted region at the cross-section of machined EN-31 sample

re-melted zone at the machined area. The area cut for analysis is shown in Fig.15, while the cross-sectional re-solidified area of the molten metal is shown in Fig. 16.

### 4.3 Analysis of Residual Stress of Machined Surfaces

The residual stress analysis on the finished work-surfaces was performed with an X-ray residual analyzer (Pulstec limited model- $\mu$  X-360n). The machined workpiece sample information required for taking the measurement were lattice constant, crystal structure, diffraction plane, Young's modulus,

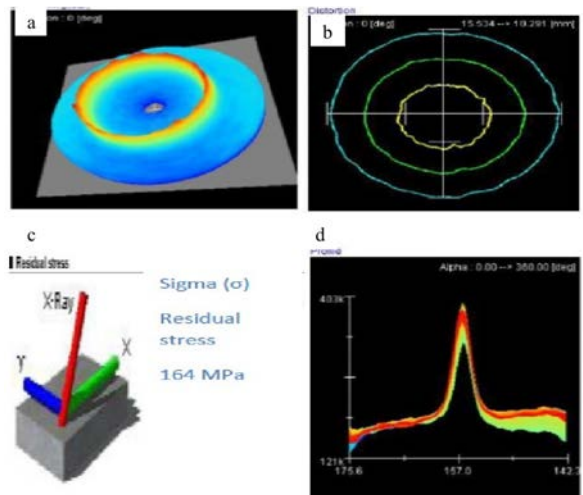


Fig. 17. Residual stress generated on work surface after machining without any metallic powder (ND-EDM); a) debye ring, b) distortion ring, c) residual stress, and d) peak profile

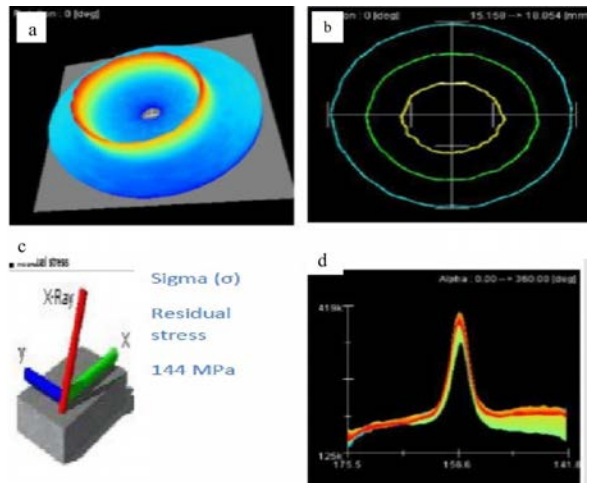
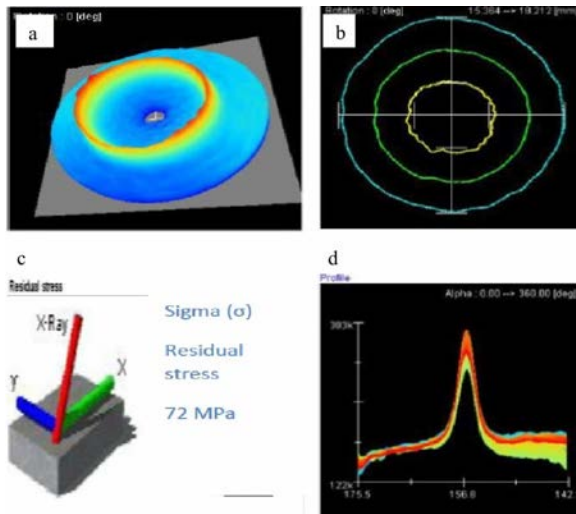


Fig. 18. Residual stress generated on work surface after machining with 2 % metallic powder by PMND-EDM; a) debye ring, b) distortion ring, c) residual stress, and d) peak profile

and Poisson ratio. The X-Ray residual stress measuring principle was based on Bragg's law. X-ray irradiation time was set up for 30 seconds while X-ray tube current and voltage were 1 mA and 30 kV, respectively. Sample distance was set at 39 mm, and the angle of incidence of the X-ray was set at 35 degree while the wavelength of the X-ray was 2.29 Å. All the measurements were taken at room temperature of 26 °C. Fig. 17 shows the residual stress analysis of machined surface by ND-EDM at 0 % powder concentration (ND-EDM). A Debye ring can be seen, which indicates residual stress distribution over the machined surface. The red ring signifies the region of maximum stress concentration while the yellow region signifies a region of comparatively lower stress induced at the machined surfaces, while the blue region signifies region of minimum induced stress. Other relevant information about the stress peak position and peak profile over the finished surface of the workpiece are also shown in Fig. 17. In ND-EDM, the residual stress measured by the machine was 164 MPa (tensile), as shown in Fig. 17. The value of stress of the machined surfaces by PMND-EDM with 2 % metallic powder concentration was 144 MPa (tensile), as shown in Fig. 18, which was lower compared to the stresses in the workpiece machined by ND-EDM. On further increasing the metallic powder concentration to 4 % in PMND-EDM, the residual stresses further reduced to a value of 72 MPa (tensile), as shown in Fig. 19. The comparative graph of different residual stresses of machined surfaces by ND-EDM and PMND-EDM is shown in Fig. 20. The maximum



**Fig. 19.** Residual stress generated on work surface after machining with 4 % metallic powder by PMND-EDM: a) debye ring, b) distortion ring, c) residual stress, and d) peak profile

decrease in residual stress was found to be 56.09 % in PMND-EDM as compared to ND-EDM. The reason for the decrease in residual stresses in PMND-EDM can be attributed to the uniform distribution of heat or energy plasma over the machined surface and improved flushing condition, which ultimately relieves some part of the residual stresses over the machined surfaces.

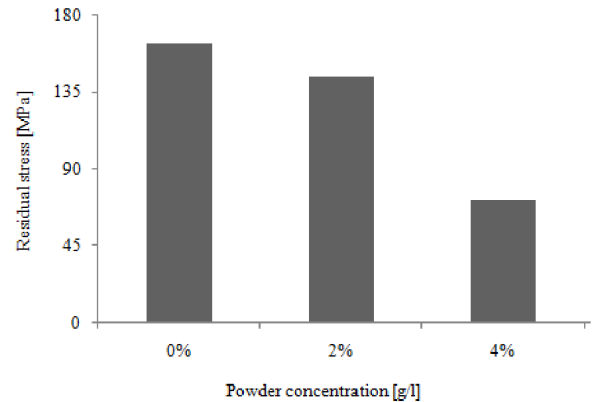


**Fig. 20.** Graph of the residual stress of machined products at different powder concentrations

#### 4.4 Analysis for Micro-Hardness of Machined Surface by PMND-EDM

MH analysis for product machined by ND-EDM and PMND-EDM was performed with help of Fischerscope instrument (HM2000S model, USA). This instrument utilizes a carbide indenter which indents with respect to the increase in value of load applied. The topography of the machined surface of the workpiece was improved by metallic powder in the dielectric medium because these additives were responsible for reducing the surface pits over the machined surface. There was an improvement in surface properties with the addition of conductive powder in the dielectric medium due to the surface modification such as the formation of a solidified layer of zinc. The MH of the die steel workpiece was increased by adding chromium powder to the dielectric medium [24]. An MH of 1600 HV was achieved with the addition of titanium powder to the dielectric [25]. This metallic powder leads to the formation of titanium carbide layer on carbon steel when machined with a copper tool.

In this study, the Vickers hardness number (HV) for machined part at 0 % powder concentration was found to be 194 HV, but with powder additive machining this value increased to the maximum value

of 520 HV at 4 % powder concentration. The powder additives changed the surface topography of the machined surface by forming a solidified recast layer, which was responsible for surface modification. This phenomenon increased the MH by 69.63 %, as shown in Fig. 21.

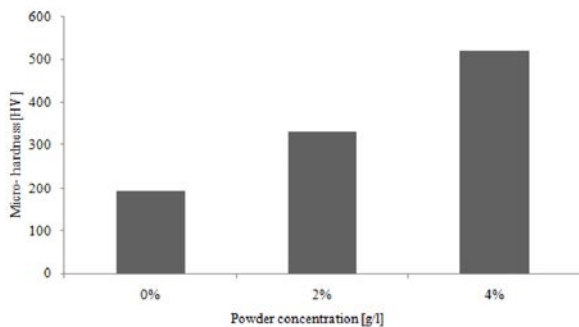


**Fig. 21.** MH of machined products at different metallic powder concentration

## 5 CONCLUSIONS

In this article, experimental investigations have been conducted regarding the PMND-EDM process. The metallic powder (zinc) as an additive along with a mist of dielectric medium was used for performance enhancements, and the following conclusions were made.

1. In PMND-EDM, the MRR was influenced by powder concentration. The MRR increases with an increase in metallic powder concentration and maximum increase in MRR was 17.85 % as compared to ND-EDM.
2. Surface finish was improved by 16.36 % in PMND-EDM as the sparking is uniformly distributed among the powder particles, which gives even and uniform machined surfaces.
3. There was a decrease in residual stress by 56.09 % over the machined surfaces in PMND-EDM as compared to the ND-EDM process.
4. The maximum increase MH was 62.69 % over the machined surface in PMND-EDM as compared to ND-EDM.

## 6 REFERENCES

[1] Tanimura, T., Isuzugawa, K., Fujita, I., Iwamoto, A., Kamitani, T. (1989). Development of EDM in the Mist. *Proceedings of Ninth International Symposium of Electro Machining*, vol. 9, p. 313-316.

[2] Jeswani, M.L. (1981). Effects of the addition of graphite powder to kerosene used as the dielectric fluid in electrical

discharge machining. *Wear*, vol. 70, no. 2, p. 133-139, DOI:10.1016/0043-1648(81)90148-4.

- [3] Wong, Y.S., Lim, L.C., Rahuman, I., Tee, W.M. (1998). Near-mirror-finish phenomenon in EDM using powder-mixed dielectric. *Journal of Materials Processing Technology*, vol. 79, no. 1-3, p. 30-40, DOI:10.1016/S0924-0136(97)00450-0.
- [4] Kansal, H.K., Singh, S., Kumar, P. (2005). Parametric optimization of powder mixed electric discharge machining by response surface methodology. *Journal of Materials Processing Technology*, vol. 169, no. 3, p. 427-436, DOI:10.1016/j.jmatprotec.2005.03.028.
- [5] Tripathy, S., Tripathy, D.K. (2017). Optimization of process parameters and investigation on surface characteristics during EDM and powder mixed EDM. Bajpai, R., Chandrasekhar, U. (eds.). *Innovative Design and Development Practices in Aerospace and Automotive Engineering. Lecture Notes in Mechanical Engineering*. Springer, p. 385-391, DOI:10.1007/978-981-10-1771-1\_41.
- [6] Singh, J., Sharma, R.K. (2016). Assessing the effects of different dielectrics on environmentally conscious powder-mixed EDM of difficult to machine material (WC-Co). *Frontiers of Mechanical Engineering*, vol.11, p. 374-387, DOI:10.1007/s11465-016-0388-8.
- [7] Bai, X., Zhang, Q.-H., Li, T.T., Zhang, Y.-H. (2012). Research on the medium breakdown mechanism of powder mixed near-dry electrical discharge machining. *Chinese Journal of Mechanical Engineering*, vol. 48, p. 186-192, DOI:10.3901/JME.2012.07.186.
- [8] Bai, X., Zhang, Q.H., Yang, T.Y., Zhang, J.H. (2013). Research on material removal rate of powder mixed near-dry electrical discharge machining. *International Journal of Advanced Manufacturing Technology*, vol. 68, p. 1757-1766, DOI:10.1007/s00170-013-4973-2.
- [9] Bai, X., Zhang, Q.H., Zhang, J.H., Kong, D., Yang, T. (2013). Machining efficiency of powder mixed near-dry electrical discharge machining based on different material combinations of tool electrode and workpiece electrode. *Journal of Manufacturing Processes*, vol. 15, no. 4, p.474-482, DOI:10.1016/j.jmpro.2013.09.005.
- [10] Wang, X., Liu, Y., Zhang, Y., Sun, Q., Li, Z., Shen, Y. (2016). Characteristics of plasma channel in powder-mixed EDM based on monopulse discharge. *International Journal of Advanced Manufacturing Technology*, vol. 82, p. 1063-1069, DOI:10.1007/s00170-015-7236-6.
- [11] Kumar, M., Datta, S., Kumar, R. (2018). Electro-discharge machining performance of Ti-6Al-4V Alloy: Studies on parametric effect and phenomenon of electrode wear. *Arabian Journal for Science and Engineering*, vol. 10, p. 1-16, DOI:10.1007/s13369-018-3632-1.
- [12] Öpöz, T.T., Yasar, H., Ekmekci, N., Ekmekci, B. (2018). Particle migration and surface modification on Ti<sub>6</sub>Al<sub>4</sub>V in SiC powder mixed electrical discharge machining. *Journal of Manufacturing Processes*, vol. 31, p. 744-758, DOI:10.1016/j.jmpro.2018.01.002.
- [13] Khullar, V.R., Sharma, N. Kishore, S., Sharma, R. (2017). RSM- and NSGA-II-based multiple performance characteristics optimization of EDM Parameters for AISI 5160.

- Arabian Journal for Science and Engineering*, vol. 42, p. 1917-1928, DOI:10.1007/s13369-016-2399-5.
- [14] Liu, J.F., Guo, Y.B. (2016). Residual stress modeling in electric discharge machining (EDM) by incorporating massive random discharges. *Procedia CIRP*, vol. 45, p. 299-302, DOI:10.1016/j.procir.2016.02.060.
- [15] Rao, P.S., Ramji, K., Satyanarayana, B. (2016). Effect of wire EDM conditions on generation of residual stresses in machining of aluminum 2014 T6 alloy. *Alexandria Engineering Journal*, vol. 55, no. 2, p. 1077-1084, DOI:10.1016/j.aej.2016.03.014.
- [16] Shabgard, M., Seydi, S., Seyedzavvar, M. (2016). Novel approach towards finite element analysis of residual stresses in electrical discharge machining process. *International Journal of Advanced Manufacturing Technology*, vol. 82, p. 1805-1814, DOI:10.1007/s00170-015-7510-7.
- [17] Kumar, S., Grover, S., Walia, R.S. (2018). Effect of hybrid wire EDM conditions on generation of residual stresses in machining of HCHCr D2 tool steel under ultrasonic vibration. *International Journal on Interactive Design and Manufacturing*, vol. 12, p. 11119-1137, DOI:10.1007/s12008-018-0474-8.
- [18] Gill, A.S., Kumar, S. (2018). Investigation of micro-hardness in electrical discharge alloying of En31 tool steel with Cu-W powder metallurgy electrode. *Arabian Journal for Science and Engineering*, vol.43, p. 1499-1510, DOI:10.1007/s13369-017-2960-x.
- [19] Chundru, V.R., Koona, R., Pujari, S.R. (2019). Surface modification of Ti<sub>6</sub>Al<sub>4</sub>V alloy using EDM electrode made with nano- and micron-sized TiC/Cu powder particles. *Arabian Journal for Science and Engineering*, vol. 44, p. 1425-1436, DOI:10.1007/s13369-018-3561-z.
- [20] Kumar, S., Batra, U. (2012). Surface modification of die steel materials by EDM method using Tungsten powder-mixed dielectric. *Journal of Manufacturing Processes*, vol. 14, no. 1, p. 35-40, DOI:10.1016/j.jmapro.2011.09.002.
- [21] Kumar, S., Singh, R., Batish, A., Singh, T.P., Singh, R. (2017). Investigating surface properties of cryogenically treated titanium alloys in powder mixed electric discharge machining. *Journal of the Brazilian Society of Mechanical Sciences and Engineering*, vol. 39, p. 2635-2648, DOI:10.1007/s40430-016-0639-y.
- [22] Sundriyal, S., Vipin, Walia, R.S. (2020). Experimental investigation on micro-hardness of EN-31 die steel in powder mixed near dry electric discharge machining method. *Strojniški vestnik - Journal of Mechanical Engineering*, vol. 66, no. 3, p. 184-192, DOI:10.5545/sv-jme.2019.6474.
- [23] Zhao, W.S., Meng, Q.G., Wang, Z.L. (2002). The application of research on powder mixed EDM in rough machining. *Journal of Materials Processing Technology*, vol. 129, no. 1-3, p. 30-33, DOI:10.1016/S0924-0136(02)00570-8.
- [24] Tripathy, S., Tripathy, D.K. (2017). An approach for increasing the micro-hardness in electrical discharge machining by adding conductive powder to the dielectric. *Materials Today: Proceedings*, vol. 4, no. 2, p. 1215-1224, DOI:10.1016/j.matpr.2017.01.140.
- [25] Furutani, K., Saneto, A., Takezawa, H., Mohri, N., Miyake, H. (2001). Accertation of titanium carbide by electrical discharge machining with powder suspended in working fluid. *Precision Engineering*, vol. 25, no. 2, p. 138-144, DOI:10.1016/S0141-6359(00)00068-4.

# Experimental Investigations of Thin-layer Drying of Leaves in a Heat-Pump Assisted Tray-type Batch Drying Chamber

A.K. Babu<sup>1,\*</sup> – G. Kumaresan<sup>2</sup>, – V. Antony Aroul Raj<sup>3</sup>, – R. Velraj<sup>2</sup>

<sup>1</sup> Easwari Engineering College, Department of Automobile Engineering, Chennai, India

<sup>2</sup> Institute for Energy Studies, Anna University, Chennai, India

<sup>3</sup> Easwari Engineering College, Department of Mechanical Engineering, Chennai, India

The design of a batch drying chamber with multiple trays for the thin-layer drying of fragile, heat-sensitive food materials, such as edible leaves, is a challenging task. It is essential to ensure good air distribution with minimum pressure drop in all the compartments of the drying chamber to obtain uniform drying of the product. In the present work, a drying chamber that was optimized from different configurations using computational fluid dynamics (CFD) software was fabricated and tested in the heat pump dryer. The experimental investigation was carried out with an optimized configuration for the temperature range of 50 °C to 60 °C, the relative humidity range of 20 % to 12 %, and air velocities of 1.41 m/s, 2.39 m/s, and 3.24 m/s. These optimal operating conditions were chosen based on an extensive literature survey on leaf drying. It was found that the drying process took place only in the falling rate period, fully controlled by the mechanism of liquid diffusion. The effects of air velocity on the performance parameters of the dryer were studied. Calculations based on the mean average parameters of the experimental data showed that a relatively higher heat utilization factor (0.17), moisture extraction ratio (0.375 kg/h), specific moisture extraction ratio (0.1529 kg/(kWh)), coefficient of performance (4.60), drying efficiency (76.23 %) and lower specific energy consumption (1.16 kW/kg) were obtained for a moderate drying velocity of 2.39 m/s in the heat pump drying process due to higher convection mass and heat transfer effects. Drying curves were plotted for different drying conditions and discussed. The findings were in agreement with those of many earlier research studies listed in the references section. The tested drying chamber can be used for drying all kinds of leaves in a heat pump dryer.

**Keywords:** Amaranth leaves, batch dryer, heat pump dryer, coefficient of performance, thin-layer drying

## Highlights

- A drying chamber optimized from different configurations using computational fluid dynamics (CFD) software is fabricated and tested in a heat pump dryer for drying Amaranth leaves.
- Good air distribution with minimum pressure drop is ensured in all the compartments of the newly designed drying chamber to obtain uniform drying of the product.
- The drying process of batches of spread-out material takes place only in the falling rate period.
- Better results are obtained for a moderate drying velocity of 2.39 m/s in the heat pump drying process.
- Air velocity, relative humidity, and the drying temperature are found to influence the rate of drying mutually.
- The newly designed drying chamber is suitable for drying all kinds of leaves in a heat pump dryer.

## 0 INTRODUCTION

Amaranth leaves are a storehouse of many phytonutrients, antioxidants, minerals, and vitamins that are essential for good health and wellness. Fresh Amaranth leaves are one of the richest sources of vitamin C; 100 g of fresh leaves carry 43.3 mg or 70 % of the recommended daily intake of this vitamin. Vitamin C is a powerful water-soluble antioxidant that plays a vital role in healing wounds and helps the body fight and ward off viral infections [1]. Amaranth leaves can be dried all year round in India, and a few thousand tons are exported annually. Fresh Amaranth leaves can be easily dried in a tray dryer without degradation.

When hot air is blown over wet food, heat is transferred to the surface, and latent heat of vaporization causes water to evaporate. Water vapour

diffuses through a boundary film of air and is carried away by moving air. Different drying methods are applied for drying Amaranth leaves. When dried in the open air, the drying time is about 10 days to 12 days. There are some disadvantages associated with the open-air sun drying of Amaranth leaves, which are related to the contamination with impurities, such as airborne dust, soil, sand particles and insects. Also, the process is weather-dependent, and accompanied by bleaching due to ultraviolet (UV) and chlorophyll depletion [2]. The drying process also involves a lot of material handling and manual labour, and the drying time can be quite long. Non-uniform and delayed drying process significantly changes the leaf colour, which results in a lower price in the market. Rainfall and windy weather can hamper the complete drying process. Therefore, the drying process is generally undertaken within closed equipment to improve the

quality of the final product. With this controlled, low contact time drying process, vital nutrients, as well as the inherent colour and low volatile fragrance components, are retained to the maximum extent possible in the final dried materials within its limiting moisture levels for longer storage periods [3]. Once-through drying is a simple method, but obtaining all of the above-mentioned controlled conditions while maintaining high drying rates and heat efficiency with a short retention time of the material to be dried is difficult.

There are many closed-type once-through dryers used for dehydration of leaves. Efficiencies are generally higher for heat-pump drying (95 %) compared to vacuum drying (less than 70 %), and hot-air convective drying (between 35 % to 40 %) [4]. Also, a medium-range of temperatures (40 °C to 60 °C) and low relative humidity (12 % to 20 %) for safe drying of heat-sensitive leaves have been achieved experimentally in a heat-pump dryer (HPD) [5].

Benedicic [6] observed that drying products in a condenser dryer, which includes a fan, a heat-pump, and air duct, was complicated as all drying parameters, such as product moisture content, ambient temperature and humidity conditions, temperature and humidity, in the process were varied and mutually influenced each other during the drying operation. He also found that a controlled air-flow system was suitable for drying products of higher density and drying was also more economical in a condenser dryer. Cerci et al. [7] designed a drying chamber for drying zucchini, which distributed hot air uniformly. Aktas et al. [8] reported that a high velocity of drying air (3 m/s) had the lowest drying time for mint leaves. Their findings were supported by Premi et al. [9] for drumstick leaves and Kumar et al. [10] for mint leaves. Doymaz et al. [11] reported that optimum drying air temperature (50 °C to 60 °C) resulted in significantly reducing drying time for dill and parsley leaves. Their findings were in line with those of Rayaguru and Routray [12]. Hossain et al. [13] found that low relative humidity (20 %) played an important role in reducing the moisture content of herbs (89 %wb) (wet basis) to safe final levels (9 %wb). Fatouh et al. [14] observed that drying air temperature and air velocity had a significant effect on the drying rate. From their experimental investigation on drying herbs using HPD, it was noted that moderate air temperature (55 °C) and air velocity (2.7 m/s) resulted in the maximum drying rate. Almost all the research studies on leaf drying indicate that drying occurs in the falling rate period. This is usually the longest period of drying operation. Constant rate period was observed only in a few cases [2].

In the present work, a drying chamber that is optimized from different configurations using computational fluid dynamics (CFD) software is fabricated and used in the heat pump dryer [15].

The main objective of this research is to investigate the effect of a new batch drying chamber in a tray dryer using a closed-loop heat pump drying process (herein known as heat pump assisted tray dryer (HPATD)) on overall dryer performance for leaf drying.

## 1 METHODS

### 1.1 Sample Preparation

Fresh Amaranth leaves were purchased from a local wholesale market in Chennai, Tamil Nadu, India. The leaves were first washed clean with running water and sorted to remove the unwanted parts, such as stems and older leaves. Three trays were used for the study, and each tray was loaded with 0.5 kg of leaves. Most of the procured leaves were of uniform maturity and good quality.

### 1.2 Dry Matter

The dry weight of the leaves was found by drying samples in a drying oven at  $105 \pm 2^\circ \text{C}$  [16]. After consecutive measurements, the samples were considered to be dry when the weight change was below 1 %.

## 2 EXPERIMENTAL PROCEDURE

### 2.1 Experimental Setup

The experimental analysis with HPATD was carried out based on the conditions mentioned in Table 1. These conditions were selected based on the in-depth literature survey [1], [5], [8], [14], [17] and [18].

**Table 1.** Testing conditions for the drying of Amaranth leaves

Conditions	Value
Temperature [°C]	30 to 60
Velocity [m/s]	1.47, 2.39 and 3.24
RH [%]	61.5 to 12.5

The technical specifications of various components involved in HPATD are mentioned in Table 2. The measuring devices/instruments used in this study, and their accuracy is given in Table 3.

**Table 2.** Technical specifications of heat pump components

Components	Specifications
Evaporator	Aluminum finned copper tube, 2.78 m <sup>2</sup> , 5 fins/cm
Metering device (capillary tube)	91.5 cm length, 0.15 cm diameter, Number of circuits 2.
Condenser	Aluminum-finned copper tube, 3.60 m <sup>2</sup>
Compressor	Hermetically sealed reciprocating type, cylinder volume 51.7 cm <sup>3</sup> /rev, nominal power 2350 W, heating power 7330 W, 1.86 kW motor.
Fan	Axial type, 1330 rpm, 90 W, Hicool, China.

**Table 3.** Measuring devices/instruments

Measured quantities	Measurement devices	Measurement ranges	Accuracy
Mass of the product	Electronic weighing balance	0 kg to 20 kg	±2 g
Air velocity	Rotating anemometer [m/s]	0.1 to 10	±0.1
Air temperature in the drying chamber [°C]	Electronic thermostat RTD PT100	-99 to +400	±0.1
RH of air in the drying chamber	Digital Humidistat	20 % to 90 %	±5 % RH
	Electronic thermostat RTD PT100	-99 to +400 °C	±0.1 °C
Refrigerant pressure [psi]	Bourdon tube	Evaporator side -30 to 150	±2
		Condenser side 0 to 500	±10
Refrigerant temperature [°C]	Electronic thermostat RTD PT100	-99 to +400	±0.1
Power consumption [V]	Electrical power meter	180 to 260	-

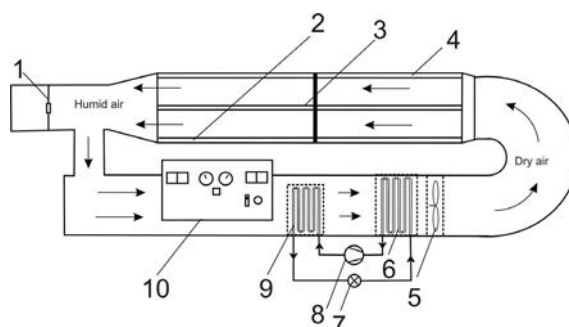
**2.1.1 Description of the Dryer**

Fig. 1 shows the line diagram of the HPATD fabricated for the experimental work. The developed HPATD is a closed insulated chamber consisting of a dehumidifier unit, with an evaporator, hermetic compressor, expansion valve, and condenser at its lower portion and a drying chamber at its upper portion.

The refrigerant R134a is chosen as the working fluid and charged in the system. The dryer consists of three sections: the heating section, the airflow section, and the drying chamber. The drying chamber is horizontal, with annulus airflow parallel to the static drying material. The air is forced through an axial fan. Heated dry bulb temperatures are measured with the installed copper-constantan thermocouples. At the inlet and outlet of the drying chamber, the RH of air is measured by thermo-hygrometers.

A damper is inserted at the drying chamber outlet to alter the overall airflow rate. The velocity of airflow is measured using a digital anemometer (HTC,

AVM-06, ±0.1 ms<sup>-1</sup>, made in Taiwan) at the outlet of the drying chamber. A long diffuser with rectangular end cross-section with minimum pressure drop is used at the drying chamber air inlet. These two accessories help in ensuring a more uniform and straight airflow in the drying chamber. There is no inclination and no geometrical changes perpendicular to the airflow direction in the drying chamber. Uniform airflow distribution with a minimum pressure drop is a mandatory parameter because it has a significant effect on the homogeneity of the leaves being dried.



**Fig. 1.** Experimental setup; 1 damper, 2 tray-1, 3 tray-2, 4 tray-3, 5 fan, 6 condenser, 7 expansion valve, 8 compressor, 9 evaporator, 10 control panel

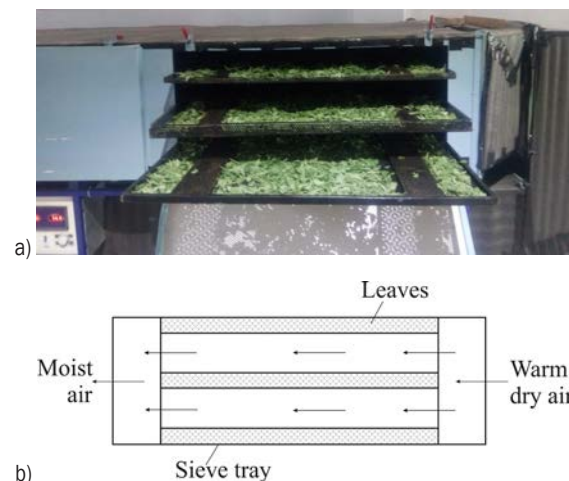


**Fig. 2.** Drying chamber; a) photographic view, and b) schematic diagram

The drying chamber has three perforated stainless steel trays placed parallel to each other. The dimensions of the drying compartment are 2.7 m × 1 m × 0.8 m. These trays are tightly embedded in the drying chamber to prevent all possible leaks, and the chamber walls are thermally insulated with Thermorex (6 mm) to reduce heat loss. Experiments are carried out at three levels of inlet air velocity (3.24 m/s, 2.39

m/s, and 1.41 m/s) with varying drying temperatures and percentages of RH.



Fig. 3. Photograph of the experimental apparatus

The major advantage of this setup is that the parameters (drying air temperature, drying air relative humidity, and drying air velocity) have been controlled to operate at constant optimized variable conditions.

### 2.1.2 Experimental Procedure

In this experiment, the drying chamber is maintained at a transient state condition in terms of temperature and relative humidity during the early part of the drying process, after which the operating conditions are almost stable. The humid air from the drying chamber outlet is passed over the evaporator of the heat pump, which acts as a dehumidifier. In this section, the humid atmospheric air loses moisture by cooling and giving up condensing heat to the vaporizing low-pressure refrigerant. The cooled dry air then passes over the condenser, where it is heated by the condensing high-pressure refrigerant vapour. The heated air then flows parallel to the drying product spread over the stacked trays. The drying air is circulated using an axial fan in a closed cycle, and fresh air is not allowed into the system. The velocity of airflow in the HPATD is altered with the help of a fan speed regulator. The dryer tested in this work is applied in transit drying [19]. The leaves can be dried during transportation using waste heat released from the radiator of the cooling system and the condenser of the vehicle air-conditioning system of the transit vehicle.

The gross weight of 1.5 kg fresh Amaranth leaves is used in conducting the experimental work. A uniform layer of 2 cm thickness is spread over all three trays, with each tray having about 0.5 kg. The initial moisture content of the Amaranth leaf is measured to be 89.3 % (wet basis) according to the procedure of ASAE standard S358.2, 1997 [20]. The drying cycle starts as soon as the trays are placed in the drying chamber. All trays with Amaranth leaves are weighed accurately at the beginning and the end of the drying cycle using an electronic balance of  $\pm 0.01$

kg accuracy. Before starting an experimental run, the whole apparatus is operated for several hours for calibration purposes.

The initial moisture content has to be reduced up to 7 % to 10 % to obtain the desired final moisture content [2]. When the weight of the sample becomes constant, the experiment is stopped. The dryer is working with a closed circuit, and the moisture content of Amaranth leaves is measured based on water removed from the evaporator cooling coil of the heat pump. The moisture loss, drying time, the air temperature inside the chamber, relative humidity, air recirculation rate, and ambient temperature are considered as base data for the determination of moisture content, moisture ratio, drying rate, etc.

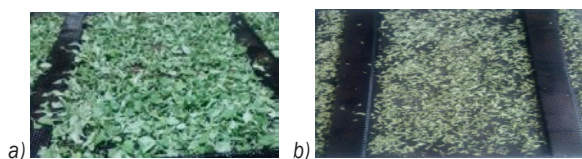


Fig. 4. A photographic view of Amaranth leaves; a) before drying, and b) after drying

## 2.2 Modelling of Thin-Layer Drying

The drying performance of the dryer is determined based on heat utilization, the coefficient of performance, the quantity of the dried leaves, rate of drying, rate of consumption of electricity, and other operating conditions. Continuous dryers alone have constant rates of drying. The batch dryer can be evaluated only by overall utilities of power, operation time, heat energy cost, and the quality of the dried product.

### 2.2.1 Heat Utilization Factor

The heat utilization factor (*HUF*) may be defined as the ratio of temperature decrease due to cooling of the air during drying and the temperature increase due to heating of air. The *HUF* is determined by using Eq. (1) [21].

$$HUF = \frac{t_1 - t_2}{t_1 - t_o}, \quad (1)$$

where  $t_o$ ,  $t_1$  and  $t_2$  are dry bulb temperature of ambient air, drying chamber inlet air, and drying chamber outlet air in [K], respectively.

*HUF* may be more than unity under certain drying conditions. *HUF* for a heat pump assisted dryer should be as high as possible to achieve a higher

drying rate. At higher *HUF* values, moisture carried away from the leaves by the drying air is at maximum.

### 2.2.2 Coefficient of Performance

The coefficient of performance (*COP*) can be used to evaluate the amount of work converted into heat for two different system operations: cooling and heating. For a heat pump, the heat transfer from the system to the hot body is desired, and the coefficient of performance is expressed as [22],

$$COP = \frac{Q_{cd}}{W_c}, \quad (2)$$

where,  $Q_{cd}$  is the heat delivered by the condenser in [kW], and  $W_c$  is the power input to the compressor. When calculating the *COP* for a heat pump, the heat output from the condenser ( $Q_{cd}$ ) is compared to the power supplied to the compressor ( $W_c$ ). The range of *COP* is usually between 4 and 6 for heat pump drying.

Heat delivered by the condenser can be calculated from Eq. (3) [23].

$$Q_{cd} = m_a C_p (t_1 - t_3), \quad (3)$$

where  $m_a$  is the mass flow rate of air in [kg/s],  $C_p$  is the specific heat of air, in [kJ/(kgK)], and  $t_3$  is the drying air temperatures at condenser inlet in [K], respectively.

### 2.2.3 Moisture Content

The percentage of moisture content (*M*) of Amaranth leaves is calculated by Eq. (4) [24]:

$$M = \frac{w_i - w_d}{w_i} \times 100, \quad (4)$$

where,  $w_i$  and  $w_d$  are mass of the sample before drying and after drying.

The moisture content in freshly harvested leaves is 77 %wb to 91 %wb while that required for storage is 7 %wb to 10 %wb.

### 2.2.4 Moisture Ratio

Moisture ratio (*MR*) of Amaranth leaves is calculated by Eq. (5) [24].

$$MR = \frac{M_t - M_e}{M_i - M_e}, \quad (5)$$

where,  $M_t$ ,  $M_i$ , and  $M_e$  are the moisture content at  $t$ , initial moisture content, and equilibrium moisture content, respectively. The values of  $M_e$  are too small

to be compared to  $M_t$  or  $M_i$  for a long period and hence, Eq. (5) for *MR* is finally written as  $M_t/M_i$ .

### 2.2.5 Weight of Dry Material

Weight of dry material ( $w_d'$ ) is calculated by Eq. (6) [21]:

$$w_d' = w_i \left[ \frac{100 - M}{100} \right], \quad (6)$$

where,  $w_i$  is the initial weight of the sample in grams and  $M$  is the moisture content of sample feed in %wb.

### 2.2.6 Drying Rate

The drying rate (*R*) in a gram of water per min per 100 g of dry matter during drying experiments is calculated by using Eq. (7) [21].

$$R = \frac{w_d}{t \times \left( \frac{w_d' [g]}{100} \right)}, \quad (7)$$

where  $t$  is the drying time in minutes.

### 2.2.7 Moisture Extraction Rate

Moisture extraction rate (*MER*) [kg/h] is defined as a kilogram of moisture removed per hour and indicates the dryer capacity or throughput rate. *MER* is given by Eq. (8) [25].

$$MER = \frac{(w_i - w_d)}{t}, \quad (8)$$

where,  $(w_i - w_d)$  is the amount of water removed during drying.

### 2.2.8 Specific Moisture Extraction Rate

The specific moisture extraction rate (*SMER*) [kg/(kWh)] describes the effectiveness of the energy used in the drying process. *SMER* is defined as a kilogram of moisture removed per kilowatt-hour consumed energy and is related to the total power to the dryer, including the fan power and the efficiencies of the electrical devices. *SMER* is calculated by Eq. (9) given below [25].

$$SMER = \frac{(w_i - w_d)}{E_c}, \quad (9)$$

where,  $E_c$  is the total energy supplied in the drying process

## 2.2.9 Specific Energy Consumption

Specific energy consumption ( $SEC$ ) [kW/kg], which is the reciprocal of  $SMER$ , is used to compare the energy efficiencies of different types of dryers. The  $SEC$  is defined as the total energy required to remove one kg of water.  $SEC$  is calculated according to Eq. (10) [25].

$$SEC = \frac{E_c}{(w_i - w_d)} \quad (10)$$

## 2.2.10 Drying Efficiency

The effective heat efficiency is mathematically defined by Eq. (11) [13] and [21].

$$\eta_d = \frac{t_1 - t_2}{t_1 - t_w} \quad (11)$$

where  $t_w$  is wet bulb temperature of drying air in [°C].

## 3 RESULTS AND DISCUSSION

The drying experiments were carried out in June and July 2018 in the Thermal Engineering Laboratory located in Easwari Engineering College, Chennai, South India. Each experiment was started at 9.00 a.m. and continued until the weight of the samples became constant. In the drying process, the temperature, the velocity, and relative humidity of the drying air had a considerable effect on drying and were the important parameters to determine the quality of the dried products. Velocity was taken as the constant parameter while varying temperature and relative humidity of the drying air, and the experiment was carried out. The dryer performance was evaluated, and drying curves were drawn to study the drying characteristics of Amaranth leaves.

### 3.1 Dryer Performance

The mean  $HUF$ ,  $MER$ ,  $SMER$ ,  $SEC$ ,  $COP$ , and drying efficiency values for three different velocities are tabulated in Table 4.

As shown in Table 4, the relatively best values (higher  $HUF$ ,  $MER$ ,  $SMER$ ,  $COP$ , drying efficiency,

and lower  $SEC$ ) were obtained for a moderate drying velocity of 2.39 m/s in the heat pump drying process. The results obtained showed good agreement with the results of earlier studies available in the literature [18] and [26].

The  $SMER$  and  $MER$  values increased with a decrease in drying air velocity due to more drying potential of medium temperature air. The specific moisture extraction rate when using HPATD for drying Amaranth leaves was more at a high velocity of drying air (0.1529 kg/(kWh)) than low velocity (0.1512 kg/(kWh)). This was due to lesser energy requirement and higher drying potential of low RH air in HPATD.

The energy consumption of HPATD for 270 to 390 minutes of operation was found to be less (1.16 kW/kg to 1.27 kW/kg) when operating under different drying velocity conditions. It was observed that the variation of energy requirement was not much as the compressor had to operate for the same duration leading to almost equal energy consumption.

The maximum average  $COP$  of the HPATD was 4.60 for a moderate drying velocity of 2.39 m/s, which was relatively higher for better conversion of work into heat. Usually,  $COP$  increases with increasing air recirculation. Here, an increase in  $COP$  was observed for the moderate velocity of air, which was because of the increase in the temperature difference between temperatures at condenser and evaporator as a result of the decrease in velocity of air to the evaporator. Coefficients of performance below 4 are normally not acceptable for drying applications [13] and [27].

The drying efficiency varied with moisture content in the leaves for different velocities. As the drying progressed, the moisture content was reduced, and this resulted in a decrease in drying efficiency. The relatively higher drying efficiency of 76.23 % was obtained for a moderate velocity of air at 2.39 m/s.

### 3.2 Drying Curves

The effects of drying velocities on the drying process of Amaranth leaves are shown in Figs. 5 to 11, in which drying rate curves under different drying conditions are plotted. During the drying process, air

**Table 4.** Dryer performance parameters

Drying velocity, [m/s]	$HUF$	$MER$ , [kg/h]	$SMER$ , [kg/(kWh)]	$SEC$ , [kW/kg]	$COP$	Drying efficiency, [%]
1.41	0.18	0.370	0.1512	1.27	4.23	72.12
2.39	0.17	0.375	0.1529	1.16	4.60	76.23
3.24	0.11	0.375	0.1529	1.26	4.46	74.34

velocity was kept constant, and the drying rate and drying time were continuously influenced by drying air velocity. It was experimentally confirmed that drying velocities had significant effects on the drying parameters. The drying rate curves indicated that the whole drying process occurred in the falling rate period.

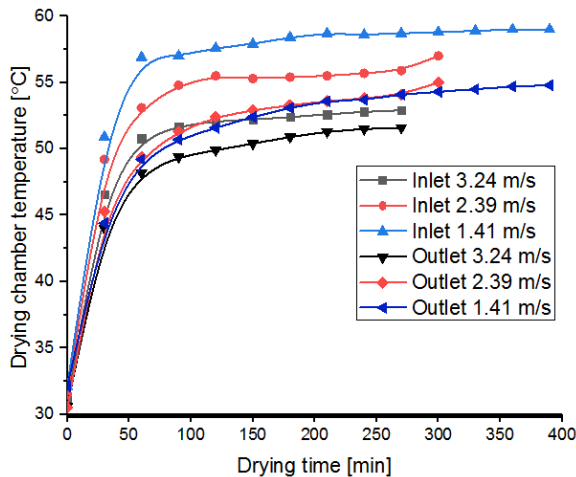


Fig. 5. Variation of drying chamber at inlet and outlet air temperature with drying time

3.2.1 Effect of Drying Temperature

Variation of inlet and exhaust temperature of the drying chamber with drying time for Amaranth leaves at different velocities is shown in Fig. 5. The temperature of drying air increased with time at the inlet and outlet of the trays and ultimately reached constant values. Initially, the temperature was low because the leaves were wet and released latent heat. As time progressed, the leaves began to dry, and the release of latent heat reduced, thereby increasing the drying air temperature inside the drying chamber. The maximum temperature attained by the air at the inlet of the trays was 59.1 °C, 57.0 °C, and 52.9 °C for the air velocities of 1.41 m/s, 2.39 m/s, and 3.24 m/s, respectively. The reason for the difference in temperature was the residence time of air in contact with the condenser surface area. As the residence time was slightly more with low velocity (1.41 m/s) of air, a higher drying temperature was observed. As leaves are to be dried in dryers using temperatures ranging from 40 °C to 60 °C, at which there will be no structural damage and nutrient losses [2], the dryer was designed to attain temperatures not exceeding 60 °C. The other reason was that when the temperature increased, the psychrometric process moved towards

the right on the chart, increasing the energy required to condense moisture at the evaporator.

The drying chamber inlet air temperature was varied during the initial stage of drying, after which the temperature was almost stable. The temperature was varied between 31.1 °C and 50 °C for the first few hours during which almost 20 % of the drying took place. It was implied that the temperature difference across the drying chamber was highest for the first few hours of operation and then decreased because the quantity of moisture removed during the second falling rate period was small. It was also inferred from the figure that the variation of air temperature across the drying chamber was significant when low air velocity was maintained. From Fig. 5, it is observed that, at any time of operation, the temperature difference was found to be 6 °C for low and high air velocity conditions at the inlet of the drying chamber whereas 4 °C temperature differences were observed from Fig. 5 at the outlet.

Since the reheat of a heat pump is constant inlet temperature decreases as the mass flow rate is increased as per  $Q = m C_p \Delta T$ .

Since the dehumidified air is recirculated, initially, because of the product moisture and thermal capacity, the temperature rises slowly to 50 °C to 60 °C. Once the product is heated, both the inlet and outlet temperatures remain constant.

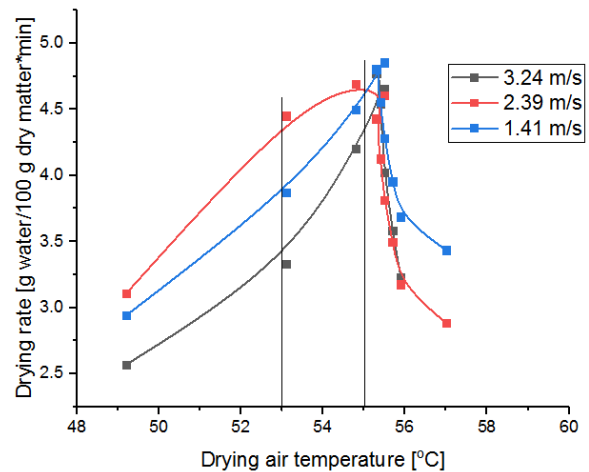


Fig. 6. Variation of drying rate against drying temperature

The experimental results showed that the drying air temperature had a significant effect on the expulsion of moisture content. As can be seen from Fig. 6, by increasing air temperature, the heat transfer rate between the heat source (drying air) and the material (Amaranth leaves) increased and led to faster moisture evaporation and shorter drying. In

the temperature range of 53 °C to 55 °C, there was a significant increment in drying rate, as depicted in Fig. 6. This range was wider for low velocities of air (1.41 m/s), which was in agreement with the results of earlier studies on drying of amaranth leaves [28], and mint leaves [10].

For leaf drying, it was better to use drying temperatures of 50 °C to 55 °C. The temperature should never exceed 60 °C. The main reason for this was because higher temperatures would destroy important nutrients in the leaves. Without these nutrients, the leaves would lose much of their dietary importance.

### 3.2.2 Effect of Air Humidity

Fig. 7 indicates the relative humidity of air at the inlet and outlet of the drying chamber. The RH values of drying air at the inlet of the drying chamber were achieved from the initial values of 57.1 %, 61 %, and 54.8 % down to 12.5 %, 14.8 %, and 17.9 % for the air velocities of 1.41 m/s, 2.39 m/s and 3.24 m/s, respectively, by the end of batch drying. The corresponding temperatures were 59.1 °C, 57 °C, and 52.9 °C, respectively. The initial high moisture content of the leaves and low temperature of drying air resulted in higher initial RH of the drying air, as seen in Fig. 7. The difference between outlet and inlet air RH was more initially due to the loss of water from the wet product.

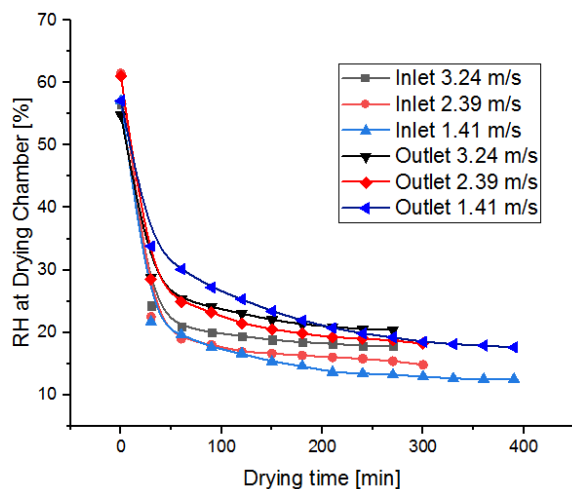


Fig. 7. Variation of RH for drying time at inlet and outlet of the drying chamber

The RH of air entering the drying chamber was maintained below 30 % with the dehumidification system of the HPATD in 30 min from the start of dryer

operation for all drying velocities chosen, as seen in Fig. 7 [22]. In the closed air circuit of HPATD, the RH continued to gradually decrease and attained an almost constant value after 60 minutes. It was evident from the figure that the reduction of RH during the study was more for the low velocity of airflow (as drying temperature was comparatively more for 1.41 m/s). This showed that the flow velocity of air had the greatest effect on the reduction of RH and had an appreciable effect on the drying rate and drying time. It was, therefore, clear that the effect of RH on drying rate was a performance controlling factor in addition to air velocity and dry bulb temperature across the bed.

It is clear from the figure that the exit RH of air was always greater than the inlet RH of air. The moisture removal capacity of air was high at the beginning of the study as the leaves were wet and, further, the RH of air decreased because of the decrease of bound moisture content from the leaves. Fig. 7 also reveals that the difference in air RH at drying chamber inlet and outlet was more during the first falling rate period. It indicates that the drying rate was faster with higher air velocity during the first falling rate period.

### 3.2.3 Effect of Air Velocity

The drying rate is a strong function of the velocity of air over the products to be dried. Variation in moisture content as a function of drying time is shown in Fig. 8. After drying, the moisture content of the Amaranth leaf samples was reduced from an initial value of 89.3 %wb to less than 10 %wb. The variation of equilibrium moisture content of the leaves occurred based on the drying air velocity. Equilibrium moisture contents of 7.51 %wb, 4.19 %wb, and 9.09 %wb were achieved for the drying air velocities of 1.41 m/s, 2.39 m/s, and 3.24 m/s, respectively. The corresponding drying times of these experimental runs to achieve the above moisture contents were 390 min, 300 min, and 270 min. The lowest final moisture content was obtained by a moderate air velocity of 2.39 m/s. From Fig. 8 and Table 5, it is seen that the drying time needed to reach the equilibrium moisture content (EMC) was shortened notably with an increase in drying air velocity from 1.41 m/s to 2.39 m/s, and 3.24 m/s due to a larger driving force for mass transfer at a higher velocity of air, which was in agreement with the results of studies on drying of dill and parsley leaves [11], studies on drying Amaranth leaves using solar dryer [28], and studies on drying of crops [14]. However, the equilibrium moisture

content of 4.19 %wb was obtained with a moderate velocity of 2.39 m/s, which was slightly higher than for 2.39 m/s. A velocity of 1.41 m/s allowed the leaves to dry reasonably well. However, when the velocity was increased to 2.39 m/s and 3.24 m/s, there was a noticeable improvement in the drying rate and drying time as the mass transfer rate was higher due to the larger driving force.

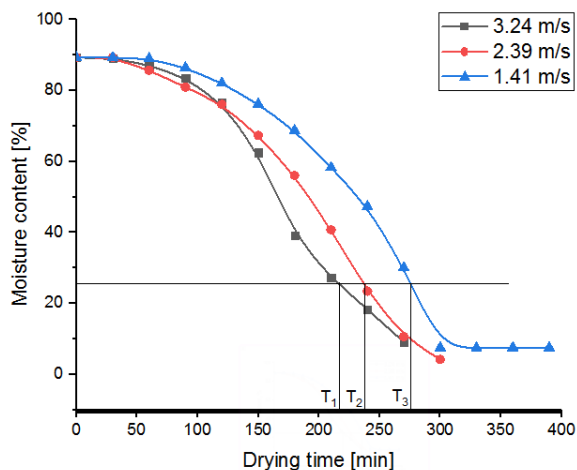


Fig. 8. Effect of air velocity on moisture content of Amaranth leaves

Table 5. Equilibrium moisture content of Amaranth leaves

Air velocity, [m/s]	Average drying air temperature, [°C]	Average relative humidity, [%]	Equilibrium moisture content, [%wb]
1.41	57.8	15.1	7.51
2.39	54.7	17.1	4.19
3.24	51.5	19.5	9.09

During the constant drying rate period, the air velocity needs to be high for the rapid initial evaporation of moisture from the surface of the leaves. Since drying progressed only with the falling drying rate period, the bound moisture gradually assumed importance. Therefore, the leaves required more energy and time to diffuse the bound moisture into the drying air and hence the amount of moisture that evaporated into the drying air decreased, as seen in Fig. 8. Thus the air velocity did not have to be high. At the same time, too low an air velocity increased the risk of non-uniform drying. According to the graph, the velocity of 1.41 m/s had no significant effect on the drying rate of Amaranth leaves.

In Fig. 8, a horizontal line was drawn to indicate constant wet basis moisture. At points where this line intersected the drying curves for each velocity,

a thin line was dropped vertically. The three vertical thin lines met the horizontal axis for a time at points labelled  $T_1$ ,  $T_2$ , and  $T_3$ .  $T_1$  was the time for the sample dried at a velocity of 3.24 m/s to reach a certain specific moisture content. It was shorter than  $T_2$ , which was the drying time at a velocity of 2.39 m/s.  $T_3$  was the time taken for drying at a velocity of 1.41 m/s, and was the longest drying time of the three. This clearly showed the impact of velocity on the drying of the Amaranth leaves for moisture removal and drying time.

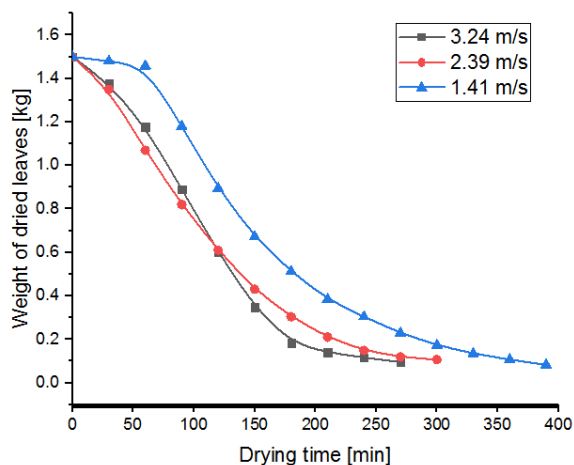


Fig. 9. Effect of air velocity on the weight of dried leaves

Fig. 9 shows the graph of the weight of the leaves during the time the drying tests were run with a curve for each velocity. It was seen that the weight of the leaves decreased faster with the air velocity of 2.39 m/s than it did for 3.24 m/s or 1.41 m/s.

### 3.2.4 Drying Rate

Fig. 10 shows the variation of drying rate versus drying time for different velocities. It was seen that the drying process took place only in the falling rate period, controlled by the mechanism of liquid diffusion. The constant rate drying period was almost absent. During the falling rate period, the drying rate decreased continuously with decreasing moisture content and increasing drying time. Usually, higher airflow velocity intensified drying rate change by the drying time. This result was in line with many earlier research findings on leaf drying [2], [4], [9], [13] and [16].

Change in air velocity had a strong influence on the evaporation of bound water from leaves and reduced drying time. Drying rates decreased as moisture content decreased. The results showed that

the experiment with a moderate velocity of air had a higher drying rate and shorter drying time. The drying time of samples decreased from 390 min to 270 min as the air velocity was increased from 1.41 m/s to 3.24 m/s. The results were consistent with the results those obtained by Pal and Khan [22] for heat-sensitive crops.

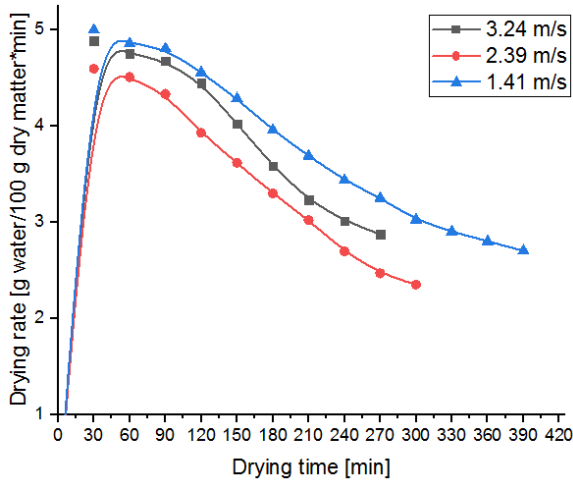


Fig. 10. Effect of air velocity on drying rate

It can be concluded that at a constant temperature and varied ambient percentage of relative humidity, the maximum possible drying rate was obtained by the moderate velocity of drying air (2.39 m/s) across the surface of the product, resulting in the rapid removal of moisture by evaporation from the product, which was because of the faster airflow along with suitable drying temperature (57 °C). It was seen from Fig. 10 that the drying rate curve showed a reducing trend for the highest velocity of 3.24 m/s when a low drying temperature of 52.9 °C was maintained. From the results, it was clearly understood that drying air velocity and drying temperature mutually influenced each other as well as the drying rate of Amaranth leaves.

### 3.2.5 Effect of Depth of Leaves in Trays

Fig. 11 shows the effect that the depth of leaves in trays had on the drying of Amaranth leaves for the moderate velocity of 2.39 m/s. As seen in the figure, the leaves placed in depths of 6 cm and 4 cm dried slowly when compared to the 2 cm depth, which was because the penetration of drying air through the leaves was relatively poor for a higher depth of leaves in the trays.  $T_1$  was the time required for 2 cm depth of leaves to reach a specific moisture content. It was noticeably shorter than the time taken to dry 4 cm

depth ( $T_2$ ) and 6 cm depth ( $T_3$ ), to the same moisture content. A thickness of 2 cm was hence found suitable to produce a considerable quantity of dried leaves from batch drying of Amaranth leaves.

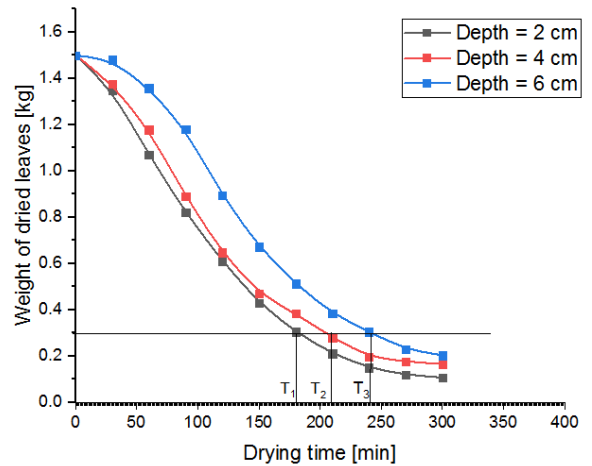


Fig. 11. Effect of depth of leaves for the velocity of 2.39 m/s

## 4 CONCLUSIONS

A drying chamber was designed, fabricated, and tested for closed-loop heat pump drying of Amaranth leaves. Experiments were conducted to examine the performance of an HPATD and determine some of the optimum operating conditions. The drying characteristics of Amaranth leaves at drying air velocities of 1.41 m/s, 2.39 m/s, and 3.24 m/s for the temperature range of 50 °C to 60 °C and relative humidity range of 20 % to 12 % were examined. The experimental results showed that

- The influence of the drying temperature was of more significance for the heat and mass transfer rate during the drying process rather than the convective effect of drying air.
- Drying rate curves indicated that the drying process took place mostly in the falling rate period.
- The velocity, temperature and RH of drying air were found to influence the rate of drying mutually.
- The experimental investigations confirmed that the moderate drying air velocity (2.39 m/s), moderate air temperature (50 °C to 60 °C), and low relative humidity (<20 %) had a significant effect on the expulsion of moisture content from Amaranth leaves.
- The results indicated that the increase in air temperature and a decrease in relative humidity

and velocity of the air improved the drying rate of amaranth leaves.

- The relatively best average values (higher *HUF*, *MER*, *SMER*, *COP*, drying efficiency, and lower *SEC*) were obtained for a moderate drying velocity of 2.39 m/s in the heat pump drying process.
- The investigation also established that a thickness of 2 cm was most suitable for batch drying of Amaranth leaves.

This dryer may be used for the effective drying of all edible leaves and other heat-sensitive crops as well.

As a result of this analysis, better drying air conditions were determined to obtain a high-quality dried product with less energy consumption.

## 5 ACKNOWLEDGMENT

The authors wish to convey their gratitude to Easwari Engineering College for readily providing the necessary infrastructure to carry out this experimental investigation.

## 6 NOMENCLATURES

$t_o$	dry bulb temperature of ambient air, [°C]
$t_1$	dry bulb temperature of drying air, [°C]
$t_2$	dry bulb temperature of drying chamber exhaust air, [°C]
$t_w$	wet bulb temperature of drying air, [°C]
$Q_{cd}$	heat delivered by the condenser, [kW]
$W_c$	power input to the compressor, [kW]
$m_a$	mass flow rate of air, [kg/s]
$C_p$	specific heat of the air, [kJ/(kgK)]
$T_C$	drying air temperature at the condenser inlet, [°C]
$T_D$	drying air temperature at drying chamber inlet, [°C]
$M$	moisture content of the sample, [%]
$w_i$	initial mass of the sample before drying, [kg]
$w_d$	final mass of the sample after drying, [kg]
$M_t$	moisture content at 't', [%wb]
$M_i$	initial moisture content, [%wb]
$M_e$	equilibrium moisture content, [%wb]
$w_d'$	weight of dry material, [kg]
$t$	drying time, [min]
$E_c$	total energy supplied in the drying process, [kW]

## 7 REFERENCES

- [1] Amaranth Greens Nutrition Facts and Health Benefits (2020). from <https://www.nutrition-and-you.com/amaranth-greens.html>, accessed on 2020-02-26.
- [2] Babu, A.K., Kumaresan, G., Antony Aroul Raj, V., Velraj, R. (2014). Review of leaf drying: Mechanism and influencing parameters, drying methods, nutrient preservation, and mathematical models. *Renewable and Sustainable Energy Reviews*, vol. 90, p. 536-556, DOI:10.1016/j.rser.2018.04.002.
- [3] Guohua Chen, Arun S. Mujumdar. (2006). Drying of herbal medicines and tea. *Handbook of Industrial Drying*. Taylor & Francis Group, p. 635-646, DOI:10.1201/9781420017618.
- [4] Patel, K.K., Kar, A. (2012). Heat pump assisted drying of agricultural produce-An overview. *Journal of Food Science Technology*, vol. 49, no. 2, p. 142-160, DOI:10.1007/s13197-011-0334-z.
- [5] Goh, L.J., Othman, M.Y., Mat, S., Ruslan, H., Sopian, K. (2011). Review of heat pump systems for drying application. *Renewable and Sustainable Energy Reviews*, vol. 15, no. 9, p. 4788-4796, DOI:10.1016/j.rser.2011.07.072.
- [6] Benedičič, J. (2019). An analysis of the process of drying fresh bales. *Tehnički vjesnik - Technical Gazette*, vol. 26, no. 6, p. 1714-1719, DOI:10.17559/TV-20190704175850.
- [7] Çerçi, K.N. Süfer, O., Söyler, M., Hürdoğan, E., Özalp, C. (2018). Thin layer drying of Zucchini in solar dryer located in Osmaniye region. *Tehnicki Glasnik - Technical Journal*, vol. 12, no. 2, p. 79-85, DOI:10.31803/tg-20180126094515.
- [8] Aktaş, M., Khanlari, A., Aktekel, B., Amini, A. (2017). Analysis of a new drying chamber for heat pump mint leaves dryer. *International Journal of Hydrogen Energy*, vol. 42, no. 28, p. 18034-18044, DOI:10.1016/j.ijhydene.2017.03.007.
- [9] Premi, M., Sharma, H., Upadhyay, A. (2012). Effect of air velocity and temperature on the drying kinetics of drumsticks leaves (*Moringa Olefera*). *International Journal of Food Engineering*, vol. 8, no. 4, p. 1556-3758, DOI:10.1515/1556-3758.1986.
- [10] Kumar, A., Kumar, V., Khan, K., Kumar, A. (2017). Experimental Investigation on Drying of Mint Leaves (*M. pulegium*) in Solar Tunnel Dryer. *International Journal Pure & Applied Bioscience*, vol. 5, no. 2, p. 682-689, DOI:10.18782/2320-7051.2498.
- [11] Doymaz, İ., Tugrul, N. Pala, M. (2006). Drying characteristics of dill and parsley leaves. *Journal of Food Engineering*, vol. 77, no. 3, p. 559-565, DOI:10.1016/j.jfoodeng.2005.06.070.
- [12] Rayaguru, K., Routray, W. (2010). Effect of drying conditions on drying kinetics and quality of aromatic Pandanus amaryllifolius leaves. *Journal of Food Science and Technology*, vol. 47, no. 6, p. 668-673, DOI:10.1007/s13197-010-0114-1.
- [13] Hossain, M.A., Gottschalk, K., Hassan, M.S. (2013). Mathematical model for a heat pump dryer for aromatic plant. *Procedia Engineering*, vol. 56, p. 510-520, DOI:10.1016/j.proeng.2013.03.154.
- [14] Fatouh, M., Metwally, M.N., Helali, A.B., Shedid, M.H. (2006). Herbs drying using a heat pump dryer. *Energy Conversion and Management*, vol. 47, no. 15-16, p. 2629-2643, DOI:10.1016/j.enconman.2005.10.022.
- [15] Babu, A.K., Kumaresan, G., Antony Aroul Raj, V., Velraj, R. (2019). CFD studies on different configurations of drying chamber for thin-layer drying of leaves. *Energy Sources, Part A: Recovery, Utilization, and Environmental Effects*, p. 113, DOI:10.1080/15567036.2019.1607935.
- [16] Ahn, J.Y., Kill, D.Y., Kong, C., Kim, B.G. (2014). Comparison of oven-drying methods for determination of moisture content

- in feed ingredients. *Asian-Australasian Journal of Animal Sciences*, vol. 27, no. 11, p. 1615-1622, DOI:10.5713/ajas.2014.14305.
- [17] Negi, P.S., Roy, S.K. (2001). Effect of drying conditions on quality of green leaves during long term storage. *Food Research International*, vol. 34, no. 4, p. 283-287, DOI:10.1016/S0963-9969(00)00165-4.
- [18] Sagrin, M.S., Chong, G.H. (2013). Effects of drying temperature on the chemical and physical properties of Musa acuminate Colla (AAA Group) leaves. *Industrial Crops and Products*, vol. 45, p. 430-434, DOI:10.1016/j.indcrop.2012.12.036.
- [19] Growing and Processing of Moringa Leaves (2019). from <http://www.moringanews.org/documents/moringawebEN.pdf>, accessed on 2019-10-14.
- [20] Shaw, M., Meda, V., Tabil Jr., L., Opoku, A. (2007). Drying and color characteristics of Coriander foliage using convective thin-layer and microwave drying. *Journal of Microwave Power & Electromagnetic Energy*, vol. 41, no. 2, p. 41-2-56-65, DOI:10.1080/08327823.2006.11688559.
- [21] Chakraverthy, A., Singh, R.P. (2014). *Postharvest Technology and Food Process Engineering*. Taylor & Francis Group, CRC Press, Boca Raton.
- [22] Pal, U.S., Khan, M.K. (2010). Performance evaluation of heat pump dryer. *Journal of Food Science and Technology*, vol. 47, no. 2, p. 230-234, DOI:10.1007/s13197-010-0031-3.
- [23] Yamankaradeniz, N., Sokmen, F., K., Coskun, S., Kaynakli, O., Pastakkaya, B. (2016). Performance analysis of a re-circulating heat pump dryer. *Thermal Science*, vol. 20, no. 1, p. 267-277, DOI:10.2298/TSCI130426069Y.
- [24] Tunçkal, C., Coskun, S., Doymaz, İ., Ergun, E. (2018). Determination of sliced pineapple drying characteristics in a closed loop heat pump assisted drying system. *International Journal of Renewable Energy Development*, vol. 7, no. 1, p. 35-41, DOI:10.14710/ijred.7.1.35-41.
- [25] Baysal, T., Ozbalta, N., Gokbulut, S., Capar, B., Tastan, O., Gurlek, G.. (2015). Investigation of effects of various drying methods on the quality characteristics of apple slices and energy efficiency. *Journal of Thermal Science and Technology*, vol. 35, no. 1, p. 135-144.
- [26] Simpson, W.T. (1997). *Effect of air velocity on drying rate of single eastern white pine boards*. Res. Note FPL-RN-266. U.S. Department of Agriculture, Forest Service, Forest Products Laboratory, Madison, DOI:10.2737/fpl-rn-266.
- [27] Minea, V. (2011). *Industrial drying heat pumps. Refrigeration: Theory, Technology and Applications*. Nova Science Publishers, Inc., New York.
- [28] Singh, P., Singh, S., Singh, B.R., Singh, J., Singh, S.K. (2014). The drying characteristic of amaranth leaves under greenhouse type solar dryer and open sun. *Greener Journal of Agricultural Sciences*, vol. 4, no. 6, p. 281-287, DOI:10.15580/GJAS.2014.6.040314174.

# Pitch Stability Analysis for Mechanical-Hydraulic-Structural-Fluid Coupling System of High-Lift Hoist Vertical Shiplift

Yang Zhang<sup>1,2</sup> – Duanwei Shi<sup>1,2,\*</sup> – Tong Xiao<sup>2</sup> – Ji Zhou<sup>2</sup> – Xionghao Cheng<sup>2</sup>

<sup>1</sup>Wuhan University, Key Laboratory of Hydraulic Machinery Transients, China

<sup>2</sup>Wuhan University, School of Power and Mechanical Engineering, China

*Pitch stability of the high-lift wire rope hoist vertical shiplift under dynamic hydraulic levelling has always been an issue of concern. It not only affects working efficiency but also brings significant challenges to operational safety. A new mechanical-hydraulic-structural-fluid (MHSF) coupling dynamics model and a developed semi-analytical method are presented for stable property analysis. The models of the hydraulic levelling subsystem, shallow water sloshing subsystem, the main hoist mechanical subsystem, and the shiplift chamber structure subsystem are built using a closed-loop transfer function, multi-modal theory, and an second-type Lagrangian equation, respectively. Then, a core twenty-one order state matrix of the MHSF coupling system is established using the state-space method. Subsequently, the Lyapunov motion stability theory and Eigen-analysis method are used in combination to judge the pitch stability and analyse the characteristics of the subsystems. Taking four typical high-lift hoist vertical shiplifts as examples, the rationality of the proposed model and method is validated. The results indicate that although the pitch stability safety factor under hydraulic dynamic levelling is reduced by about 15 % to 44 % with respect to hydraulic static levelling, hydraulic dynamic levelling still can meet stability requirements. Furthermore, for the designed 200 m level hoist vertical shiplift, the preliminary design parameters can ensure the pitch stability safety factor under dynamic hydraulic levelling of not less than 1.1. The element most prone to instability is the shallow water sloshing subsystem; increasing the synchronous shaft stiffness or the water boundary layer damping ratio can effectively enhance the pitch stability.*

**Keywords:** shiplift, pitch stability, hydraulic levelling, Eigen-analysis, dynamics

## Highlights

- A new mechanical-hydraulic-structural-fluid (MHSF) coupling dynamics model of high-lift hoist vertical shiplift has been established.
- A developed semi-analytical method has been presented to analyse the pitch stability characteristics.
- Pitch stability under hydraulic dynamic levelling is reduced by 15 % to 44 % with respect to hydraulic static levelling, but hydraulic dynamic levelling will not cause instability.
- For the designed 200 m level shiplift, improving the synchronous shaft stiffness by 30 % can enhance the pitch stability by about 6.2 %; doubling the water boundary layer damping ratio can raise the pitch stability about 20.57 %.

## 0 INTRODUCTION

As a core component in a large hydropower station, the high-lift hoist vertical shiplift is pre-developed in China. It uses cables to raise the ship to overcome the water level difference between upstream and downstream. Since the lift height of the 200 m level hoist vertical shiplift (abbreviated as 200 m level shiplift) is nearly double that of the Three Gorges shiplift, the pitch stability problem becomes more complicated. For the vast majority of hoist vertical shiplifts, a hydraulic levelling subsystem has been set up, for levelling the shiplift chamber and balancing the tension of cables. However, once the hydraulic levelling subsystem is started during operation (dynamic hydraulic levelling), it will form a complex mechanical-hydraulic-structural-fluid (MHSF) coupling system. Its dynamic stability and the ability to resist the overturning are not apparent,

so only starting the hydraulic levelling subsystem after stopping the shiplift (hydraulic static levelling) is allowed at present [1] and [2]. In order to ensure operational safety and avoid unnecessary downtime, pitch stability under dynamic hydraulic levelling should be studied in depth.

Previous research studies on the shiplift system model are incomplete. The ship-water-chamber coupling motion equations are established to analyse the time response [3]. However, the primary hoist subsystem is ignored, which plays an essential role in ensuring pitch stability. Liao [4] and Cheng et al. [5] built a coupling dynamics model of main hoist subsystem, shiplift chamber, and sloshing, but neglected the torque counterweight in the main hoist subsystem; the latter is an essential part in the fully balanced quality system. A nine-degree-of-freedom (DOF) model of the primary hoist subsystem (including hoist, pulley, wire rope,

torque counterweight, gravity counterweight, and synchronous shaft), shiplift chamber, and shallow water sloshing was developed by Zhang et al. [6]. The pitch stability problem under hydraulic static levelling can be solved very well, but the hydraulic levelling subsystem remains ignored; it is important to balance and equalize the tension between the wire ropes and adjust the level of shiplift chamber. In the newly proposed MHSF coupling dynamics model, the main hoist subsystem, shiplift chamber subsystem, hydraulic levelling subsystem, and shallow water sloshing subsystem will be considered completely to analyse the pitch stability under hydraulic dynamic levelling. This is a critical issue for current shiplift designers and researchers.

For the relatively simple mechanical [7] and [8] and mechanical-fluid [9] system, the Lyapunov function is commonly used to judge the stability. However, it is difficult to construct the Lyapunov function directly from the complex shiplift system. The convergence of the time-domain response is focused on analysing the complex hydraulic-mechanical-electrical-structural system [10]. However, for the MHSF coupling system with a large difference in response frequency, it is too easy to form ill-conditioned equations. The hydraulic levelling subsystem is treated as a first-order system, and the tension equalization characteristics and dynamic system responses are analysed [11]. It is a good attempt, but the simplification of the hydraulic levelling subsystem and the lack of shallow water sloshing subsystems are inappropriate for pitch stability analysis. The Routh-Hurwitz theory [12] and [13] and Lyapunov motion stability theory [14] and [15] have been proved to rate the stability effectively. However, its analysis of the intrinsic connection of the coupling system is powerless. Eigen-analysis and the state-space method are adopted to investigate the stability of the hydraulic-mechanical-electrical coupling mechanism of a hydropower plant [16] to [19].

In the present study, a new MHSF coupling dynamics model for high-lift hoist vertical shiplift will be established. Furthermore, a developed semi-analytical method integrating the Lyapunov motion stability theory and Eigen-analysis will be proposed to judge the pitch stability and analyse the internal connection of the coupling system under dynamic hydraulic levelling. Four typical high-lift hoist vertical shiplifts will be taken as examples to validate the proposed model and method. The subsystem stability priority will be interpreted. In addition, the influence of lift height, synchronous shaft stiffness

and subsystem damping ratio on the pitch stability will be researched in detail.

## 1 METHODS

In the process of ascension, the shiplift chamber suspended by cable is inevitably pitched due to the manufacturing error of the hoist diameter, the wire rope diameter and elastic modulus [20]. As shown in Fig. 1, the shiplift chamber is subjected to pitch motion during operation, and the clamping equipment, the safety brake, and the working brake have been released.

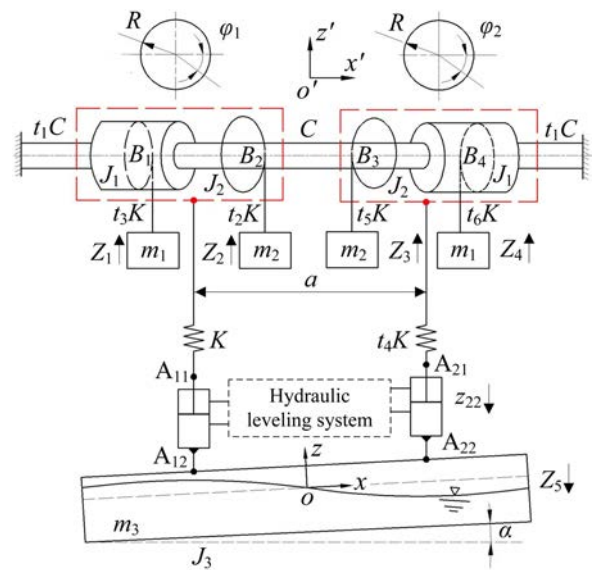


Fig. 1. A 10DOF ( $\varphi_1, \varphi_2, \alpha, Z_1, Z_2, Z_3, Z_4, Z_5, z_{22}, \beta_1$ ) MHSF coupling dynamics model of high-lift hoist vertical shiplift

A new MHSF coupling system is established under the earth-fixed coordinate system ( $o'x'z'$ ). In order to illustrate the mathematical model, the coupling system is decoupled as the main hoist mechanical subsystem, hydraulic levelling subsystem, rigid shiplift chamber structure subsystem and shallow water sloshing subsystem. The main hoist mechanical subsystem is a mechanical device that suspends the chamber and drives it up and down; it mainly consists of the hoist lift mechanism ( $B_1, B_2, B_3, B_4$ ), synchronous shaft ( $C, t_1C$ ), counterweight ( $m_1, m_2$ ) and wire rope ( $K, t_4K, t_2K, t_3K, t_5K, t_6K$ ).

### 1.1 Shallow Water Sloshing Subsystem Model

The shiplift chamber is a typical rectangular water container with low filling depth ratio ( $H/L < 0.05$ ).

Since the variation range of water along the length distribution is much larger than that along the width distribution, a two-dimensional rigid shiplift chamber with a unitary width is adopted [21], as shown in Fig. 2.  $oxz$  is the shiplift chamber-fixed coordinate system located at the centre of the mean free surface ( $\Sigma_0$ ).

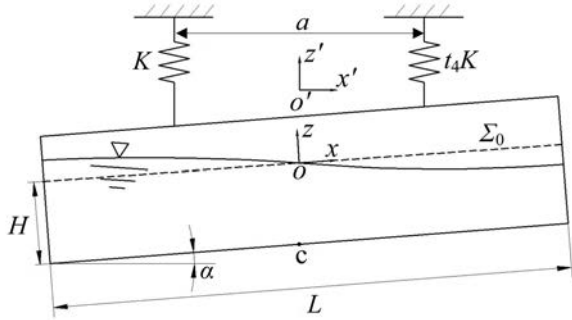


Fig. 2. Shallow water sloshing in the shiplift chamber under pitch motion

Previous research [22] has shown that the peak hydrodynamic moment reaches maximum value under pure pitch motion instead of coupled vertical and pitch motions. To ensure the safety, pure pitch motion (more dangerous) will be further investigated. According to the studies of [6] and [23], the modal system of shallow water sloshing and hydrodynamic moment can be written as:

$$\ddot{\beta}_1 + 2\xi_w \omega_1 \dot{\beta}_1 + \omega_1^2 \beta_1 = \frac{4Hg}{L} \alpha + \frac{4H^2}{L} \ddot{\alpha}, \quad (1)$$

$$M = -\frac{3}{2500} \rho BHL^3 \ddot{\alpha} + \frac{2L}{\pi^4 H^2} \rho BHL^3 \ddot{\beta}_1. \quad (2)$$

### 1.2 Hydraulic Levelling Subsystem Model

The hydraulic levelling subsystem consists of levelling hydraulic cylinders and a hydraulic control system. If the situation of Fig. 1 appears, the control strategy is keeping the state of  $A_{11}$  point unchanged, and controlling the  $A_{21}$  point to approach  $A_{11}$  through the hydraulic system. The modelling of the hydraulic levelling subsystem mainly includes the proportional

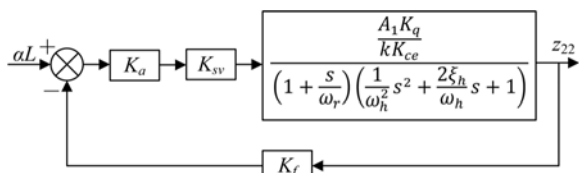


Fig. 3. Closed-loop transfer function block diagram of hydraulic levelling system

amplifier, the proportional speed regulating valve, valve controlled asymmetric hydraulic cylinder, and shiplift chamber level sensor. Because of the working frequency of proportional amplifiers, the proportional speed regulating valve and shiplift chamber level sensor is much higher than that of the hydraulic cylinder, so these are linearized into proportional links.

As shown in Fig. 3, according to the linear flow equation, the flow continuity equation and force balance equation [24], the transfer function of the valve controlled asymmetric hydraulic cylinder  $G(s)$  can be derived as:

$$G(s) = \frac{A_1 K_q}{k K_{ce}} \left( 1 + \frac{s}{\omega_r} \right) \left( \frac{s^2}{\omega_h^2} + \frac{2\xi_h}{\omega_h} s + 1 \right), \quad (3a)$$

$$\omega_h = \sqrt{\left[ \frac{2(1+n^2)\beta_e A_1^2}{M_t V_t} + \frac{k}{M_t} \right]}, \quad (3b)$$

$$\xi_h = \frac{K_{ce}}{2A_1} \sqrt{\frac{2(1+n^2)\beta_e M_t}{V_t}} \left[ 1 + \frac{kV_t}{2(1+n^2)\beta_e A_1^2} \right]^{\frac{3}{2}}, \quad (3c)$$

$$\omega_r = \frac{K_{ce}}{A_1^2} \left[ \frac{1}{k} + \frac{V_t}{2(1+n^2)\beta_e A_1^2} \right], \quad (3d)$$

here  $n=A_2/A_1$ ,  $K_{ce}=K_c+C_t$  and  $k=t_4K$ .

According to Fig. 3, the closed-loop transfer function of the hydraulic levelling subsystem  $G_B(s)$  is as follows:

$$G_B(s) = \frac{A_1 K_q K_a K_{sv} \omega_r \omega_h^2}{k K_{ce}} \left[ \frac{s^3 + (2\xi_h \omega_h + \omega_r) s^2 + (\omega_h^2 + 2\xi_h \omega_r \omega_h) s + (1 + \frac{A_1 K_q}{k K_{ce}} K_a K_{sv} K_f) \omega_r \omega_h^2}{s^3 + (2\xi_h \omega_h + \omega_r) s^2 + (\omega_h^2 + 2\xi_h \omega_r \omega_h) s + (1 + \frac{A_1 K_q}{k K_{ce}} K_a K_{sv} K_f) \omega_r \omega_h^2} \right]. \quad (4)$$

The input of the hydraulic levelling system is the displacement deviation of the shiplift chamber ( $\alpha L$ ), and the output is the piston displacement ( $z_{22}$ ). Thus, the dynamic model can be derived based on Eq. (4).

$$\ddot{z}_{22} + (2\xi_h \omega_h + \omega_r) \dot{z}_{22} + (\omega_h^2 + 2\xi_h \omega_r \omega_h) z_{22} + \left( 1 + \frac{A_1 K_q}{k K_{ce}} K_a K_{sv} K_f \right) \omega_r \omega_h^2 z_{22} = \dots \quad (5)$$

$$-\frac{A_1 K_g}{k K_{ce}} K_a K_{sv} \omega_r \omega_h^2 L \alpha = 0. \quad \text{cont. (5)}$$

### 1.3 Main Hoist Mechanical Subsystem Model

The kinetic energy and potential energy of the main hoist mechanical and shiplift chamber structure subsystem can be defined as:

$$T = \frac{1}{2} J_1 (\dot{\phi}_1^2 + \dot{\phi}_2^2) + \frac{1}{2} J_2 (\dot{\phi}_1^2 + \dot{\phi}_2^2) + \frac{1}{2} J_3 \dot{\alpha}^2 + \frac{1}{2} m_1 \dot{Z}_1^2 + \frac{1}{2} m_2 \dot{Z}_2^2 + \frac{1}{2} m_2 \dot{Z}_3^2 + \frac{1}{2} m_1 \dot{Z}_4^2 + \frac{1}{2} m_3 \dot{Z}_5^2, \quad (6)$$

$$V = \frac{1}{2} K \left( R\phi_1 - Z_5 - \frac{1}{2} \alpha \right)^2 + \frac{1}{2} t_4 K \left( R\phi_2 - z_{22} - Z_5 + \frac{1}{2} \alpha \right)^2 + \frac{1}{2} t_3 K (R\phi_1 + Z_1)^2 + \frac{1}{2} t_2 K (R\phi_1 + Z_2)^2 + \frac{1}{2} t_5 K (R\phi_2 + Z_3)^2 + \frac{1}{2} t_6 K (R\phi_2 + Z_4)^2 + \frac{1}{2} C (\phi_1 - \phi_2)^2 + \frac{1}{2} t_1 C (\phi_1^2 + \phi_2^2). \quad (7)$$

Considering the torsional vibration damping ratio  $\xi_j$  and wire rope damping ratio  $\xi_g$ , the dynamic model of the primary hoist mechanical subsystem can be derived using the second type Lagrangian equation.

$$\ddot{\phi}_1 + 2\xi_j \sqrt{\frac{(C + t_2 KR^2 + t_3 KR^2 + t_1 C + KR^2)}{(J_1 + J_2)}} \dot{\phi}_1 + \frac{(C + t_2 KR^2 + t_3 KR^2 + t_1 C + KR^2)}{(J_1 + J_2)} \phi_1 - \frac{KR}{(J_1 + J_2)} Z_5 - \frac{aKR}{2(J_1 + J_2)} \alpha + \frac{t_3 KR}{(J_1 + J_2)} Z_1 + \frac{t_2 KR}{(J_1 + J_2)} Z_2 - \frac{C}{(J_1 + J_2)} \phi_2 = 0, \quad (8)$$

$$\ddot{\phi}_2 + 2\xi_j \sqrt{\frac{(t_6 KR^2 + t_5 KR^2 + C + t_1 C + t_4 KR^2)}{(J_1 + J_2)}} \dot{\phi}_2 + \frac{(t_6 KR^2 + t_5 KR^2 + C + t_1 C + t_4 KR^2)}{(J_1 + J_2)} \phi_2 - \frac{t_4 KR}{(J_1 + J_2)} z_{22} - \frac{t_4 KR}{(J_1 + J_2)} Z_5 + \frac{t_4 aKR}{2(J_1 + J_2)} \alpha + \frac{t_5 KR}{(J_1 + J_2)} Z_3 + \frac{t_6 KR}{(J_1 + J_2)} Z_4 - \frac{C}{(J_1 + J_2)} \phi_1 = 0, \quad (9)$$

$$\ddot{Z}_1 + 2\xi_g \sqrt{\frac{t_3 K}{m_1}} \dot{Z}_1 + \frac{t_3 K}{m_1} Z_1 + \frac{t_3 KR}{m_1} \phi_1 = 0, \quad (10)$$

$$\ddot{Z}_2 + 2\xi_g \sqrt{\frac{t_2 K}{m_2}} \dot{Z}_2 + \frac{t_2 K}{m_2} Z_2 + \frac{t_2 KR}{m_2} \phi_1 = 0, \quad (11)$$

$$\ddot{Z}_3 + 2\xi_g \sqrt{\frac{t_5 K}{m_2}} \dot{Z}_3 + \frac{t_5 K}{m_2} Z_3 + \frac{t_5 KR}{m_2} \phi_2 = 0, \quad (12)$$

$$\ddot{Z}_4 + 2\xi_g \sqrt{\frac{t_6 K}{m_1}} \dot{Z}_4 + \frac{t_6 K}{m_1} Z_4 + \frac{t_6 KR}{m_1} \phi_2 = 0. \quad (13)$$

### 1.4 Shiplift Chamber Structure Subsystem Model

The rigid shiplift chamber is subjected to pitch and vertical motions during operation. Considering the pitch motion damping ratio  $\xi_p$  and vertical motion damping ratio  $\xi_v$ , the model of the shiplift chamber structure subsystem can also be derived by using the second type Lagrangian equation.

$$\ddot{Z}_5 + 2\xi_v \sqrt{\frac{(K + t_4 K)}{m_3}} \dot{Z}_5 + \frac{(K + t_4 K)}{m_3} Z_5 - \frac{KR}{m_3} \phi_1 + \frac{\left(\frac{Ka}{2} - \frac{t_4 Ka}{2}\right)}{m_3} \alpha - \frac{t_4 KR}{m_3} \phi_2 + \frac{t_4 K}{m_3} z_{22} = 0, \quad (14)$$

$$\ddot{\alpha} + 2\xi_p \sqrt{\frac{\left(\frac{t_4 Ka^2}{4} + \frac{Ka^2}{4}\right)}{J_3}} \dot{\alpha} + \frac{\left(\frac{t_4 Ka^2}{4} + \frac{Ka^2}{4}\right)}{J_3} \alpha - \frac{KR a}{2J_3} \phi_1 + \frac{t_4 KR a}{2J_3} \phi_2 - \frac{t_4 Ka}{2J_3} z_{22} + \frac{\left(\frac{Ka}{2} - \frac{t_4 Ka}{2}\right)}{J_3} Z_5 = \frac{M}{J_3}. \quad (15)$$

### 1.5 Eigen-analysis of MHSF Coupling System

With the MHSF coupling system, it is rather difficult to judge the stability by directly solving the time domain signal. The state-space method is adopted to form a core twenty-one order state matrix. Substituting Eq. (2) into Eq. (15), the Eq. (1), Eq. (5) and Eq. (8) to Eq. (15) can be further organized as follows:

$$\ddot{\alpha} + C_{1,1} \dot{\alpha} + C_{1,2} \alpha - C_{1,3} \phi_1 + C_{1,4} \phi_2 - C_{1,5} z_{22} + C_{1,6} Z_5 + C_{1,7} \beta_1 + C_{1,8} \beta_1 = 0, \quad (16a)$$

$$\ddot{\phi}_1 + C_{2,1} \dot{\phi}_1 + C_{2,2} \phi_1 - C_{2,3} Z_5 - C_{2,4} \alpha + C_{2,5} Z_1 + C_{2,6} Z_2 - C_{2,7} \phi_2 = 0, \quad (16b)$$

$$\ddot{\varphi}_2 + C_{3,1}\dot{\varphi}_2 + C_{3,2}\varphi_2 - C_{3,3}z_{22} - C_{3,4}Z_5 + C_{3,5}\alpha + C_{3,6}Z_3 + C_{3,7}Z_4 - C_{3,8}\varphi_1 = 0, \tag{16c}$$

$$\ddot{Z}_1 + C_{4,1}\dot{Z}_1 + C_{4,2}Z_1 + C_{4,3}\varphi_1 = 0, \tag{16d}$$

$$\ddot{Z}_2 + C_{5,1}Z_2 + C_{5,2}Z_2 + C_{5,3}\varphi_1 = 0, \tag{16e}$$

$$\ddot{Z}_3 + C_{6,1}\dot{Z}_3 + C_{6,2}Z_3 + C_{6,3}\varphi_2 = 0, \tag{16f}$$

$$\ddot{Z}_4 + C_{7,1}\dot{Z}_4 + C_{7,2}Z_4 + C_{7,3}\varphi_2 = 0, \tag{16g}$$

$$\ddot{Z}_5 + C_{8,1}\dot{Z}_5 + C_{8,2}Z_5 - C_{8,3}\varphi_1 + C_{8,4}\alpha - C_{8,5}\varphi_2 + C_{8,6}z_{22} = 0, \tag{16h}$$

$$\ddot{\beta}_1 + C_{9,1}\dot{\beta}_1 + C_{9,2}\beta_1 + C_{9,3}\alpha + C_{9,4}\dot{\alpha} - C_{9,5}\varphi_1 + C_{9,6}\varphi_2 - C_{9,7}z_{22} + C_{9,8}Z_5 = 0, \tag{16i}$$

$$\ddot{z}_{22} + C_{10,1}\ddot{z}_{22} + C_{10,2}\dot{z}_{22} + C_{10,3}z_{22} - C_{10,4}\alpha = 0, \tag{16j}$$

here  $C_{i,j}$  correspond to coefficient terms in Eq. (15), Eq. (8) to Eq. (14), Eq. (1) and Eq. (5). In order to judge the pitch stability, the Eq. (16a) to (16i) should be reduced to first-order. The state vectors are selected as:  $x_1 = \dot{\varphi}_1$ ,  $x_2 = \varphi_1$ ,  $x_3 = \dot{\varphi}_2$ ,  $x_4 = \varphi_2$ ,  $x_5 = \dot{\alpha}$ ,  $x_6 = \alpha$ ,  $x_7 = \dot{Z}_1$ ,  $x_8 = Z_1$ ,  $x_9 = \dot{Z}_2$ ,  $x_{10} = Z_2$ ,  $x_{11} = \dot{Z}_3$ ,  $x_{12} = Z_3$ ,  $x_{13} = \dot{Z}_3$ ,  $x_{14} = Z_4$ ,  $x_{15} = \dot{Z}_5$ ,  $x_{16} = Z_5$ ,  $x_{17} = \dot{\beta}_1$ ,  $x_{18} = \beta_1$ ,  $x_{19} = \dot{z}_{22}$ ,  $x_{20} = z_{22}$  and  $x_{21} = z_{22}$ .

$$\mathbf{x}^T = \begin{bmatrix} x_1 \\ \vdots \\ x_{21} \end{bmatrix}. \tag{17}$$

Combining Eq. (17) and Eq. (16a) to (16i), the state equations of the coupling system can be described by:

$$\frac{d\mathbf{x}}{dt} = \begin{bmatrix} \dot{x}_1 \\ \vdots \\ \dot{x}_{21} \end{bmatrix} = \mathbf{A} \begin{bmatrix} x_1 \\ \vdots \\ x_{21} \end{bmatrix} = \mathbf{A}\mathbf{x}. \tag{18}$$

This is the central concept of this paper because the pitch stability can be analysed by investigating the eigenvalues of  $\mathbf{A}$ . The eigenvalue equation of matrix  $\mathbf{A}$  can be derived as follows:

$$\sum_{i=0}^{21} b_i \lambda^{21-i} = 0. \tag{19}$$

Solutions of Eq. (19) are  $\lambda_i = \text{Re}_i + \text{Im}_i j$  ( $i=0, 1, \dots, 21$ ), which are not only the eigenvalues of matrix  $\mathbf{A}$  but also the main indicators of pitch stability. According to the Lyapunov motion stability theory, the necessary and sufficient condition for the zero-solution stability of a linear system with constant coefficients is that the real parts of all eigenvalues are negative ( $\text{Re}_i < 0$ ).

Since the eigenvalues  $\lambda_i$  are not needed to be expressed analytically, numerical calculation with Mathematica software can be adopted to judge the pitch stability. The algorithm flow is shown as:

- (1) For a particular shiplift, substituting structural parameters except  $a$  into matrix  $\mathbf{A}$ , and let  $a = 0.01i'$  ( $i'=0, 1, 2, \dots$ ).
- (2) For each starting from 0, substituting into the matrix  $\mathbf{A}$  to find its eigenvalues. If all the eigenvalues have a negative real part, stopping the cycle and output the critical value of  $a = a_{cd}$ , where output  $a_{cd}$  is the critical distance of suspension points under hydraulic dynamic levelling, which is a key evaluation indicator of the pitch stability. Otherwise, the loop continues until  $a_{cd}$  is found.

## 2 RESULTS AND DISCUSSION

### 2.1 Validation

In order to illustrate the rationality of the presented model and calculation method, four typical high-lift hoist vertical shiplifts are adopted to be analysed, as shown in Table 1, where  $a_{cs}$  is calculated by [6],  $n_d = a/a_{cd}$  and  $n_s = a/a_{cs}$ . The decrease of  $a_{cd}$  and  $a_{cs}$  indicates pitch stability improvement.

Comparing the  $a_{cd}$  and  $a_{cs}$  in Table 1, it can be seen that the dynamic hydraulic levelling is enabled to significantly reduce the pitch stability (from 15 % to 44 %). The main reason is that the hydraulic levelling subsystem is coupled in series to the original mechanical-structural-fluid system, reducing the system's overall stiffness. The calculated  $a_{cd}$  is the key parameter that has long limited application of hydraulic dynamic levelling in shiplift technical practice.

**Table 1.** The distance of suspension points for four typical high-lift hoist vertical shiplifts

Shiplift name	$h$ [m]	Current status	$a_d$ [m]	$a_{cd}$ [m]	$a_{cs}$ [m]	$n_d$	$n_s$	$(n_s - n_d) / n_s$ [%]
GeHeyan shiplift (the first step)	40	In use	23.6	13	8.6	1.8	2.7	34
GeHeyan shiplift (the second step)	82	In use	24.0	19.6	11.6	1.2	2.1	41
GouPitan shiplift (the second step)	127	In use	36.2	33.3	18.5	1.1	2.0	44
200 m level vertical shiplift	200	Design stage	62	56.4	47.9	1.1	1.3	15

Analysing  $a_d$  and  $a_{cd}$  in Table 1,  $a_d$  can guarantee that the shiplift is in stable working condition under hydraulic dynamic leveling. Especially for the 200 m level shiplift, the design parameters can ensure that even if the hydraulic levelling subsystem is started at the most dangerous position, the shiplift chamber is still stable with  $n_d=1.1$ .

## 2.2 Subsystem Stability Priority

In order to study the subsystem stability priority under hydraulic dynamic levelling, the vibration frequency change of each subsystem in the process of gradually reducing  $a$  is explored by taking the 200 m level shiplift as an engineering example.

**Table 2.** Eigenvalues of 200 m level shiplift coupling system under different distance of suspension points

Subsystem	Distance of suspension points		
	62	56.4	13
Hydraulic levelling	$-5.33 \pm 161.80j$	$-5.33 \pm 161.80j$	$-5.33 \pm 161.80j$
Hoists	$-3.99 \pm 46.60j$	$-3.99 \pm 46.59j$	$-4.00 \pm 46.56j$
	$-3.93 \pm 44.59j$	$-3.93 \pm 44.59j$	$-3.93 \pm 44.59j$
Suspended wire ropes	$-0.17 \pm 16.24j$	$-0.17 \pm 16.24j$	$-0.17 \pm 16.24j$
	$-0.17 \pm 16.23j$	$-0.17 \pm 16.23j$	$-0.17 \pm 16.23j$
	$-0.47 \pm 9.25j$	$-0.46 \pm 8.93j$	$-0.51 \pm 7.93j$
	$-0.38 \pm 7.56j$	$-0.38 \pm 7.56j$	$-0.38 \pm 7.56j$
Chamber pitch motion	$-0.58 \pm 5.32j$	$-0.54 \pm 4.98j$	$-0.47 \pm 0.34j$
Chamber vertical motion	$-0.23 \pm 3.39j$	$-0.23 \pm 3.39j$	$-0.23 \pm 3.39j$
Shallow water sloshing	$-1.33 \times 10^{-5} \pm 0.22j$	$-8.18 \times 10^{-5} \pm 0.22j$	$0.33 \pm 0.37j$

Here,  $j$  is an imaginary number. The negative real part of eigenvalue indicates that the subsystem is stable, otherwise unstable. The larger the absolute value of the real part, the higher the stability and instability margin. The absolute value of the imaginary part represents the vibration frequency of the subsystem [25].

In the process of reducing  $a$  from 62 m (design value) to 56.4 m (stable critical value), the eigenvalue real parts of each subsystem are negative, and the shiplift system is in stable state. However, the obvious change is that stability margin of the shallow water sloshing subsystem decreases rapidly (from  $-1.33 \times 10^{-5}$  to  $-8.18 \times 10^{-8}$ ). This means that the shallow water sloshing subsystem is the most vulnerable to instability.

When  $a$  is lower than 56.4 m, the eigenvalue real part of the shallow water sloshing subsystem changes from negative to positive, entering the unstable state. Continuing to reduce  $a$  to 13 m, causes the eigenvalue real part to become larger (from  $-8.18 \times 10^{-8}$  to 0.33), and the unstable vibration of shallow water sloshing subsystem becomes more serious. Meanwhile, the vibration frequency of shiplift chamber structure subsystem is rapidly decreased (from 4.98 rad/s to 0.34 rad/s), close to the unstable vibration frequency of the shallow water sloshing subsystem (from 0.22 rad/s to 0.37 rad/s). The vibration frequencies of the two subsystems are close to the resonance state. It can be inferred that the most unstable one (other than shallow water sloshing subsystem) is the shiplift chamber structure subsystem.

While  $a$  is reduced from 56.4 m to 13 m, the vibration frequencies of the hydraulic levelling subsystem and the main hoist subsystem remain stable, and the eigenvalue real part of the hydraulic levelling subsystem ( $-5.33$ ) is farther away from the virtual axis than the main hoist subsystem ( $-4.00$  to  $-0.38$ ). The stability margin of the hydraulic levelling subsystem is greater than the main hoist subsystem. For the 200 m level shiplift, the stability priority from high to low is hydraulic levelling subsystem, the main hoist subsystem, the shiplift chamber structure subsystem, and the shallow water sloshing subsystem.

## 2.3 Influence of Lift Height

Taking the 200 m level shiplift ( $a=62$  m) under hydraulic dynamic levelling as an example, variations of  $a_{cd}$  and subsystem vibration frequencies with lift height are analysed in Fig. 4.

It can be seen from Fig. 4a that with the increase of lift height (0 m to 200 m),  $a_{cd}$  becomes smaller (56.4 m to 41.2 m), which means that pitch stability is gradually enhanced. The main reason is that the length of suspended wire ropes becomes shorter with the rise of lift height; thus, the stiffness of suspended wire ropes increases rapidly, and pitch stability is enhanced. Figs. 4b to 4f show that the vibration frequencies of hydraulic levelling subsystem, main hoist subsystem, shiplift chamber subsystem, and shallow water sloshing subsystem change stably in their respective regions. For the 200 m level shiplift, pitch stability under dynamic hydraulic levelling can be guaranteed in the whole operation process.

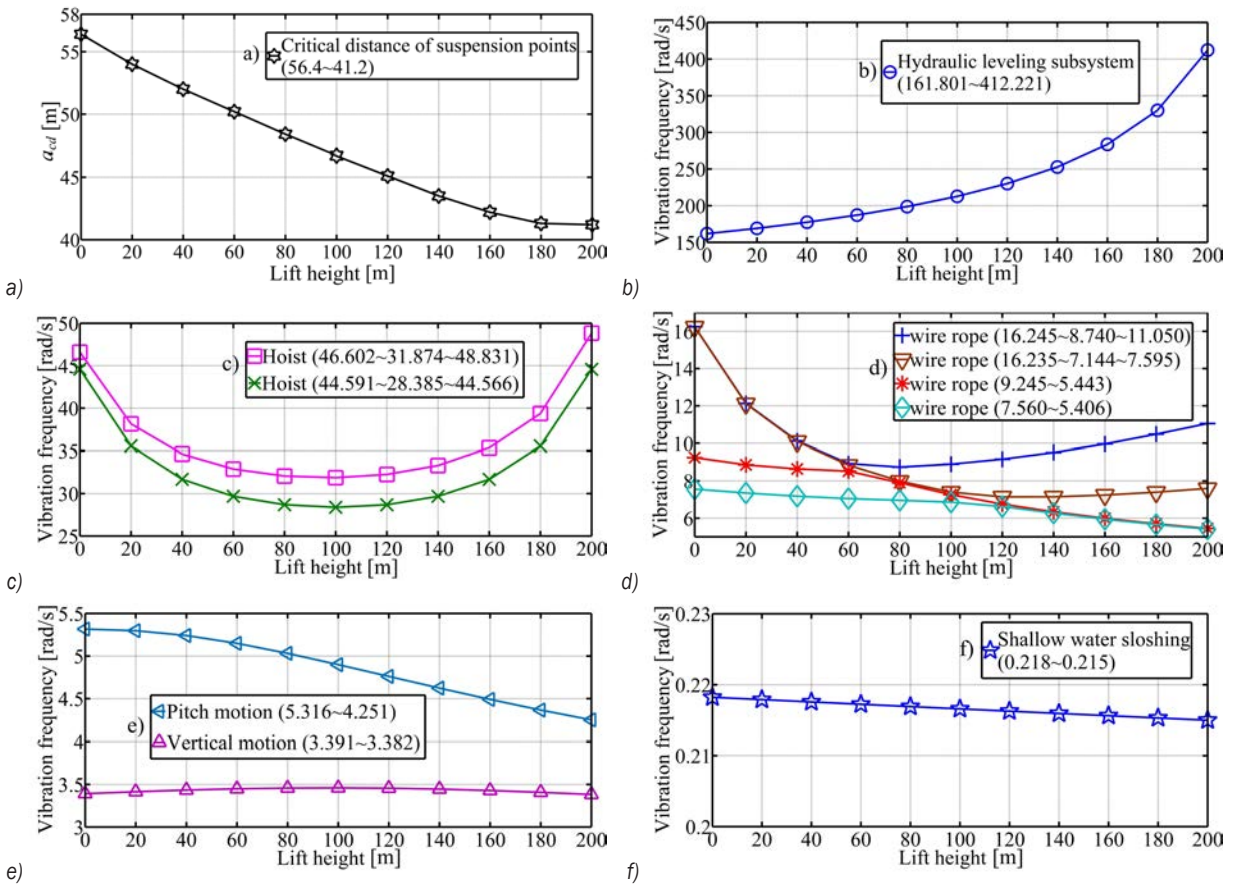


**Fig. 4.** Variations of a) critical distance of suspension points, b) hydraulic levelling subsystem vibration frequency, c) hoists vibration frequencies, d) wire ropes vibration frequencies, e) pitch and vertical motion vibration frequencies, f) shallow water sloshing vibration frequency with lift height

### 2.4 Influence of Synchronous Shaft Stiffness

The synchronous shaft system ensures the synchronization between the hoists and guarantees the shiplift smooth operation. Table 3 shows the variation of  $a_{cs}$  and  $a_{cd}$  with synchronous shaft stiffness increases.

**Table 3.** Effect of synchronous shaft stiffness on the pitch stability of the 200 m level shiplift

Critical distance of suspension points	Synchronous shaft stiffness increment						
	Design value	5 %	10 %	15 %	20 %	25 %	30 %
$a_{cd}$ [m]	56.4	55.7	55.0	54.4	53.8	53.3	52.9
$a_{cs}$ [m]	47.9	47.2	46.6	46.1	45.5	45.1	44.7

Table 3 displays that the pitch stability is enhanced with the synchronous shaft stiffness increases, regardless of hydraulic dynamic or static

levelling. For the hydraulic static levelling, the pitch stability is enhanced by 6.7 % when the synchronous shaft stiffness is increased by 30 %. For the dynamic hydraulic levelling, while the synchronous shaft stiffness raises by 30 %, pitch stability enhances about 6.2 %. It can be inferred that pitch stability of 200 m level shiplift can be effectively improved by increasing the synchronous shaft stiffness, whether it is hydraulic static or dynamic levelling.

### 2.5 Influence of Damping Ratio

The essence of stability is that system energy decays over time, and finally reaches a state of equilibrium with minimum energy. The subsystem damping plays an essential role in energy dissipation and attenuation. Table 4 analyses the influence of the subsystem damping ratio on the pitch stability.

**Table 4.** Effect of subsystem damping ratio on the pitch stability of the 200 m level shiplift

Series	$\zeta_j$	$\zeta_g$	$\zeta_v$	$\zeta_p$	$\zeta_w$	$\zeta_h$	$a_{cd}$ [m]
1	0.1	0.01	0.005	0.05	0.00024	0.03	56.4
2	0.1	0.01	0.005	0.05	$2 \times 0.00024$	0.03	44.8
3	0.1	0.01	0.005	0.05	0.00024	$2 \times 0.03$	56.39

where  $\zeta_g$  refers to [2],  $\zeta_j$  and  $\zeta_j$  are adopted from [4],  $\zeta_v$  comes from [6],  $\zeta_w$  is calculated according to [26] and  $\zeta_h$  is obtained by Eq. (3c).

Comparing series 1 and series 2, when  $\zeta_w$  is doubled, pitch stability safety factor is raised from 1.1 (i.e.  $62 / 56.4$ ) to 1.4 (i.e.  $62 / 44.8$ ). That is, increasing  $\zeta_w$  can effectively improve the pitch stability. The main reason is that the weakest stability link in the MHSF coupling system is the shallow water sloshing subsystem, and the increase of the sloshing damping ratio can accelerate the convergence and enhance stability. When the shiplift works, because of the existence of ship in the chamber,  $\zeta_w$  is greatly increased, and sloshing is suppressed. Compared with the ship-free state, pitch stability is improved, and the safety factor in the actual operation process is higher than the calculated value 1.1.

Comparing series 1 and series 3, while  $\zeta_h$  is doubled,  $a_{cd}$  is essentially unchanged. That is,  $\zeta_h$  hardly affects the pitch stability. The main reason is that the hydraulic levelling subsystem has the highest stability priority in the coupling system. Increasing is equivalent to raise the upper limit of stability but does not affect the lower limit of stability.

### 3 CONCLUSIONS

A new MHSF coupling dynamics model and a developed semi-analytical method are presented to investigate the pitch stability under hydraulic dynamic levelling. Taking four typical high-lift hoist vertical shiplifts as examples, the reliability of the proposed model and method is illustrated. The subsystem stability priority and influence factors on the pitch stability are analysed in detail. Pitch stability of the 200 m level shiplift under dynamic hydraulic levelling is focused. The key observations are summarized as follows:

1. Based on the closed-loop transfer function, multi-modal theory and second type Lagrangian equation, the models of hydraulic levelling subsystem, shallow water sloshing subsystem, the main hoist mechanical subsystem and shiplift chamber structure subsystem are built,

respectively. Subsequently, a core 21 order state matrix of the MHSF coupling system is proposed using state-space method.

2. A developed semi-analytical method integrating the Lyapunov motion stability theory and the Eigen-analysis method is proposed to judge the pitch stability and analyse subsystem characteristics. The results indicate that pitch stability under dynamic hydraulic levelling is reduced by 15 % to 44 % with respect to hydraulic static levelling, but dynamic hydraulic levelling will not cause instability. For the designed 200 m level shiplift, the critical distance of suspension points is 56.4 m, and the design parameters can guarantee the pitch stability safety factor under dynamic hydraulic levelling not less than 1.1.
3. In the MHSF coupling system, the stability priority from high to low is the hydraulic levelling subsystem, the main hoist subsystem, shiplift chamber structure subsystem, and the shallow water sloshing subsystem.
4. For the designed 200 m level shiplift, pitch stability enhances significantly (maximum 26.98 %) as the lift height increases (0 m to 200 m). Improving the synchronous shaft stiffness by 30 % can enhance the pitch stability about 6.2 %. Doubling the water boundary layer damping ratio can raise the pitch stability about 20.57 %.

### 4 ACKNOWLEDGMENTS

This study was supported by the National Key R&D Program of China (No. 2016YFC0402002), and the authors gratefully acknowledge this support.

### 5 NOMENCLATURES

- $a$  distance of suspension points, [m]  
 $a_d$  distance of suspension points given by designers, [m]  
 $a_{cd}$  critical distance of suspension points under hydraulic dynamic levelling, [m]  
 $a_{cs}$  critical distance of suspension points under hydraulic static levelling, [m]  
**A** state matrix of MHSF coupling system  
 $A_1$  non-rod cavity area of hydraulic cylinder, [m<sup>2</sup>]  
 $A_2$  rod cavity area of hydraulic cylinder, [m<sup>2</sup>]  
 $b_i$  eigenvalue equation coefficients  
 $B$  width of shiplift chamber, [m]  
 $B_1$  hoist at upstream  
 $B_2$  pulley at upstream  
 $B_3$  pulley at downstream  
 $B_4$  hoist at downstream

$c$	center point of shiplift chamber bottom	$t_6$	influence factor on torque counterweight suspended wire rope at downstream
$C$	equivalent synchronous shaft stiffness, [N·m·rad <sup>-1</sup> ]	$T$	kinetic energy, [J]
$C_{i,j}$	coefficient expressions	$V$	potential energy, [J]
$C_t$	total leakage coefficient related to load pressure, [m <sup>5</sup> ·N <sup>-1</sup> ·s <sup>-1</sup> ]	$V_t$	total volume of two cavities of hydraulic cylinder, [m <sup>3</sup> ]
$g$	gravity acceleration, [m·s <sup>-2</sup> ]	$\mathbf{x}$	state vector matrix
$G(s)$	transfer function of valve controlled asymmetric hydraulic cylinder	$z_{22}$	piston displacement, [m]
$G_B(s)$	closed-loop transfer function	$Z_1$	torque counterweight vertical displacement at upstream, [m]
$h$	lift height, [m]	$Z_2$	gravity counterweight vertical displacement at upstream, [m]
$H$	water depth of shiplift chamber, [m]	$Z_3$	gravity counterweight vertical displacement at downstream, [m]
$J_1$	equivalent inertia moment of hoist, [kg·m <sup>2</sup> ]	$Z_4$	torque counterweight vertical displacement at downstream, [m]
$J_2$	equivalent inertia moment of pulley, [kg·m <sup>2</sup> ]	$Z_5$	shiplift chamber vertical displacement, [m]
$J_3$	equivalent inertia moment of shiplift chamber, [kg·m <sup>2</sup> ]	$\alpha$	pitch angular displacement, [rad]
$k$	equivalent load wire rope stiffness, [N·m <sup>-1</sup> ]	$\beta_1$	first order modal function of sloshing
$K$	equivalent stiffness of wire ropes at upstream, [N·m <sup>-1</sup> ]	$\beta_e$	elastic modulus of oil, [Pa]
$K_a$	proportional amplifier gain	$\zeta_w$	first order water boundary-layer damping ratio
$K_{sv}$	flow gain of proportional speed regulating valve	$\zeta_h$	hydraulic damping ratio
$K_f$	sensor gain	$\zeta_j$	torsional vibration damping ratio
$K_q$	flow gain	$\zeta_g$	wire rope damping ratio
$K_{ce}$	total pressure flow coefficient including leakage, [m <sup>5</sup> ·N <sup>-1</sup> ·s <sup>-1</sup> ]	$\zeta_p$	pitch motion damping ratio
$K_c$	pressure-flow factor (the change rate of the load flow rate relative to the load pressure when the valve spool displacement is constant), [m <sup>5</sup> ·N <sup>-1</sup> ·s <sup>-1</sup> ]	$\zeta_v$	vertical motion damping ratio
$L$	length of shiplift chamber, [m]	$\Sigma_0$	mean free surface
$m_1$	half weight of torque counterweight, [kg]	$\rho$	water density, [kg·m <sup>-3</sup> ]
$m_2$	half weight of gravity counterweight, [kg]	$\varphi_1$	rotating angle displacement of hoist and pulley at upstream, [rad]
$m_3$	total weight of shiplift chamber, [kg]	$\varphi_2$	rotating angle displacement of hoist and pulley at downstream, [rad]
$M$	hydrodynamic moment with respect to point $c$ , [N·m]	$\omega_1$	first order natural frequency of fluid in the shiplift chamber, [rad·s <sup>-1</sup> ]
$M_t$	equivalent mass of piston and load wire rope, [kg]	$\omega_h$	hydraulic natural frequency, [rad·s <sup>-1</sup> ]
$n$	effective area ratio of two cavities of hydraulic cylinder	$\omega_r$	turning frequency of inertial link, [rad·s <sup>-1</sup> ]
$n_d$	pitch stability safety factor under hydraulic dynamic levelling		
$n_s$	pitch stability safety factor under hydraulic static levelling		
$R$	radius of hoists and pulleys, [m]		
$t_1$	torsional stiffness ratio of synchronous shaft and motor drive shaft		
$t_2$	influence factor on torque counterweight suspended wire rope at upstream		
$t_3$	influence factor on gravity counterweight suspended wire rope at upstream		
$t_4$	influence factor of elasticity modulus tolerance		
$t_5$	influence factor on gravity counterweight suspended wire rope at downstream		

## 6 REFERENCES

- [1] Yu, Q., Fang, X. (2008). Application of hydraulic pressure technology in modern shiplift. *Yangtze River*, vol. 39, no. 20, p. 71-72, DOI:10.3969/j.issn.1001-4179.2008.20.026. (in Chinese)
- [2] GB 51177(2016). *Design Code for Shiplift*. The Ministry of Water Resources of the People's Republic of China. Beijing, China. (in Chinese)
- [3] Cheng, G., Li, H., Ruan, S. (2005). Free vibration characteristics and stability analysis of shiplift system. *Journal of Mechanical Strength*, vol. 27, no. 3, p. 276-281, DOI:10.3321/j.issn:1001-9669.2005.03.002. (in Chinese)
- [4] Liao, L. (2014). Safety analysis and design of full balanced hoist vertical shiplifts. *Structural Engineering and Mechanics*, vol. 49, no. 3, p. 311-327, DOI:10.12989/sem.2014.49.3.311.

- [5] Cheng, X., Shi, D., Li, H., Xia, R., Zhang, Y., Zhou, J. (2018). Stability and parameters influence study of Fully Balanced Hoist Vertical Ship Lift. *Structural Engineering and Mechanics*, vol. 66, p. 583-594, DOI:10.12989/sem.2018.66.5.583.
- [6] Zhang, Y., Shi, D., Liao, L., Shi, L., Cheng, X. (2019). Pitch stability analysis of high-lift wire rope hoist vertical shiplift under shallow water sloshing-structure interaction. *Proceedings of the Institution of Mechanical Engineers, Part K: Journal of Multi-Body Dynamics*, DOI:10.1177/1464419319850666.
- [7] Niu, W., Wang, S., Wang, Y., Song, Y., Zhu, Y. (2017). Stability analysis of hybrid-driven underwater glider. *China Ocean Engineering*, vol. 31, no. 5, p. 528-538, DOI:10.1007/s13344-017-0061-y.
- [8] Banskchikov, A., Bourlakova, L. (2001). Computer algebra and problems of motion stability. *Mathematics and Computers in Simulation*, vol. 57, no. 3-5, p. 161-174, DOI:10.1016/S0378-4754(01)00336-6.
- [9] Ahmad, S., Yue, B. (2012). Motion stability dynamics for spacecraft coupled with partially filled liquid container. *Theoretical and Applied Mechanics Letters*, vol. 2, no. 1, art. ID 013002, DOI:10.1063/2.1201302.
- [10] Wu, Q., Zhang, L., Ma, Z. (2017). A model establishment and numerical simulation of dynamic coupled hydraulic-mechanical-electric-structural system for hydropower station. *Nonlinear Dynamics*, vol. 87, p. 459-474, DOI:10.1007/s11071-016-3053-1.
- [11] Peng, H., Pan, E., Zhong, T., Hu, Z. (2004). Analysis on tension balance characteristic of hydraulics system of three gorges shiplift. *Chinese Journal of Mechanical Engineering*, vol. 40, no. 1, p. 155-159, DOI:10.3321/j.issn:0577-6686.2004.01.031. (in Chinese)
- [12] Zeng, W., Yang, J., Yang, W. (2016). Instability analysis of pumped-storage stations under no-load conditions using a parameter-varying model. *Renewable Energy*, vol. 90, p. 420-429, DOI:10.1016/j.renene.2016.01.024.
- [13] Zheng, Y., Eben Li, S., Wang, J., Cao, D., Li, K. (2015). Stability and scalability of homogeneous vehicular platoon: study on the influence of information flow topologies. *IEEE Transactions on Intelligent Transportation Systems*, p. 1-13, DOI:10.1109/TITS.2015.2402153.
- [14] Martynyuk, A. (2003). *Advances in Stability Theory at the End of the 20<sup>th</sup> Century*. CRC Press, London, DOI:10.1201/b12543.
- [15] Stojanović, V., Petković, M., Deng, J. (2018). Instability of vehicle systems moving along an infinite beam on a viscoelastic foundation. *European Journal of Mechanics AsSolids*, vol. 69, p. 238-254, DOI:10.1016/j.euromechsol.2017.12.007.
- [16] Liu, X., Liu, C. (2007). Eigenanalysis of oscillatory instability of a hydropower plant including water conduit dynamics. *IEEE Transactions on Power Systems*, vol. 22, no. 2, p. 675-681, DOI:10.1109/TPWRS.2007.895156.
- [17] Yang, W., Norrlund, P., Chung, C., Yang, J., Lundin, U. (2018). Eigen-analysis of hydraulic-mechanical-electrical coupling mechanism for small signal stability of hydropower plant. *Renewable Energy*, vol. 115, p. 1014-1025, DOI:10.1016/j.renene.2017.08.005.
- [18] Yu, X., Zhang, J., Fan, C., Chen, S. (2016). Stability analysis of governor-turbine-hydraulic system by state space method and graph theory. *Energy*, vol. 114, p. 613-622, DOI:10.1016/j.energy.2016.07.164.
- [19] Yu, X.D., Zhang, J., Chen, S., Liu, J.C. (2016). Stability analysis of the governor-turbine-hydraulic system of pumped storage plant during small load variation. *IOP Conference Series: Earth and Environmental Science*, vol. 49, art. ID 112004, DOI:10.1088/1755-1315/49/11/112004.
- [20] Zhang, Y., Shi, D., Shi, L., Xia, R., Cheng, X., Zhou, J. (2019). Analytical solution of capsizing moments in ship chamber under pitching excitation. *Proceedings of the Institution of Mechanical Engineers, Part C: Journal of Mechanical Engineering Science*, vol. 233, no. 15, p. 5294-5301, DOI:10.1177/0954406219843327.
- [21] Shi, L., Zhang, Y., Cheng, X.H., Zhou, J., Shi, D.W., Xia, R. (2019) Stability analysis of Hoist Vertical Shiplift chamber under pitching motion. *IOP Conference Series: Materials Science and Engineering*, vol. 631, art. ID 032028, DOI:10.1088/1757-899X/631/3/032028.
- [22] Stephen, J.J., Sannasiraj, S.A., Sundar, V. (2016). Numerical simulation of sloshing in a rectangular tank under combined horizontal, vertical and rotational oscillations. *Proceedings of the Institution of Mechanical Engineers, Part M: Journal of Engineering for the Maritime Environment*, vol. 230, no. 1, p. 95-113, DOI:10.1177/1475090214533512.
- [23] Faltinsen, O.M., Timokha, A.N. (2009). *Sloshing*. Cambridge University Press, Cambridge.
- [24] Walters R.B. (2000) System Analysis of Electro-hydraulic Control Systems. In: *Hydraulic and Electric-Hydraulic Control Systems*. Springer, Dordrecht, DOI:10.1007/978-94-015-9427-1\_12.
- [25] Blair, T. H. (2016). Control Systems. *Energy Production Systems Engineering*. John Wiley and Sons, Inc. DOI:10.1002/9781119238041.ch23.
- [26] Keulegan, G. (1959). Energy dissipation in standing waves in rectangular basins. *Journal of Fluid Mechanics*, vol. 6, no. 1, p. 33-50, DOI:10.1017/S0022112059000489.



# Vsebina

**Strojniški vestnik - Journal of Mechanical Engineering**  
**letnik 66, (2020), številka 4**  
**Ljubljana, april 2020**  
**ISSN 0039-2480**

**Izhaja mesečno**

## **Razširjeni povzetki (extended abstracts)**

- Branislav Panić, Jernej Klemenc, Marko Nagode: Preučevanje Gaussovih mešanih modelov za potrebe klasifikacije: "Raziskava na primeru klasifikacije napak v ležajih" SI 29
- VanThien Nguyen, VietHung Nguyen, VanTrinh Pham: Nadzor nad obrabljanjem orodja med procesom čelnega rezkanja z globokim zloženim samokodirnikom SI 30
- Jakub Sikorski, Witold Pawlowski: Notranje trenje v krogličnih ležajih pri zelo nizkih temperaturah SI 31
- Sanjay Sundriyal, Vipin, Ravinderjit Singh Walia: Študija vpliva kovinskega prahu pri skoraj suhi elektroerozijski obdelavi SI 32
- A.K. Babu, G. Kumaresan, V. Antony Aroul Raj, R. Velraj: Eksperimentalna raziskava sušenja listov v tankih plasteh na pladnjih v šaržni sušilni komori na toplotno črpalko SI 33
- Yang Zhang, Duanwei Shi, Tong Xiao, Ji Zhou, Xionghao Cheng: Analiza vzdolžne stabilnosti sklopljenega mehansko-hidravlično-strukturno-fluidnega sistema visokega vertikalnega dvigala za ladje SI 34



# Preučevanje Gaussovih mešanih modelov za potrebe klasifikacije: Raziskava na primeru klasifikacije napak v ležajih

Branislav Panič\* – Jernej Klemenc – Marko Nagode  
Univerza v Ljubljani, Fakulteta za strojništvo, Slovenija

Spremljanje zdravja struktur ter zaznavanje napak je dandanes izjemno popularna tematika. Številne obremenitve, okolja itn. vplivajo na komponente ter sisteme na različne načine ter lahko povzročijo napake, katerih posledica je nepravilno obratovanje. Obratovanje elementa lahko opazujemo na podlagi meritev s pomočjo različne merilne opreme. Z opazovanjem pravičnega (brez napake) ter nepravilnega (z napako) obratovanja sistema ali elementa lahko določimo diskriminativne funkcije, ki na podlagi meritev ločujejo ti dve stanji. Na ta način lahko spremljamo stanje ter zaznamo napako v elementu ali sistemu na podlagi naknadnih meritev.

Osnova za čim bolj pravilno zaznavanje napak temelji na uporabi ustrezne klasifikacijske metode, kot je klasifikacija na podlagi Gaussovega mešanega modela. Glavni problem pri tej metodi je nedvomno ocena parametrov mešanega modela. Gaussov mešani model vsebuje množico parametrov. Za oceno parametrov obstaja veliko načinov, med katerimi je eden najpogosteje uporabljenih algoritem pričakovanja in maksimizacije (angl. Expectation-Maximization) ali skrajšano EM. Parametri, ocenjeni z uporabo EM algoritma, so lahko neustrezni, saj je algoritem zelo podvržen t. i. inicializaciji oz. potrebi po nekaterih začetnih parametih Gaussovega mešanega modela. Če so začetni parametri neustrezni, bo EM algoritem konvergirala k neustreznemu lokalnemu optimumu in na ta način ogrozil uspešnost klasifikacije. Po drugi strani za oceno parametrov Gaussovega mešanega modela obstaja veliko heuristik. Ena najbolj znana je zagotovo REBMIX algoritem. REBMIX heuristika zagotavlja hitrost, pri tem pa ni nobenega zagotovila, da so ocenjeni parametri pravilni. Edini način preverjanja ocene parametrov je njena uporaba, ki predstavlja uspešnost klasifikacije. Ker tudi ni zagotovila, da je EM algoritem konvergirala h globalnemu optimumu, je edini način preverjanja ocene parametrov, npr. uspešnost klasifikacije.

Zaznavanje napak je področje, na katerem obstaja izjemno visoka zahteva po uspešnosti klasifikacije. Zaradi tega je nujno oceniti najboljše parametre Gaussovega mešanega modela tako, da je uspešnost klasifikacije visoka. Parametri Gaussovega mešanega modela so ocenjeni na podlagi štirih različnih metod, mda, mclust, rebmix ter rebmix&em. Vse našteje metode so poimenovane po imenih ustreznih R paketov. Vse simulacije in preračuni so prav tako izvedeni v R programskem jeziku. Dodatno so neparametrične metode za klasifikacijo, kot je metoda podpornih vektorjev in nevronske mreže, vključene v primerjavo. Kot eden izmed prevladujočih problemov zaznavanja napak v strojništvu je izbran primer zaznavanja napak pri ležajih. Ležaji so enostavno zamenljivi in poceni strojni elementi, vendar nezaznava napak pri obratovanju velikokrat pripelje do odpovedi ne samo ležaja, pač pa tudi nekaterih drugih, varnostno bolj kritičnih elementov. Zaradi tega je zelo pomembno zaznati napako v ležaju pravočasno. Uporabljeni sta dve bazi podatkov, baza podatkov CWRU ter VSBD. Primerjava metod temelji na k-kratnem navkrižnem preverjanju (angl. k-fold cross validation). Za vsako klasifikacijsko metodo sta zajeti dve cenilki, uspešnost klasifikacije ter čas izračuna.

Na podlagi rezultatov se je klasifikacija s pomočjo Gaussovega mešanega modela izkazala za konkurenčno in uspešno. Na obeh bazah podatkov je ena izmed metod klasifikacije, ki temelji na Gaussovem mešanem modelu, dala najboljše rezultate. Varianti rebmix in mda sta se izkazali kot hitri, vendar manj točni, mclust in rebmix&em pa počasnejši, a točnejši. Prispevek tega članka je rezultat primerjave različnih metod ocene parametrov Gaussovega mešanega modela. Ustrezna ocena parametrov Gaussovega mešanega modela lahko privede do visoke uspešnosti klasifikacije. Prav tako lahko omogoči uporabo te metode v visoko zahtevnih področjih, kot je področje zaznavanja napak.

**Ključne besede:** Gaussov mešan model, klasifikacija, ocena napak ležajev, ocena parametrov, uspešnost klasifikacijske metode

# Nadzor nad obrabljanjem orodja med procesom čelnega rezkanja z globokim zloženim samokodirnikom

VanThien Nguyen – VietHung Nguyen\* – VanTrinh Pham  
Tehniška univerza v Hanoju, VietNam

Rutinsko zbiranje podatkov o obratovanju sistemov je pomembno za analiziranje, diagnosticiranje in napovedovanje potencialnih težav v kontekstu razvoja industrije 4.0. Upoštevanje obrabljanja orodja med obdelavo kovin z odrezavanjem ima pomembno vlogo pri izboljševanju kakovosti izdelkov in produktivnosti v proizvodni industriji. Z nadzorom rezalnega orodja je mogoče identificirati stanja obrabe orodja in to je področje zanimanja mnogih raziskovalcev. Glavni cilj pričujoče študije je bil zasnovati globoko nevronska mrežo (DLN) za identifikacijo stanj obrabe orodja pri operacijah čelnega rezkanja železove litine za zagotavljanje zanesljivosti in stabilnosti procesa odrezavanja.

Na podlagi zbranih podatkov o vibracijah je bil podrobno preučen model DLN za napovedovanje stanj obrabe orodja pri obdelavi kovin z odrezavanjem. V raziskavi je bila uporabljena metoda učenja DLN na osnovi podatkov za doseganje visoke stopnje točnosti, ki potrjuje uspešnost napovedi. DLN, ki je bila uporabljena za klasifikacijo obrabe orodja, je bila oblikovana z združitvijo zloženega samokodirnika (SAE) in klasifikatorja softmax. V tem modelu DLN so bile s SAE izločene visokonivojske značilke kompleksnega signala vibracij v povezavi z obrabljanjem orodja, nato pa je bil uporabljen klasifikator softmax za točno identifikacijo vzorcev značilk.

Zasnovan je bil dvoslojni SAE za učinkovito izločanje pomembnih značilk, ki imajo vlogo vhodov za klasifikator softmax pri učenju in testiranju. Klasifikacijska točnost je pri vseh preizkušanih znašala 100 %. Sledi sklep, da so SAE z nenadzorovanimi algoritmi učenja primerna rešitev za izločanje značilk obrabe orodja. Klasifikator softmax z aktivacijsko funkcijo je bil uporabljen kot klasifikacijski sloj v arhitekturi DLN za ocenjevanje verjetnosti vzorcev, rezultat pa je bila 100-odstotna točnost. Značilke, pridobljene s SAE, so bile uporabljene tudi v modelih s plitkim klasifikatorjem, kot sta klasifikator z usmerjeno nevronska mrežo (FNN) in klasifikator z algoritmom k-najbližjih sosedov (k-NN). Izkazalo se je, da je značilke mogoče uporabiti v poljubnem klasifikacijskem modelu za doseganje klasifikacijske točnosti vsaj 65 %. Za učenje modelov klasifikatorjev je bila uporabljena samo polovica vzorcev značilk, kar dokazuje sposobnost SAE za izločanje značilk. Učenje modela DLN traja 0,3072 sekunde z optimiziranimi fazami gradnje DLN za pridobivanje rezultatov s popolno klasifikacijsko točnostjo za arhitekturo DLN. Čas učenja je daljši kot pri modelu klasifikatorja z algoritmom k-NN, kjer učenje traja le 0,1098 s. Na osnovi teh rezultatov je mogoče izraziti veliko gotovost v primernost DLN za diagnostiko na področju vzdrževanja v strojništvu, denimo pri odkrivanju napak v ležajih ali zobnikih.

Originalne podatke o vibracijah iz procesa čelnega rezkanja v časovni domeni je treba za učinkovito delovanje pred vnosom v DLN predstaviti v frekvenčno domeno s hitro Fourierjevo transformacijo (FFT). Opisana arhitektura DLN ni bila uporabljena za zaznavanje drugih stanj rezalnega orodja v procesu čelnega rezkanja, kot je zlom ali iztek obstojnosti orodja, zato bo to ena od možnih tem za nadaljnje raziskave.

Glavni prispevki študije so: (1) pridobitev signala vibracij iz procesa čelnega rezkanja s senzorji in predobdelava podatkov; (2) izločitev visokonivojskih značilk vibracijskega signala v povezavi s stanji obrabe orodja; (3) klasifikacija stanj obrabe orodja s prepoznavanjem vzorcev. Naštete tri faze so vdelane v arhitekturi DLN za identifikacijo obrabljanja orodja, ki bo uporabna v industrijski proizvodnji.

**Ključne besede:** čelno rezkanje, obraba orodja, zloženi samokodirnik (SAE), globoke nevronske mreže (DLN), železova litina, identifikacija, softmax

# Notranje trenje v krogličnih ležajih pri zelo nizkih temperaturah

Jakub Sikorski, Witold Pawlowski\*

Tehniška univerza v Lodzu, Inštitut za obdelovalne stroje in proizvodni inženiring, Poljska

Predstavljena raziskava je bila opravljena z namenom pridobitve znanja o vedenju masti in krogličnih ležajev med obratovanjem pri zelo nizkih temperaturah do  $-195\text{ }^{\circ}\text{C}$ . To znanje bo v prihodnosti uporabno pri konstruiranju strojev, ki so namenjeni uporabi v zelo ostrih pogojih.

Članek podaja rezultate analize delovanja jeklenih in keramičnih ležajev pri zelo nizkih temperaturah. Testi so bili opravljeni na krogličnih ležajih pri temperaturah do  $-195\text{ }^{\circ}\text{C}$ , doseženih s pomočjo tekočega dušika. V raziskavo so bili vključeni ležaji, tovarniško mazani s standardnimi mazivi, z grafitnim prahom in s prahom molibdenovega disulfida. Študija izboljšuje poznavanje vedenja ležajev in maziv pri zelo nizkih temperaturah, njeni izsledki pa bodo tako uporabni pri konstruiranju nove generacije robotov za raziskovanje vesolja in bližnjih planetov osončja.

Pri vseh meritvah so bili uporabljeni kroglični ležaji tipa 625 velikosti  $5\text{ mm} \times 16\text{ mm} \times 5\text{ mm}$  in brez tesnil. Ležaji so bili po montaži na pogonsko gred nameščeni v okvir in vpeti z objemko in vijaki, ki so bili zategnjeni s ponovljivim momentom. Prvi korak priprav na meritve notranjega trenja v ležajih je bil določitev moči upora proti gibanju v samem pogonskem sistemu. V ta namen je bila analizirana poraba moči v pogonskem motorju in v napajalnih kabljih. Uporabljeni laboratorijski izvor omogoča računalniško krmiljenje električne napetosti in toka za napajanje motorja, napajanje motorja pa je tako v celoti ponovljivo. Vrednosti porabe moči elektromotorja in kablov so bile odštete od celotne porabe (vključno z ležajem) za določitev celotnih izgub med obratovanjem ležaja. Ležaj je bil nato prestavljen v nizkotemperaturno komoro, ki zagotavlja postopno ohladitev do temperature  $-195\text{ }^{\circ}\text{C}$  v 8 do 22 minutah s pomočjo tekočega dušika. Poraba moči je bila v tem času izmerjena in zabeležena 80-krat na minuto. Na osnovi teh podatkov je bilo pripravljenih več grafikonov.

Opravljenе meritve so pokazale, da je vrsta mazanja ležaja mnogo pomembnejša od materiala, iz katerega je ta izdelan. V nasprotju s splošnim prepričanjem se lahko jekleni ležaji uporabljajo tudi v strojih, ki obratujejo pri zelo nizkih temperaturah, vendar pod pogojem, da se viskozno mazivo zamenja s suhim mazivom. Praktično linearno povečanje izgub moči v ležaju vodi k sklepu, da mora biti obratovanje jeklenih in keramičnih ležajev možno in zanesljivo tudi pri temperaturah pod  $-195\text{ }^{\circ}\text{C}$ . Najmanjše notranje trenje v ležajih je bilo ugotovljeno pri molibdenovem disulfidu, ki učinkovito maže tako jeklene kakor tudi keramične kroglične ležaje. Njegove lastnosti so ostale praktično nespremenjene pri vseh meritvah ležajev.

Porast izgub moči v ležaju z zmanjševanjem temperature je bila gotovo posledica krčenja aluminijastega okvirja, ki drži ležaj, v tej fazi raziskav pa ni mogoče izključiti niti večanja izgub zaradi krčenja samega ležaja. Prihodnje raziskave bodo razširile predstavljeno temo na interakcije ležaja z materiali, ki se uporabljajo pri izdelavi sestavov gredi in pest, kot so aluminijeve in titanove zlitine.

Članek podaja informacije o vedenju maziv in krogličnih ležajev pri temperaturah do  $-195\text{ }^{\circ}\text{C}$ . To je pomembno, ker večina obstoječih raziskav obravnava težave z mazanjem pri povišanih temperaturah, le redke pa širijo obravnavano temperaturno območje do  $-80\text{ }^{\circ}\text{C}$ .

**Ključne besede:** kotalni ležaji, kotalni upor, mazanje, nizke temperature

# Študija vpliva kovinskega prahu pri skoraj suhi elektroerozijski obdelavi

Sanjay Sundriyal<sup>1</sup> – Vipin<sup>1</sup> – Ravinderjit Singh Walia<sup>2,\*</sup>

<sup>1</sup>Tehniška univerza v Delhiju, Indija

<sup>2</sup>Tehniški kolidž v Punjabu, Indija

Proces skoraj suhe elektroerozijske obdelave (ND-EDM) je prijazen do okolja. V tej študiji je bil opravljen poskus izboljšave učinkovitosti procesa obdelave orodnega jekla EN-31 po postopku ND-EDM z dodajanjem kovinskega prahu v dielektrik. Skoraj suha elektroerozijska obdelava s primešanim prahom (PMND-EDM) ima več prednosti v primerjavi s postopkom ND-EDM in konvencionalno elektroerozijsko obdelavo, med drugim višjo stopnjo odvzema materiala (MRR), nizko površinsko hrapavost ( $R_a$ ), oster rezalni rob, manjšo pretaljeno plast in nižjo stopnja odlaganja delcev. Izhodne odvisne spremenljivke so MRR,  $R_a$ , preostale napetosti (RS) in mikrotrdota (MH) obdelanih površin.

Opravljen je bil nadaljnja analiza obdelovanca in primerjava med ND-EDM in PMND-EDM. Uporaba sistema minimalnega mazanja ima pomembno vlogo pri točnosti obdelanih izdelkov, obenem pa preprečuje onesnaženje okolja in tveganja za zaposlene. Z uporabo optimalnih tekočin pri obdelavi kovin je mogoče doseči ekonomske koristi in obvarovati okolje. V pričujoči raziskavi je bil po natančnem pregledu literature opravljen poskus preučitve postopka PMND-EDM z vidika vplivov na vrednosti MRR,  $R_a$ , preostalih napetosti (RS) in mikrotrdote (MH). Pri predlaganem postopku obdelave je bilo ugotovljeno povišanje vrednosti MRR,  $R_a$  in MH za 17,85 %, 16,36 % oz. 62,69 %, medtem ko se je vrednost RS zmanjšala za 56,09 %.

Predhodne raziskave PMND-EDM so bile omejene na preučitev mikrotrdote površine obdelanih komponent in pričujoča študija zato predstavlja korak naprej k podrobnejšim raziskavam PMND-EDM. Oblikovan je bil nov pristop k preučevanju vloge trifaznega dielektrika z različnimi dimenzijami elektrod, koncentracijo kovinskih prahov in pretoki. Razvit je bil eksperiment za preučevanje vpliva koncentracije kovinskih prahov, različnih elektrod in pretoka dielektrika na zmogljivost obdelave, merjeno s prej omenjenimi dejavniki.

Na koncu je bila opravljena še primerjava zmogljivosti obdelave po postopkih ND-EDM in PMND-EDM na osnovi rezultatov eksperimentov.

**Ključne besede:** stopnja odvzema materiala, skoraj suha elektroerozijska obdelava, skoraj suha elektroerozijska obdelava s primešanim prahom, preostale napetosti, površinska hrapavost

# Eksperimentalna raziskava sušenja listov v tankih plasteh na pladnjih v šaržni sušilni komori na toplotno črpalko

A.K. Babu<sup>1,\*</sup> – G. Kumaresan<sup>2</sup>, – V. Antony Aroul Raj<sup>3</sup>, – R. Velraj<sup>2</sup>

<sup>1</sup> Tehniški kolidž Easwari, Oddelek za avtomobilsko tehniko, Chennai, Indija

<sup>2</sup> Inštitut za energetiko, Univerza Anna, Chennai, Indija

<sup>3</sup> Tehniški kolidž Easwari, Oddelek za strojništvo, Chennai, Indija

Pri pridelavi svežih kmetijskih proizvodov nastajajo izgube med nabiranjem/obiranjem, rokovanjem, skladiščenjem, obdelavo in prevozom. Po oceni iz analize, ki jo je leta 2011 opravila Organizacija Združenih narodov za prehrano in kmetijstvo (FAO), je letna globalna količina živilskih odpadkov približno 1,3 milijarde ton, kar ustreza približno eni tretjini celotne proizvodnje hrane za ljudi. Sveže sadje, zelenjava in listi se v toplih podnebnih pokvarijo in niso več varni za prehrano. FAO ocenjuje, da so izgube med vsemi vrstami hrane največje pri sadju in pri zelenjavi, tudi do 60-odstotne. Svežo hrano je mogoče zaščititi pred kvarjenjem s sušenjem. Pri sušenju se rabi veliko energije – v Indiji in v večini razvitih držav gre na ta račun kar od 12 % do 20 % celotne industrijske rabe energije. Glavni razlog je v tem, da je treba za odstranitev vode in drugih topil dovajati latentno izparilno toploto.

Kmetijske proizvode je mogoče sušiti med transportom z neposrednim izkoriščanjem odpadne toplote ali v sušilnikih na toplotno črpalko. Cilj pričujoče raziskave je bil zasnovati sušilnik na toplotno črpalko s komoro za sušenje kmetijskih proizvodov med prevozom. Sušilnik mora zagotavljati majhno rabo energije in visoko stopnjo izločanja vlage.

Obširna analiza literature s področja sušenja listov je pokazala, da še ne obstaja primerna konstrukcija komore za šaržno sušenje listov s toplotno črpalko v zaprti zanki. Zato je bila s pomočjo programske opreme za računalniško dinamiko fluidov (CFD) zasnovana in izdelana optimizirana sušilna komora, ki je bila nato preizkušena v sušilniku na toplotno črpalko. Opravljena je bila eksperimentalna analiza z vzorci listov ščira v optimalnih delovnih pogojih, ki so bili določeni na podlagi obširnega pregleda literature o sušenju listov. Ugotovitve se ujema z rezultati mnogih predhodnih študij, ki so našteje v virih. Preizkušeni sušilnik je primeren za sušenje vseh vrst listja med tranzitom v sušilnikih na toplotno črpalko.

V prihodnjih raziskavah bo mogoče uporabiti napredne modele sušenja za izboljšanje natančnosti razvitega simulacijskega modela.

**Ključne besede:** listi ščira, šaržni sušilnik, sušilnik na toplotno črpalko, grelna število, sušenje v tankih plasteh

# Analiza vzdolžne stabilnosti sklopljenega mehansko-hidravlično-strukturno-fluidnega sistema visokega vertikalnega dvigala za ladje

Yang Zhang – Duanwei Shi – Tong Xiao – Ji Zhou – Xionghao Cheng

Univerza v Wuhanu, Šola za energetiko in strojništvo, Kitajska

Večina visokih vertikalnih dvigal za ladje, ki so danes v uporabi, je opremljenih s hidravličnim podsistemom, ki je namenjen izravnavanju korita dvigala in izenačevanju napetosti v vrveh. Ko se med obratovanjem zažene hidravlični sistem za izravnavanje (dinamično hidravlično izravnavanje), se oblikuje kompleksen sklopljeni mehansko-hidravlično-strukturno-fluidni sistem (MHFS). Raziskovalci trenutno ne razpolagajo z ugotovitvami glede vzdolžne stabilnosti korit za dviganje ladij med obratovanjem, inženirji pa se pri projektiranju kritične razdalje med obešalnimi točkami preveč zanašajo na splošne izkušnje. Zagon sistema za hidravlično izravnavanje je trenutno dovoljen šele po zaustavitvi dvigala (statično hidravlično izravnavanje), kar močno vpliva na učinkovitost obratovanja.

Za razrešitev problema dinamične stabilnosti korita za dviganje ladij pri dinamičnem hidravličnem izravnavanju je predstavljena polanalitična metoda, ki vključuje oceno vzdolžne stabilnosti in izračun kritične razdalje med obešalnimi točkami. Ta metoda predstavlja teoretično osnovo za zasnovo konstrukcije in izbiro režima obratovanja visokega vertikalnega dvigala za ladje.

Modeli podsistema za hidravlično izravnavanje, podsistema pljuskajoče plitke vode, glavnega mehanskega podsistema dvigala in podsistema konstrukcije korita dvigala so bili zgrajeni na osnovi zaprtozračne prenosne funkcije, teorije večmodalnosti in Lagrangeove enačbe druge vrste. Nato je bila po metodi prostora stanj določena matrika stanj 21. reda za sklopljeni sistem MHSF. Za oceno vzdolžne stabilnosti, izračun kritične razdalje med obešalnimi točkami in analizo lastnosti podsistemov sta bili uporabljeni teorija stabilnosti gibanj po Lyapunovu in metoda analize lastnih vrednosti.

Vzdolžna stabilnost visokega vertikalnega dvigala za ladje je bila analizirana po polanalitični metodi z analitično matriko stanj in numeričnimi izračuni v programu Mathematica.

Članek spada v področja dinamike več teles, interakcij med pljuskajočimi fluidi in konstrukcijami ter analize stabilnosti.

Rezultati, ugotovitve: (1) Vzdolžna stabilnost pri dinamičnem hidravličnem izravnavanju se v primerjavi s statičnim hidravličnim izravnavanjem zmanjša za 15 % do 44 %, toda dinamično hidravlično izravnavanje ne povzroča nestabilnosti. (2) Med podsistemi v sklopljenem sistemu MHSF je najverjetnejša nestabilnost podsistema pljuskajoče plitve vode, na katero vpliva razdalja med obešalnimi točkami. (3) Kritična razdalja med obešalnimi točkami pri dvigalu za ladje, ki se projektira za premostitev višinske razlike 200 m, znaša 56,4 m. Konstrukcijski parametri zagotavljajo, da varnostni faktor vzdolžne stabilnosti pri dinamičnem hidravličnem izravnavanju ni manjši od 1,1. Vzdolžna stabilnost občutno raste (maksimum je 26,98 %) s povečevanjem višine dviga (0 m do 200 m). Ob povečanju togosti sinhrono gredi za 30 % se izboljša za približno 6,2 %. S podvojitvijo stopnje dušenja mejne plasti vode pa se vzdolžna stabilnost poveča za približno 20,57 %.

V članku ni bil upoštevan vpliv guganja ladje. Prihodnje raziskave bodo lahko osredotočene na kompleksno odvisnosti sklopitve fluida in trdne snovi oz. na interakcije med koritom za dviganje ladje, ladjo in vodo. Za nadaljnje raziskave vertikalnega dvigala za ladje bi bil dragocen tudi večdisciplinarni fizikalni model za eksperimentalno potrditev, ki bi vključeval mehanske prenose, upravljanje hidravlike in pljuskanje.

Prispevek, novosti, vrednost: (1) Postavljen je bil nov model dinamike sklopljenega mehansko-hidravlično-strukturno-fluidnega sistema visokega vertikalnega dvigala za ladje. (2) Razvita in predstavljena je bila polanalitična metoda za analizo lastnosti vzdolžne stabilnosti. (3) Članek podaja teoretične osnove in tehnično podporo pri projektiranju kritične razdalje med obešalnimi točkami dvigala za ladje. Navaja tudi izhodišča za analizo stabilnosti sklopljenih dinamičnih sistemov več teles.

**Ključne besede:** dvigalo za ladje, vzdolžna stabilnost, dinamično hidravlično izravnavanje, analiza lastnih vrednosti, metoda prostora stanj, dinamika

# Guide for Authors

All manuscripts must be in English. Pages should be numbered sequentially. The manuscript should be composed in accordance with the Article Template given above. The maximum length of contributions is 12 pages (approx. 5000 words). Longer contributions will only be accepted if authors provide justification in a cover letter. For full instructions see the Information for Authors section on the journal's website: <http://en.sv-jme.eu>.

## SUBMISSION:

Submission to SV-JME is made with the implicit understanding that neither the manuscript nor the essence of its content has been published previously either in whole or in part and that it is not being considered for publication elsewhere. All the listed authors should have agreed on the content and the corresponding (submitting) author is responsible for having ensured that this agreement has been reached. The acceptance of an article is based entirely on its scientific merit, as judged by peer review. Scientific articles comprising simulations only will not be accepted for publication; simulations must be accompanied by experimental results carried out to confirm or deny the accuracy of the simulation. Every manuscript submitted to the SV-JME undergoes a peer-review process.

The authors are kindly invited to submit the paper through our web site: <http://ojs.sv-jme.eu>. The Author is able to track the submission through the editorial process - as well as participate in the copyediting and proofreading of submissions accepted for publication - by logging in, and using the username and password provided.

## SUBMISSION CONTENT:

The typical submission material consists of:

- A **manuscript** (A PDF file, with title, all authors with affiliations, abstract, keywords, highlights, inserted figures and tables and references),
  - Supplementary files:
    - a **manuscript** in a WORD file format
    - a **cover letter** (please see instructions for composing the cover letter)
    - a ZIP file containing **figures** in high resolution in one of the graphical formats (please see instructions for preparing the figure files)
    - possible **appendices** (optional), cover materials, video materials, etc.
- Incomplete or improperly prepared submissions will be rejected with explanatory comments provided. In this case we will kindly ask the authors to carefully read the Information for Authors and to resubmit their manuscripts taking into consideration our comments.

## COVER LETTER INSTRUCTIONS:

Please add a **cover letter** stating the following information about the submitted paper:

1. Paper **title**, list of **authors** and their **affiliations**. **One** corresponding author should be provided.
2. **Type of paper**: original scientific paper (1.01), review scientific paper (1.02) or short scientific paper (1.03).
3. A **declaration** that neither the manuscript nor the essence of its content has been published in whole or in part previously and that it is not being considered for publication elsewhere.
4. State the **value of the paper** or its practical, theoretical and scientific implications. What is new in the paper with respect to the state-of-the-art in the published papers? Do not repeat the content of your abstract for this purpose.
5. We kindly ask you to suggest at least two **reviewers** for your paper and give us their names, their full affiliation and contact information, and their scientific research interest. The suggested reviewers should have at least two relevant references (with an impact factor) to the scientific field concerned; they should not be from the same country as the authors and should have no close connection with the authors.

## FORMAT OF THE MANUSCRIPT:

The manuscript should be composed in accordance with the Article Template. The manuscript should be written in the following format:

- A **Title** that adequately describes the content of the manuscript.
- A list of **Authors** and their **affiliations**.
- An **Abstract** that should not exceed 250 words. The Abstract should state the principal objectives and the scope of the investigation, as well as the methodology employed. It should summarize the results and state the principal conclusions.
- 4 to 6 significant **key words** should follow the abstract to aid indexing.
- 4 to 6 **highlights**; a short collection of bullet points that convey the core findings and provide readers with a quick textual overview of the article. These four to six bullet points should describe the essence of the research (e.g. results or conclusions) and highlight what is distinctive about it.
- An **Introduction** that should provide a review of recent literature and sufficient background information to allow the results of the article to be understood and evaluated.
- A **Methods** section detailing the theoretical or experimental methods used.
- An **Experimental section** that should provide details of the experimental set-up and the methods used to obtain the results.
- A **Results** section that should clearly and concisely present the data, using figures and tables where appropriate.
- A **Discussion** section that should describe the relationships and generalizations shown by the results and discuss the significance of the results, making comparisons with previously published work. (It may be appropriate to combine the Results and Discussion sections into a single section to improve clarity.)
- A **Conclusions** section that should present one or more conclusions drawn from the results and subsequent discussion and should not duplicate the Abstract.
- **Acknowledgement** (optional) of collaboration or preparation assistance may be included. Please note the source of funding for the research.
- **Nomenclature** (optional). Papers with many symbols should have a nomenclature that defines all symbols with units, inserted above the references. If one is used, it must contain all the symbols used in the manuscript and the definitions should not be repeated in the text. In all cases, identify the symbols used if they are not widely recognized in the profession. Define acronyms in the text, not in the nomenclature.
- **References** must be cited consecutively in the text using square brackets [1] and collected together in a reference list at the end of the manuscript.
- **Appendix(-ices)** if any.

## SPECIAL NOTES

**Units:** The SI system of units for nomenclature, symbols and abbreviations should be followed closely. Symbols for physical quantities in the text should be written in italics (e.g.  $v$ ,  $T$ ,  $n$ , etc.). Symbols for units that consist of letters should be in plain text (e.g.  $\text{ms}^{-1}$ , K, min, mm, etc.). Please also see: <http://physics.nist.gov/cuu/pdf/sp811.pdf>.

**Abbreviations** should be spelt out in full on first appearance followed by the abbreviation in parentheses, e.g. variable time geometry (VTG). The meaning of symbols and units belonging to symbols should be explained in each case or cited in a **nomenclature** section at the end of the manuscript before the References.

**Figures** (figures, graphs, illustrations digital images, photographs) must be cited in consecutive numerical order in the text and referred to in both the text and the captions as Fig. 1, Fig. 2, etc. Figures should be prepared without borders and on white grounding and should be sent separately in their original formats. If a figure is composed of several parts, please mark each part with a), b), c), etc. and provide an explanation for each part in Figure caption. The caption should be self-explanatory. Letters and numbers should be readable (Arial or Times New Roman, min 6 pt with equal sizes and fonts in all figures). Graphics (submitted as supplementary files) may be exported in resolution good enough for printing (min. 300 dpi) in any common format, e.g. TIFF, BMP or JPG, PDF and should be named Fig1.jpg, Fig2.tif, etc. However, graphs and line drawings should be prepared as vector images, e.g. CDR, AI. Multi-curve graphs should have individual curves marked with a symbol or otherwise provide distinguishing differences using, for example, different thicknesses or dashing.

**Tables** should carry separate titles and must be numbered in consecutive numerical order in the text and referred to in both the text and the captions as Table 1, Table 2, etc. In addition to the physical quantities, such as  $t$  (in italics), the units [s] (normal text) should be added in square brackets. Tables should not duplicate data found elsewhere in the manuscript. Tables should be prepared using a table editor and not inserted as a graphic.

## REFERENCES:

A reference list must be included using the following information as a guide. Only cited text references are to be included. Each reference is to be referred to in the text by a number enclosed in a square bracket (i.e. [3] or [2] for more references; do not combine more than 3 references, explain each). No reference to the author is necessary.

References must be numbered and ordered according to where they are first mentioned in the paper, not alphabetically. All references must be complete and accurate. Please add DOI code when available. Examples follow.

## Journal Papers:

Surname 1, Initials, Surname 2, Initials (year). Title. Journal, volume, number, pages, DOI code.

- [1] Hackenschmidt, R., Alber-Laukant, B., Rieg, F. (2010). Simulating nonlinear materials under centrifugal forces by using intelligent cross-linked simulations. *Strojniški vestnik - Journal of Mechanical Engineering*, vol. 57, no. 7-8, p. 531-538, DOI:10.5545/sv-jme.2011.013.

Journal titles should not be abbreviated. Note that journal title is set in italics.

## Books:

Surname 1, Initials, Surname 2, Initials (year). Title. Publisher, place of publication.

- [2] Groover, M.P. (2007). *Fundamentals of Modern Manufacturing*. John Wiley & Sons, Hoboken.

Note that the title of the book is italicized.

## Chapters in books:

Surname 1, Initials, Surname 2, Initials (year). Chapter title. Editor(s) of book, book title. Publisher, place of publication, pages.

- [3] Carbone, G., Ceccarelli, M. (2005). Legged robotic systems. Kordić, V., Lazinica, A., Merdan, M. (Eds.), *Cutting Edge Robotics*. Pro literatur Verlag, Mammendorf, p. 553-576.

## Proceedings Papers:

Surname 1, Initials, Surname 2, Initials (year). Paper title. Proceedings title, pages.

- [4] Štefanič, N., Martinčević-Mikić, S., Tošanović, N. (2009). Applied lean system in process industry. *MOTSP Conference Proceedings*, p. 422-427.

## Standards:

Standard-Code (year). Title. Organisation. Place.

- [5] ISO/DIS 16000-6.2:2002. *Indoor Air - Part 6: Determination of Volatile Organic Compounds in Indoor and Chamber Air by Active Sampling on TENAX TA Sorbent, Thermal Desorption and Gas Chromatography using MSD/FID*. International Organization for Standardization. Geneva.

## WWW pages:

Surname, Initials or Company name. Title, from <http://address>, date of access.

- [6] Rockwell Automation. Arena, from <http://www.arenasimulation.com>, accessed on 2009-09-07.

## EXTENDED ABSTRACT:

When the paper is accepted for publishing, the authors will be requested to send an **extended abstract** (approx. one A4 page or 3500 to 4000 characters or approx. 600 words). The instruction for composing the extended abstract are published on-line: <http://www.sv-jme.eu/information-for-authors/>.

## COPYRIGHT:

Authors submitting a manuscript do so on the understanding that the work has not been published before, is not being considered for publication elsewhere and has been read and approved by all authors. The submission of the manuscript by the authors means that the authors automatically agree to transfer copyright to SV-JME when the manuscript is accepted for publication. All accepted manuscripts must be accompanied by a Copyright Transfer Agreement, which should be sent to the editor. The work should be original work by the authors and not be published elsewhere in any language without the written consent of the publisher. The proof will be sent to the author showing the final layout of the article. Proof correction must be minimal and executed quickly. Thus it is essential that manuscripts are accurate when submitted. Authors can track the status of their accepted articles on <http://en.sv-jme.eu/>.

## PUBLICATION FEE:

Authors will be asked to pay a publication fee for each article prior to the article appearing in the journal. However, this fee only needs to be paid after the article has been accepted for publishing. The fee is 380 EUR (for articles with maximum of 6 pages), 470 EUR (for articles with maximum of 10 pages), plus 50 EUR for each additional page. The additional cost for a color page is 90.00 EUR (only for a journal hard copy; optional upon author's request). These fees do not include tax.



<http://www.sv-jme.eu>

# Contents

## Papers

- 215 Branislav Panić, Jernej Klemenc, Marko Nagode:  
**Gaussian Mixture Model Based Classification Revisited:  
Application to the Bearing Fault Classification**
- 227 VanThien Nguyen, VietHung Nguyen, VanTrinh Pham:  
**Deep Stacked Auto-Encoder Network Based Tool Wear Monitoring  
in the Face Milling Process**
- 235 Jakub Sikorski, Witold Pawlowski:  
**Internal Friction of Ball Bearings at Very Low Temperatures**
- 243 Sanjay Sundriyal, Vipin, Ravinderjit Singh Walia:  
**Study on the Influence of Metallic Powder in Near-Dry  
Electric Discharge Machining**
- 254 A.K. Babu, G. Kumaresan, V. Antony Aroul Raj, R. Velraj:  
**Experimental Investigations of Thin-layer Drying of Leaves  
in a Heat-Pump Assisted Tray-type Batch Drying Chamber**
- 266 Yang Zhang, Duanwei Shi, Tong Xiao, Ji Zhou, Xionghao Cheng:  
**Pitch Stability Analysis for Mechanical-Hydraulic-Structural-Fluid  
Coupling System of High-Lift Hoist Vertical Shiplift**